OPTICAL COHERENT CONTROL OF A SINGLE CHARGED INDIUM ARSENIDE QUANTUM DOT

by

Katherine L. Truex

A dissertation submitted in partial fulfillment
of the requirements for the degree of
Doctor of Philosophy
(Applied Physics)
in The University of Michigan
2011

Doctoral Commitee:

Professor Duncan G. Steel, Chair
Professor Paul R. Berman
Professor Roberto D. Merlin
Professor Theodore B. Norris
Professor Bradford G. Orr

ACKNOWLEDGEMENTS

The task of completing a PhD cannot be accomplished without a large amount of assistance from others. When I remember how little I knew when I first joined Duncan's group it makes me really appreciate how much others have taught me during my time in graduate school.

Dr. Dan Gammon's group at the Naval Research Lab has not only provided us with the samples and device expertise that make our research possible, but they have also provided important collaborations on spectroscopy and coherent control. I have benefited from interactions with Alan Bracker, Danny Kim, and Sophia Economou at conferences and via teleconferences. I owe a huge thank you to Professor Lu Sham for patiently teaching me about entanglement. His guidance was critical in completing the entropy of entanglement discussion in Appendix A. Dan and Lu's visits to Ann Arbor were some of the most intense days of learning of my graduate career. I would like to acknowledge Professor Luming Duan for the inspiration to pursue entanglement within the spin-exciton system, which lead to the work presented in Chapter 4.

I feel very fortunate to have been a student in Duncan Steel's lab. Duncan is always compassionate and encouraging, but with high standards. While this can be confusing at times, he has provided an excellent environment that allowed me to grow into a much more independent researcher. I want to thank Yanwen Wu, Erik Kim, and Xiaodong Xu for teaching me the ropes in the lab. Erik set an excellent example of lab work ethic and taught me how seemingly insignificant things can affect an experiment. The spin rotation work in Chapter 3 was a collaborative project with Erik. Bo Sun and I joined the lab at the same time and now are graduating within

a few months of each other. While we have always worked on different projects, he has been a great source of ideas and encouragement. I feel very lucky that I was able to work with Leon Webster this past year, because he is both a friend and a fast learner. He has done a wonderful job of continuing the entanglement project while I was writing my thesis. John Schaibley and Leon deserve special thanks for their extensive editing of this thesis, though many people contributed revisions. Many thanks to everyone I have worked with in the Steel group: Jun Cheng, Qiong Huang, Vasudev Lal, Colin Chow, Renee Harton, Meredith Henstridge, Alex Burgers, and Greg McCracken as well as those already named above. You have been my teachers, coworkers, and most importantly my friends. It has been a real pleasure.

My family deserves the biggest thank you. I cannot count the number of times that I called my parents, Arthur and Loraine Smirl, for words of wisdom during the past year. They raised me to value hard work and education, and ever since they have supported me in all of my pursuits. Perhaps most importantly, they taught me "Hail to the Victors" at a young age. Their confidence in me, their confidence that my work would pay off in the end, and their reminders that there IS a life after graduate school helped me through the inevitable times of frustration. Even my extended family, who probably wonder why in the world I am still in school, have been constantly supportive. My husband, Beau, has supported me daily and from my first year of graduate school through my defense. I can never thank him enough for being flexible while I finished my degree here in Ann Arbor, and for all that he has done for me during my final year. I know I would have eaten a lot more Ramen and frozen pizzas if it had not been for him. It is not easy to live with someone during the stress of writing a dissertation. Thank you for being here for me.

I was told at the recruiting weekend that Applied Physics is like a family, and I couldn't agree more, thanks to the efforts of Cynthia McNabb, Charles Sutton, and Brad Orr. My fellow first year Applied Physics students have become some of my closest friends. I would like to end by thanking all of my friends who have kept me sane and have forgiven me for being stressed out and having a crazy schedule during graduate school.

TABLE OF CONTENTS

LIST OF FIGURES

Figure

LIST OF APPENDICES

Appendix

CHAPTER 1

Motivation and Requirements for Quantum Computing

Quantum computing, defined as information processing using quantum mechanical systems, is a valuable technique that can solve certain problems much more efficiently than a classical computer. Cobham's thesis defined an "efficient" algorithm as one that scales as a polynomial of the size of the problem's input, and equated an "efficient" algorithm with one that could be feasibly computed by any "reasonable and general" classical method [1]. Quantum simulations [2], Shor's algorithms [3], and Grover's algorithm [4] are examples of problems for which quantum algorithms have been developed that are more efficient than classical algorithms.

One of Richard Feynman's insights was the suggestion in 1982 that a quantum computer could simulate quantum systems more efficiently than a classical computer [2]. This suggestion was later proved to be correct by Seth Lloyd in 1996 [5]. The challenge in simulating quantum systems stems from the 2^n differential equations that must be solved to model n quantum bits. A quantum bit, or qubit, is simply a two level system that obeys the laws of quantum mechanics and serves an analogous role in quantum computing to that of bits in classical computing. The ability to simulate quantum systems could have implications for a wide range of applications and scientific fields, such as calculating basic parameters for chemistry, simulating the Hubbard model, or even simulating quantum gravity if enough qubits were available [5].

Among the most famous and influential quantum algorithms are Shor's and Grover's algorithms. In 1994, Peter Shor presented a method for computing both prime fac-

torization and the discrete logarithm problem in polynomial time using quantum algorithms that take advantage of the quantum Fourier transform [3]. Shor's algorithm is a substantial improvement in efficiency over the fastest existing classical factoring algorithm, which scales sub-exponentially with the bits in the number to be factored [3]. These efficient factoring and discrete logarithm algorithms receive so much attention because, if implemented, they would render public key encryption no longer secure [6].

Lov Grover's quantum search algorithm, which addresses the challenge of searching an unsorted database, would run in time $\sqrt{N}$ compared to time N for a classical algorithm [4]. While there are some limitations to the usefulness of this algorithm in searching classical databases, Grover's search algorithm has the possible application of speeding up solutions to the set of Non Polynomial-complete problems [6].

1.1 Physical Implementations of Quantum Computing

In his 2000 paper [7], DiVincenzo enumerated five fundamental requirements for quantum computation:

1. A scalable physical system with well characterized qubits

The requirement of scalability refers to the fact that a quantum computer able to perform useful computations will need to consist of a large number of qubits.

2. The ability to initialize the state of the qubits

Initialization is fundamental to computing schemes since it is important to start in a known state. Also, quantum error correction schemes require a continuous supply of initialized qubits.

3. Long relevant decoherence times compared to the gate operation time

Since coherence is essential to quantum computation, the ratio of the gate operation time to the decoherence time determines the number of operations that can be performed before the qubits must be reinitialized. The necessary ratio is still under discussion, but it is largely dependent on error correction schemes. DiVincenzo suggests a ratio of 10^{-4} to 10^{-5} would be sufficient.

4. A "universal" set of quantum gates

A universal set of quantum gates is a set of gates that can be used to compute any unitary quantum operation. One example of a universal set of gates is a single qubit gate and a controlled not (CNOT) gate [6].

5. A qubit specific measurement capability

Ideally, a measurement on one qubit would not change the state of the rest of the qubits.

1.1.1 Nuclear Magnetic Resonance

One of the early approaches to implementing a quantum computer was based on nuclear magnetic resonance (NMR) techniques with the spin states of molecules serving as qubits. Early success, such as a 7 bit demonstration of Shor's algorithm in 2001 [8], gave way to substantial challenges: increasing the number of bits reduced the signal strength exponentially making systems above 10 qubits challenging [9] and studies by Caves and others showed that liquid state ensemble NMR efforts so far did not possess quantum entanglement [10].

1.1.2 Optical Quantum Computing

The use of photons as qubits faces a major challenge due to the large number of operations that must be performed to obtain sufficiently high fidelities [11]. At first the extremely large resource overhead required due to this challenge seemed to condemn optical qubits, but recent work has been addressing this issue with new error encoding schemes and cluster-state methods [12–15]. The future feasibility of this method will require the development of high-efficiency single photon sources and detectors as well as low loss optical circuits, as the entire optical system must be highly efficient [11].

1.1.3 Trapped ions and atoms

Another very successful and mature implementation of quantum computing is the

use of trapped ions and atoms as qubits. As many as 14 trapped ions have been entangled [16], and a semiclassical quantum Fourier transform algorithm has been demonstrated in a three ion system [17]. The electromagnetic interactions between ions makes scaling to large numbers of qubits challenging, especially in a linear qubit geometry. In response to this challenge, research is ongoing on three dimensional arrays of ions as well as on the use of neutral atoms as qubits. In early 2010 the first two qubit gate was demonstrated for neutral atoms [18].

1.1.4 Superconducting qubits

One of the more popular approaches to quantum computing has been the use of solid state superconducting circuits involving Josephson junctions. Several types of qubits have been explored, including charge, quantronium, flux, and phase qubits, in an attempt to find the longest possible decoherence time [19]. These circuits have the advantage that they use very little energy and offer direct control of the interaction between qubits [19]. Demonstrations to date include a CNOT gate [20], entanglement of qubits [21], and a single qubit gate with the predicted ability to perform 10^4 operations before decoherence [19].

1.1.5 Quantum Dots

Our group studies optically controlled semiconductor quantum dots. The quantum confinement present in dots is very favorable for quantum computing. One reason for this is a shift in the biexciton energy due to confinement, which leads to the suppression of many-body effects in semiconductor quantum dots [22, 23]. Many-body effects are extremely detrimental to quantum computing schemes since they greatly increase the decoherence in the system. Semiconductor quantum dots have the advantage that they are inherently spatially stable without the need for complex optical traps as are needed for ion studies. Also, successful semiconductor quantum dot technology is able to take advantage of the existing semiconductor manufacturing infrastructure. Quantum dot lasers [24–26], detectors [27–30], and light emitting

diodes [31–34] illustrate the potential to integrate quantum dots with existing III-V semiconductor devices. The physical parameters of quantum dots can be controlled by engineering the growth process, though ultimately the growth process is statistical and results in a wafer with a distribution of physical properties. Dots are characterized after growth and post-selected for desired characteristics.

The dots studied in this thesis are self-assembled semiconductor quantum dots (SAQDs). In addition to possible quantum computing applications, SAQDs show promise as single photon sources [35], entangled-photon sources [36, 37], and single-photon optical switches [38]. Self-assembled dots have better lateral confinement than other types of semiconductor dots, such as interface fluctuation dots. However, the dipole moments in the self-assembled dots tend to be smaller than interface dots. We have measured dipole moments on the order of 10-30 Debye in our self-assembled dots compared to 100 Debye in interface dots [39, 40]. This has made detection of some optical signals more challenging. Self-assembled dots confine both electrons and holes up to temperatures of 10 K, compared to electrically defined dots, which only confine one carrier and operate at milliKelvin temperatures [41]. Confinement of both electrons and holes is necessary to take advantage of optical transitions as a fast control technique.

One of the most promising aspects of the indium arsenide (InAs) self-assembled quantum dots studied in this work is the long electron spin dephasing time. The spin dephasing time is normally shortened by the nuclear environment, leading to an estimated spin dephasing time as short as 1 nanosecond, but this has been lengthened to 80 nanoseconds by optical locking of the nuclear field [42, 43]. Once combined with the ability to manipulate the spin with picosecond (or shorter) pulses, as will be demonstrated in Chapter 3, over 10^4 operations could be possible within the spin dephasing time, making the spin of an electron confined in an InAs self-assembled dot a promising qubit.

1.2 Gates and Rotations

The simplest possible gate operates on a single qubit. All quantum gates must be unitary operations, U, such that $U^\dagger U = 1$. Any unitary single qubit operator can be written as $U = e^{i\phi} R_{\hat{n}}(\theta)$, where $R_{\hat{n}}(\theta)$ represents a rotation of the qubit by an angle θ about the axis $\hat{n}$. Thus any single qubit operation can be accomplished with a rotation and a global phase shift. Furthermore, the rotation, $R_{\hat{n}}(\theta)$, about a general axis and by a general angle, known as an arbitrary rotation, can be decomposed into $R_{\hat{n}}(\theta) = R_{\hat{a}}(\alpha) R_{\hat{b}}(\beta) R_{\hat{a}}(\gamma)$, where $\hat{a}$ and $\hat{b}$ are any non-parallel vectors. The result of this is that any single qubit gate can be formed from rotations about any two non-parallel axes plus a phase gate. As stated earlier, this single qubit gate combined with a CNOT gate form a universal set of gates that can accomplish any unitary operation on any number of bits [6].

1.3 Entanglement

Entanglement is a quantum mechanical effect that can occur in composite systems and is important for quantum computing. If $|\psi\rangle$ is a wavefunction in subsystem A, $|\phi\rangle$ is a wavefunction in subsystem B, and noninteracting subsystems A and B were prepared independently, then the wavefunction of the composite system AB is the product state $|\phi\rangle|\psi\rangle$. Furthermore, if measurements were made separately on systems A and B, we would not expect to find any correlations between the measurements. Entangled states are states of composite systems that cannot be written as product or factorisable states of their subsystems. Measurements of subsystems of entangled states have some correlation. The entropy of entanglement is one method for quantifying entanglement, which is discussed in detail in Appendix A [6].

Neilson and Chuang describe entanglement as a resource whose properties and "crucial" role in quantum computing are not yet fully understood [6]. Ekert and Jozsa asserted in 1998 that entanglement was "the essential non-classical feature providing the computational speed-up in the known quantum algorithms" using the quantum Fourier transform as an example [44]. This statement was qualified in a

paper by Jozsa and Linden in 2002, which clarified that entanglement was essential only in algorithms that operate on pure states, and therefore may not be essential for computational speed-up in algorithms that operate on mixed states [45].

Despite these ongoing discussions about the role of entanglement in quantum computing, it may seem strange that entanglement is not mentioned in DiVincenzo's list of requirements. In fact, entanglement is implicitly contained in requirement 4, which requires a universal set of gates. Physical systems become entangled due to dynamical interactions between them, and this interaction could be a defined multi-qubit gate. It has been proved that a two qubit gate is universal if and only if it is an entangling gate [46], therefore a demonstration of a universal two qubit gate is a demonstration of entanglement.

Entanglement can be a useful tool in demonstrating a scalable system, part of DiVincenzo's first requirement. Demonstrating controllable entanglement between different qubits in a large network requires that the two qubits interact selectively. One proposed method for this interaction in quantum dot networks is via a photon intermediate called a "flying qubit". The idea is that the first dot-based qubit would be entangled with an emitted photon, which then would be absorbed by a second distant dot, leaving the two dots entangled [47]. Two systems that are maximally entangled, or have an entropy of entanglement of 1, essentially contain the same information since measurement on either system is completely correlated with the other system. Therefore, entangling interactions have the useful ability to pass information from one system to another. The potential of combining solid state qubits with flying qubits has created a high level of interest in demonstrations of spin-photon entanglement. Chapter 4 discusses preliminary efforts toward such a demonstration with a single electron spin in a self-assembled quantum dot.

Entanglement methods are often described as either deterministic or probabilistic. If a system is deterministically entangled, then the desired state of the system is created with a high degree of certainty. In probabilistic entanglement methods, some non-negligible fraction of the time entanglement is not created. Usually some form of post-selection is used with probabilistic methods. Scaling probabilistic entanglement

methods to large numbers of qubits requires error-correction or "entanglement purification" methods, since the probability of entanglement drops exponentially with the number of entangled qubits [48], [49], [50].

1.4 Thesis Outline

This thesis discusses and demonstrates optical coherent control techniques for an electron spin in a single InAs self-assembled quantum dot. Chapter 2 begins with a description of the samples studied, including the growth method, structure, and how the sample features enable single dot optical studies. Following this, some of the relevant condensed matter properties of bulk direct gap semiconductors and quantum dots are discussed to lay the groundwork for a detailed discussion of optical transitions in InAs dots. Equations of motion are derived for the lowest four energy levels of the dot in both the amplitude and density matrix pictures for a dot interacting with a static magnetic field and a dynamic optical field. These equations are the starting point for most calculations and simulations in this thesis. The chapter ends with a description of initial sample characterization using photoluminescence and modulated absorption techniques.

Chapter 3 describes methods for rapid initialization and readout using a frequency stable continuous wave laser and derives an expression for the readout signal in terms of the density matrix elements of the dot. These methods are used in all of the experiments presented in this work. The remainder of the chapter discusses methods for rotating the spin qubit, with a focus on optical methods. Three rotation techniques are demonstrated: (1) rotation about the optical axis by detuned picosecond optical pulses via a nearly resonant stimulated Raman process, (2)precession about the magnetic field between two Raman pulses, and (3) the generation of geometric phases from cyclic Rabi oscillations. These demonstrations provide the basic tools to achieve an arbitrary rotation, which is one component of a universal set of spin qubit gates.

Chapter 4 was inspired by a proposal by Yao, Liu, and Sham for deterministic

spin-photon entanglement [51]. The proposal requires creating a specific superposition of quantum dot eigenstates and then allowing the dot to radiatively decay. Chapter 4 proposes a coherent control experiment to create this precursor superposition state using a series of optical pulses. A calculation of the entropy of entanglement of the precursor state, described in Appendix A, shows that it is a partially entangled many particle state. Simulations of the proposed experiment predict a high fidelity for obtainable experimental parameters, including effects of decay and decoherence. Finally, Chapter 5 reviews the progress toward quantum computing that is covered in Chapters 2 through 4 and describes potential future work that is suggested by these results.

BIBLIOGRAPHY

BIBLIOGRAPHY

[1] O. Goldreich, *Computational Complexity*, Cambridge University Press, New York, NY, first edition, p.33 (2008).

[2] R. Feynman, "Simulating Physics with Computers", *International Journal of Theoretical Physics* **21**, 467 (1982).

[3] P. Shor, "Algorithms for quantum computation: discrete logarithms and factoring", *Foundations of Computer Science, Annual IEEE Symposium on* **0**, 124 (1994).

[4] L. K. Grover, "Quantum Mechanics Helps in Searching for a Needle in a Haystack", *Phys. Rev. Lett.* **79**, 325 (1997).

[5] S. Lloyd, "Universal quantum simulators", *Science* **273**, 1073 (1996).

[6] M. A. Nielsen, I. L. Chuang, *Quantum Computation and Quantum Information*, Cambridge University Press, Cambridge, United Kingdom, first edition (2000).

[7] D. P. DiVincenzo, "The Physical Implementation of Quantum Computation", *Fortschr. Phys.* **48** (2000).

[8] L. Vandersypen, M. Steffen, G. Breyta, C. Yannoni, M. Sherwood, I. Chuang, "Experimental realization of Shor's quantum factoring algorithm using nuclear magnetic resonance", *Nature* **414**, 883 (2001).

[9] I. L. Chuang, L. M. K. Vandersypen, X. Zhou, D. W. Leung, S. Lloyd, "Experimental realization of a quantum algorithm", *Nature* **393**, 4 (1998).

[10] N. C. Menicucci, C. M. Caves, "Local Realistic Model for the Dynamics of Bulk-Ensemble NMR Information Processing", *Phys. Rev. Lett.* **88**, 167901 (2002).

[11] J. L. O'Brien, "Optical quantum computing", *Science* **318**, 1567 (2007).

[12] P. Walther, K. J. Resch, T. Rudolph, E. Schenck, H. Weinfurter, V. Vedral, M. Aspelmeyer, A. Zeilinger, "Experimental One-Way Quantum Computing", *Nature* **434**, 169 (2005).

[13] N. Kiesel, C. Schmid, U. Weber, G. Tóth, O. Gühne, R. Ursin, H. Weinfurter, "Experimental Analysis of a Four-Qubit Photon Cluster State", *Phys. Rev. Lett.* **95**, 210502 (2005).

[14] R. Prevedel, P. Walther, F. Tiefenbacher, P. Bhi, R. Kaltenbaek, T. Jennewein, A. Zeilinger, "High-speed linear optics quantum computing using active feed-forward.", *Nature* **445**, 19 (2007).

[15] C.-Y. Lu, X.-Q. Zhou, O. Ghne, W.-B. Gao, J. Zhang, Z.-S. Yuan, A. Goebel, T. Yang, J.-W. Pan, "Experimental entanglement of six photons in graph states", *Nature Physics* **3**, 91 (2006).

[16] T. Monz, P. Schindler, J. T. Barreiro, M. Chwalla, D. Nigg, W. A. Coish, M. Harlander, W. Haensel, M. Hennrich, R. Blatt, "14-Qubit Entanglement: Creation and Coherence", *Physical Review Letters* **106** (2011).

[17] J. Chiaverini, J. Britton, D. Leibfried, E. Knill, M. D. Barrett, R. B. Blakestad, W. M. Itano, J. D. Jost, C. Langer, R. Ozeri, T. Schaetz, D. J. Wineland, "Implementation of the Semiclassical Quantum Fourier Transform in a Scalable System", *Science* **308**, 997 (2005).

[18] L. Isenhower, E. Urban, X. L. Zhang, A. T. Gill, T. Henage, T. A. Johnson, T. G. Walker, M. Saffman, "Demonstration of a Neutral Atom Controlled-NOT Quantum Gate", *Phys. Rev. Lett.* **104**, 010503 (2010).

[19] J.-S. Tsai, "Toward a superconducting quantum computer. Harnessing macroscopic quantum coherence.", *Proceedings of the Japan Academy Series B Physical and biological sciences* **86**, 275 (2010).

[20] J. H. Plantenberg, P. C. De Groot, C. J. P. M. Harmans, J. E. Mooij, "Demonstration of controlled-NOT quantum gates on a pair of superconducting quantum bits.", *Nature* **447**, 836 (2007).

[21] M. Steffen, M. Ansmann, R. C. Bialczak, N. Katz, E. Lucero, R. McDermott, M. Neeley, E. M. Weig, A. N. Cleland, J. M. Martinis, "Measurement of the entanglement of two superconducting qubits via state tomography.", *Science* **313**, 1423 (2006).

[22] N. H. Bonadeo, G. Chen, D. Gammon, D. S. Katzer, D. Park, D. G. Steel, "Nonlinear Nano-Optics: Probing One Exciton at a Time", *Phys. Rev. Lett.* **81**, 2759 (1998).

[23] X. Li, Y. Wu, D. Steel, D. Gammon, T. H. Stievater, D. S. Katzer, D. Park, C. Piermarocchi, L. J. Sham, "An All-Optical Quantum Gate in a Semiconductor Quantum Dot", *Science* **301**, 809 (2003).

[24] N. Kirstaedter, N. N. Ledentsov, M. Grundmann, D. Bimberg, V. M. Ustinov, S. S. Ruvimov, M. V. Maximov, P. S. Kopev, Z. I. Alferov, U. Richter, et al., "Low threshold large T_0 injection laser emission from (InGa)As quantum dots", *Electronics Letters* **30**, 1416 (1994).

[25] D. L. Huffaker, G. Park, Z. Zou, O. B. Shchekin, D. G. Deppe, "1.3 μm room-temperature GaAs-based quantum-dot laser", *Appl. Phys. Lett.* **73**, 2564 (1998).

[26] "Fujitsu launches quantum dot laser venture", *R&D Magazine* **48**, 11 (2006).

[27] J. Phillips, K. Kamath, P. Bhattacharya, "Far-infrared photoconductivity in self-organized InAs quantum dots", *Appl. Phys. Lett.* **72**, 2020 (1998).

[28] K. W. Berryman, S. A. Lyon, M. Segev, "Mid-infrared photoconductivity in InAs quantum dots", *Appl. Phys. Lett.* **70**, 1861 (1997).

[29] H. Liu, J.-Y. Duboz, R. Dudek, Z. Wasilewski, S. Fafard, P. Finnie, "Quantum dot infrared photodetectors", *physica. E* **17**, 631 (2003).

[30] X. H. Su, J. Yang, P. Bhattacharya, G. Ariyawansa, A. G. U. Perera, "Terahertz detection with tunneling quantum dot intersublevel photodetector", *Applied Physics Letters* **89**, 031117 (2006).

[31] D. L. Huffaker, L. A. Graham, D. G. Deppe, "Ultranarrow electroluminescence spectrum from the ground state of an ensemble of self-organized quantum dots", *Appl. Phys. Lett.* **72**, 214 (1998).

[32] C. Monat, B. Alloing, C. Zinoni, L. H. Li, A. Fiore, "Nanostructured Current-Confined Single Quantum Dot Light-Emitting Diode at 1300nm", *Nano Letters* **6**, 1464 (2006).

[33] Z. Mi, Y. L. Chang, "III-V compound semiconductor nanostructures on silicon: Epitaxial growth, properties, and applications in light emitting diodes and lasers", *Journal of Nanophotonics* **3** (2009).

[34] Q. Dai, C. E. Duty, M. Z. Hu, "Semiconductor-Nanocrystals-Based White Light-Emitting Diodes", *SMALL* **6**, 1577 (2010).

[35] Z. Yuan, B. E. Kardynal, R. M. Stevenson, A. J. Shields, C. J. Lobo, K. Cooper, N. S. Beattie, D. A. Ritchie, M. Pepper, "Electrically Driven Single-Photon Source", *Science* **295**, 102 (2002).

[36] N. Akopian, N. H. Lindner, E. Poem, Y. Berlatzky, J. Avron, D. Gershoni, B. D. Gerardot, P. M. Petroff, "Entangled Photon Pairs from Semiconductor Quantum Dots", *Phys. Rev. Lett.* **96**, 130501 (2006).

[37] R. J. Young, R. M. Stevenson, P. Atkinson, K. Cooper, D. A. Ritchie, A. J. Shields, "Improved fidelity of triggered entangled photons from single quantum dots", *New Journal of Physics* **8**, 29 (2006).

[38] D. Englund, A. Faraon, I. Fushman, N. Stoltz, P. Petroff, J. Vuckovic, "Controlling Cavity Reflectivity with a Single Quantum Dot", *Nature* **450**, 857 (2007).

[39] T. H. Stievater, X. Li, D. G. Steel, D. Gammon, D. S. Katzer, D. Park, C. Piermarocchi, L. J. Sham, "Rabi oscillations of excitons in single quantum dots.", *Physical Review Letters* **87**, 133603 (2001).

[40] X. Xu, B. Sun, P. R. Berman, D. G. Steel, A. S. Bracker, D. Gammon, L. J. Sham, "Coherent Optical Spectroscopy of a Strongly Driven Quantum Dot", *Science* **317**, 929 (2007).

[41] J. R. Petta, A. C. Johnson, J. M. Taylor, E. A. Laird, A. Yacoby, M. D. Lukin, C. M. Marcus, M. P. Hanson, A. C. Gossard, "Coherent Manipulation of Coupled Electron Spins in Semiconductor Quantum Dots", *Science* **309** (2005).

[42] X. Xu, W. Yao, B. Sun, D. G. Steel, A. S. Bracker, D. Gammon, L. J. Sham, "Optically controlled locking of the nuclear field via coherent dark-state spectroscopy", *Nature* **459**, 1105 (2009).

[43] D. Gammon, D. G. Steel, "Optical Studies of Single Quantum Dots", *Physics Today* **55**, 36 (2002).

[44] A. Ekert, R. Jozsa, "Quantum algorithms: entanglement-enhanced information processing", *Philosophical Transactions of the Royal Society of London Series A - Mathematical Physical and Engineering Sciences* **356**, 1769 (1998).

[45] R. Jozsa, N. Linden, "On the role of entanglement in quantum computational speed-up", *Computer* 1–22 (2002).

[46] J.-L. Brylinski, R. Brylinski, "Universal quantum gates", *Mathematics of quantum computation* 10 (2001).

[47] R.-B. Liu, W. Yao, L. J. Sham, "Quantum computing by optical control of electron spins", *Advances in Physics* **59**, 69 (2010).

[48] R. Blatt, "Push-button entanglement", *Nature* **404**, 231 (2000).

[49] L. M. Duan, M. D. Lukin, J. I. Cirac, P. Zoller, "Long-distance quantum communication Long-distance quantum communication with atomic ensembles and linear optics", *Nature* **414**, 413 (2001).

[50] L.-M. Duan, C. Monroe, "Robust probabilistic quantum information processing with atoms, photons, and atomic ensembles", volume 55 of *Advances In Atomic, Molecular, and Optical Physics*, 419 – 463, Academic Press (2008).

[51] W. Yao, L. Ren-Bau, L. J. Sham, "Theory of Control of the Spin-Photon Interface for Quantum Networks", *Phys. Rev. Lett.* **95** (2005).

CHAPTER 2

Background: Optical Properties and Characterization of Self Assembled Quantum Dots

The previous chapter discussed several physical implementations of quantum computing and described many of the advantages of self-assembled semiconductor quantum dots for quantum computing. The two most promising aspects of these dots are a long spin coherence time and the potential for fast optical manipulation of the electron spin, which should allow a spin qubit to undergo a large number of gate operations before it loses coherence. This thesis focuses on optical coherent control of the spin of an electron trapped in a self-assembled indium arsenide quantum dot with the ultimate goals of single qubit gates and demonstrations of entanglement. However, it is first necessary to understand the optical properties of InAs dots.

This chapter begins with a description of the structure of the quantum dot sample used for the studies presented in Chapter 3 and 4. Sections 2.2 and 2.3 mention a few aspects of semiconductor band structure and approximate quantum dot wavefunctions that are relevant to understanding optical quantum dot interactions. The primary dot states of interest for this work are presented. Section 2.4 develops the general theoretical framework, including the equations of motion for optical interactions in indium arsenide (InAs) quantum dots. Lastly, Section 2.5 explains the initial experimental characterization process for quantum dots.

2.1 Sample Growth and Structure

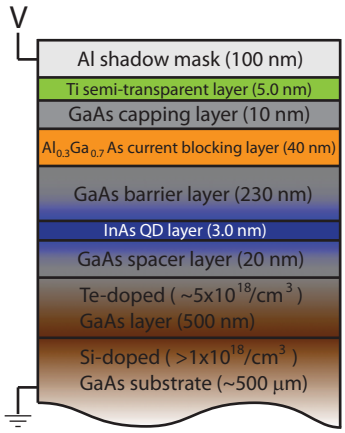

Figure 2.1: Detailed structure of sample studied in this thesis. Electrical contacts are applied to the silicon-doped gallium arsenide layer and to the titanium layer. The thickness of each layer is given in parentheses. (Figure reproduced with permission from E. D. Kim)

While several samples and many dots were explored, all data presented in this thesis was taken on a single dot in a single sample. The sample, labeled R060913G, was fabricated via molecular beam epitaxy by Daniel Gammon's group at the Naval Research Lab. Stated simply, the sample consists of a single layer of InAs/GaAs self-assembled quantum dots embedded in a Schottky diode structure. Specifically, the sample structure is shown in Figure 2.1. The back contact of the diode is a doped GaAs substrate. On top of this is a tellurium doped GaAs layer, which serves as an electron reservoir to provide negative charges to the dots. The InAs dot layer is sandwiched between two barrier layers of GaAs that create a quantum well in the growth direction.

The InAs dots self-assemble via a Stranski-Krastanov process that involves the formation of a thin InAs wetting layer before strain induces InAs island formation [1]. After the InAs dots have formed, an indium flush technique is used to shorten the dots along the growth direction, which shifts the optical transitions around 50 nm to the blue [2, 3]. This is desirable because it shifts the optical transitions to a range of 920-980 nm, within the wavelength range of titanium:sapphire (Ti:Saph) lasers and silicon detectors.

Above the GaAs barrier layer is an AlGaAs layer to block carriers from reaching the top electrical contact and then another thin GaAs layer. A semi-transparent titanium layer provides the top contact of the diode. The voltage is applied to the top contact through an aluminum mask. The mask has micron sized apertures etched into it to enable illumination of only a small area of the sample [4]. Given the density of the dots ($1/\mu m^2$) in the sample, the spatial resolution of these apertures, and the spectral resolution of our experiments, we are able to limit our studies to a single quantum dot.

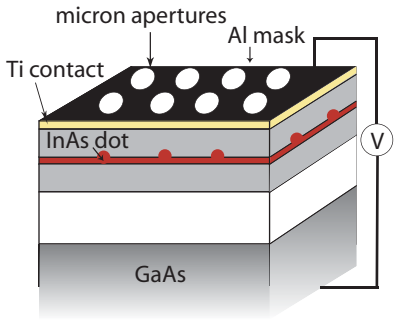

Figure 2.2: A cartoon showing the aluminum mask with micron-sized apertures on the top surface of the self-assembled dot samples.

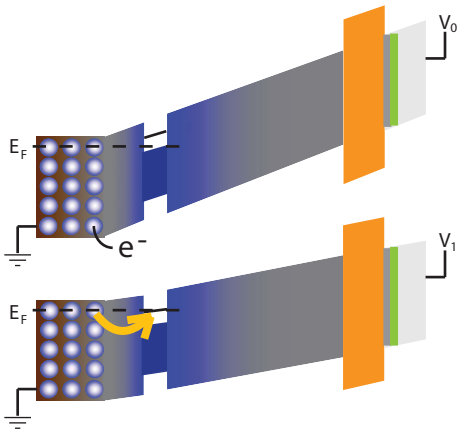

Figure 2.3: When the gate voltage is low (V_0) the lowest energy level of the dot is above the Fermi level. If the gate voltage is raised an appropriate amount to V_1, then the lowest dot level is lowered and an electron can tunnel to the dot. (Figure reproduced with permission from E. D. Kim.)

The Schottky diode structure allows selective charging of the dots. At a certain

gate voltage, V_0 in Figure 2.3, the dot under investigation is neutral. This is because the lowest confined state in the quantum dot is above the Fermi level of the doped GaAs. If the gate voltage is raised sufficiently, then the lowest quantum dot level is lowered below the Fermi level of the doped GaAs, allowing a single electron to tunnel from this reservoir through the intrinsic GaAs barrier into the dot [5]. Tunneling of further electrons does not occur at this voltage because the energy level of a dot with two electrons is so much higher than that of a singly charged dot due to the Coulomb blockade [6]. Smaller changes of the gate voltage shift the optical transition energies via a DC Stark effect. Section 2.5.2 describes how this effect is useful for phase sensitive detection.

2.2 Energy level structure: Bulk

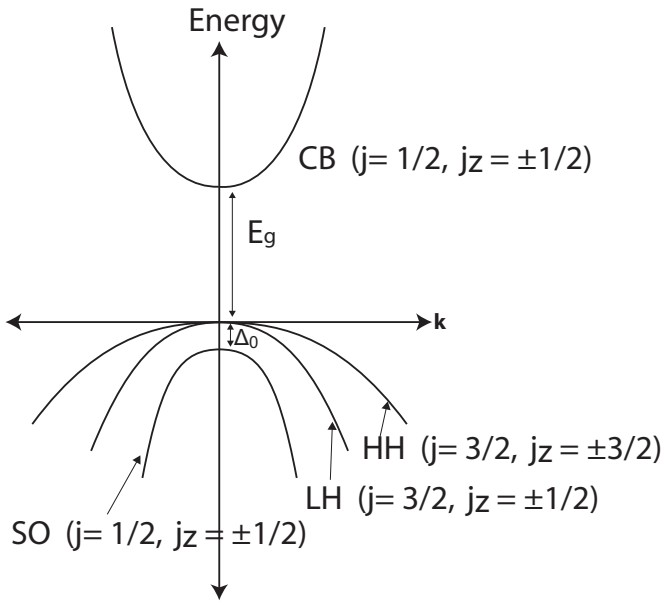

Figure 2.4: Band structure of a bulk direct bandgap semiconductor, such as GaAs or InAs. The conduction band (CB) is separated from the upper valence band by a band gap E_g. The heavy hole (HH) and light hole (LH) bands are separated from the split-off band (SO) by an energy Δ_0

An understanding of the energy levels and states of a semiconductor quantum dot begins with the bulk semiconductor band structure, shown in Figure 2.4. The figure

shows a simplified version of the allowed energy bands of a direct bandgap semiconductor as a function of crystal momentum, $\mathbf{k}$. At room temperature, a semiconductor has a highest occupied band called the valence band and a lowest unoccupied band called the conduction band. The electron wavefunctions, $\Psi_{\mathbf{k}}(\mathbf{r})$, must satisfy Bloch's Theorem

$$\Psi_{\mathbf{k}}(\mathbf{r}) = \sum_{\mathbf{R}} e^{i\mathbf{k}\cdot\mathbf{R}}\phi(\mathbf{r}-\mathbf{R}) \tag{2.1}$$

where $\mathbf{R}$ is the periodic vector of the crystal lattice and ϕ is the periodic Bloch function. Tight binding calculations approximate $\phi(\mathbf{r})$ as

$$\phi(\mathbf{r}) = \sum_{n=1}^{N} b_n\psi_n(\mathbf{r}) \tag{2.2}$$

where $\psi_n(\mathbf{r})$ are atomic eigenfunctions [7]. Such a calculation finds the eigenfunctions of the conduction band to be primarily composed of s atomic orbitals and the valence band primarily of p orbitals [8]. Because of this, the conduction band is said to have an orbital angular momentum of $l = 0$, and the valence band is labeled as $l = 1$.

As electrons and holes are the carrier of interest with a spin of $\frac{1}{2}$, the total angular momentum in the conduction band is $\mathbf{j} = \mathbf{s}+\mathbf{l} = \frac{1}{2}+0$, and the only possible eigenvalue of $\mathbf{j}$ is $j = \frac{1}{2}$. However in the valence band both $\mathbf{s}$ and $\mathbf{l}$ are nonzero and can combine such that j can be either $\frac{1}{2}$ or $\frac{3}{2}$. The energy of the $j = \frac{1}{2}$ band is much lower than the other valence bands, earning it the name split-off (SO) band with no further consideration in this work. The higher energy valence bands have $j = \frac{3}{2}$, which allows projections along the axis of symmetry of $\pm\frac{1}{2}$ or $\pm\frac{3}{2}$. The z axis is defined as the axis of symmetry, which is also the growth direction of our sample because the dots were grown on a [001] substrate [4].

As shown in Figure 2.4, the $j_z = \frac{1}{2}$ band has higher curvature as a function of $\mathbf{k}$ than the $j_z = \frac{3}{2}$ state. Since effective mass is defined in semiconductors as $m^* = \hbar^2[\frac{d^2\varepsilon}{dk^2}]^{-1}$, the $j_z = \frac{1}{2}$ ($\frac{3}{2}$) band has a lower (higher) effective mass and is termed the light-hole or LH (heavy-hole or HH) band. These bands are labeled as hole bands because they are valence bands which are completely or mostly filled, allowing a convenient discussion of charge carriers through the concept of a hole, or the absence

of an electron within a sea of other valence electrons. The hole has the opposite spin and charge to the missing electron [9].

2.3 Energy level structure: Quantum Dots

Our system of interest is not simply a bulk semiconductor, but rather a semiconductor quantum dot. A quantum dot is a potential energy well that spatially confines carriers in three dimensions. This localization of carriers comes from a combination of the bandgap offset between InAs and GaAs and the lateral strain inherent in self-assembled dots [10].

The $\mathbf{k} \cdot \mathbf{p}$ method is common for calculating approximate dot states, $\Psi_{\mathbf{k}}^{dot}(\mathbf{r})$. In this method, the Bloch exponential and weighting factor from the bulk tight binding calculation are replaced by an envelope function f($\mathbf{r}$) such that

$$\Psi_{\mathbf{k}}^{dot}(\mathbf{r}) = \sum_{j} f_{j\mathbf{k}}(\mathbf{r})\phi_j(\mathbf{r}) \tag{2.3}$$

[8]. Calculations for InAs self-assembled dots show that the majority of the contribution to the ground state conduction band is s-like and the ground state valence band remains mostly p-like [11]. When determining optical transition matrix elements, the atomic wavefunctions have a far greater contribution than the envelope function, $f(\mathbf{r})$, so in the next section we will calculate approximate transition matrix elements exclusively based on the atomic portion of the wavefunction [8].

Both the confinement potential and compressive in-plane strain of the dot break the degeneracy of the LH and HH bands that is present in bulk at k=0, however the HH and LH states remain closer to each other than any other low energy dot states [8]. The amount of mixing between two energy levels is influenced by their energy separation. Thus, the greatest amount of mixing among low energy states in InAs quantum dots occurs between the heavy and light hole states. The impact of this mixing on optical spectroscopy is simply that the polarization selection rules become elliptical instead of circular in the absence of a magnetic field. In a magnetic field the selection rules are normally linear and aligned with the magnetic field (as will be derived shortly), but the light hole-heavy hole mixing can rotate the alignment of the

still-linear polarizations [12]. Because the mixing only changes the polarization axes but not the possible interactions between states and has been observed to be small in the sample under discussion, this mixing effect will be neglected in the remainder of this work. Strain and confinement shift the HH band less than the LH band, leaving the HH band closer to the conduction band and more likely to be coupled by low energy optical excitations [8]. For this reason, the heavy-hole band will be the only valence band considered in these preliminary studies.

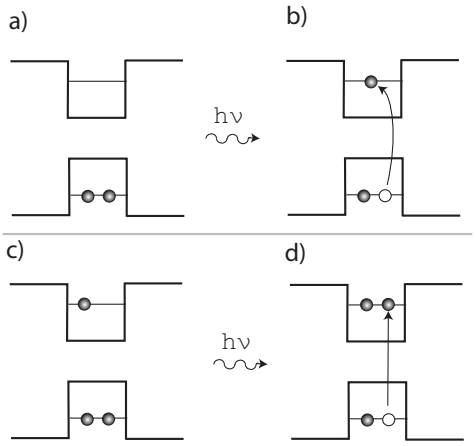

Figure 2.5: Quantum dot occupation diagrams for the a) neutral ground state, b) neutral excited state ("exciton"), c) charged ground state, and d) charged excited state ("trion")

Several occupation states of a single quantum dot are shown in Figure 2.5. These diagrams depict the heavy hole valence and conduction band of a quantum dot. In a neutral dot the ground state, a), consists of a full valence band and an empty conduction band. Diagram b) illustrates the corresponding photo-excited state, known as an "exciton", where an electron from the valence band is excited to the conduction band, leaving a hole in the valence band. In an exciton the conduction electron and valence hole are bound by their Coulomb attraction.

As discussed in Chapter 1, we are ultimately interested in manipulating spins in quantum dots, so we study charged quantum dots which possess a net spin. The ground and excited state of a charged dot are depicted in the lower half of Figure 2.5. The charged ground state, c), has one more electron than can fit in the valence band, so there is a single electron in the conduction band. The lowest energy excited state

for a charged dot is shown in d). This state, known as a negative trion (X^-), consists of an electron pair in the lowest conduction band bound to the hole left in the valence band.

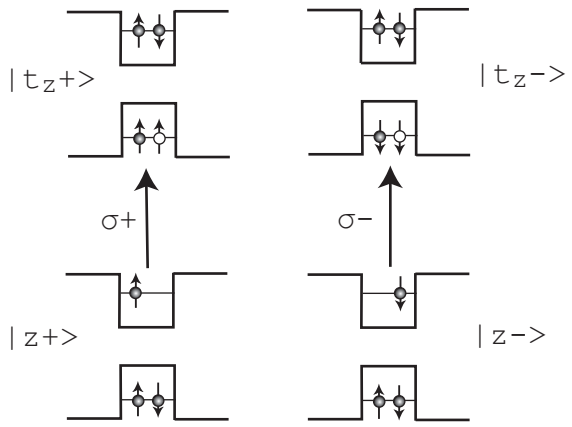

Figure 2.6: Allowed optical transitions in a charged dot in the absence of a magnetic field. The state labels reference that the axis of quantization is the z axis. $\sigma+$ and $\sigma-$ indicate the optical polarizations that satisfy the conservation of angular momentum for the allowed transitions.

The charged dot ground state valence band has pairs of spin up and spin down electrons, so the spin of the system is determined by the conduction band electron. This electron can have one of two spin states, shown in Figure 2.6 as $|z+\rangle$ and $|z-\rangle$. The growth direction is along z, and the states are labeled by the net angular momentum projection along z. Based on the calculations mentioned above of the dot states, the ground states are s-like, and the angular momentum projections are simply $+\frac{1}{2}$ or $-\frac{1}{2}$ for $|z+\rangle$ or $|z-\rangle$ respectively. If we examine the trion $|t_z+\rangle$ ($|t_z-\rangle$), we see that the spins in the conduction band cancel, but there is an unpaired hole in the p-like valence band, which carries an angular momentum of $+\frac{3}{2}$ ($-\frac{3}{2}$).

2.4 Optical Transitions in InAs Dots

Using these angular momentum assignments for the states we can calculate the allowed optical transitions. Since $\sigma+$ ($\sigma-$) circularly polarized light adds (subtracts) a unit of angular momentum from the system, the allowed transitions in the absence of

a magnetic field are as shown in Figure 2.6 and are characterized by a transition energy of $\hbar\omega_0$. This set of two uncoupled two-level systems does not allow for transitions between the two ground states of the system. Our goal is to optically manipulate the electron spin, but that would not be possible with these allowed transitions.

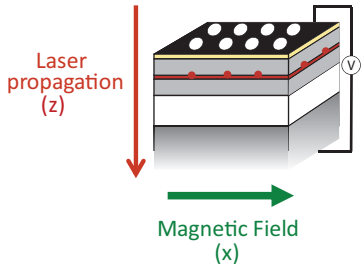

Figure 2.7: The laser propagates along the sample growth direction, which is labeled as the z axis. The magnetic field, applied perpendicular to the sample growth direction, defines the x axis.

A more suitable group of states is created when a magnetic field, B, is applied perpendicular to the growth direction (the so-called Voigt geometry), in what we will call the x direction. The Hamiltonian including the effect of the magnetic field can be written $\mathbf{H} = \mathbf{H}_0 + \mathbf{V}_{Zeeman}$ where

$$\mathbf{V}_{Zeeman} = -\boldsymbol{\mu}_{magnetic} \cdot \mathbf{B} = \mu_B(\mathbf{g}_e \cdot \mathbf{B} \cdot \mathbf{S}_e - \mathbf{g}_h \cdot \mathbf{B} \cdot \tilde{\mathbf{S}}_h), \tag{2.4}$$

$\mathbf{H}_0$ is the Hamiltonian of the dot in the absence of magnetic or optical fields, μ_B is the Bohr magneton, $\mathbf{g}_e$ ($\mathbf{g}_h$) is the g-factor tensor for the electron (hole), and heavy hole light hole mixing is neglected [13,14]. $\mathbf{S}_e$ is the angular momentum of the electron so

$$\mathbf{S}_e = \frac{\hbar}{2}\boldsymbol{\sigma} \tag{2.5}$$

where $\boldsymbol{\sigma} = \sigma_x\hat{x} + \sigma_y\hat{y} + \sigma_z\hat{z}$ and

$$\sigma_x = \begin{pmatrix} 0 & 1 \\ 1 & 0 \end{pmatrix} \quad \sigma_y = \begin{pmatrix} 0 & -i \\ i & 0 \end{pmatrix} \quad \sigma_z = \begin{pmatrix} 1 & 0 \\ 0 & -1 \end{pmatrix}. \tag{2.6}$$

$\tilde{\mathbf{S}}_h$ is the analogous pseudo-angular momentum of the hole in the convention used by Van Kesteren [15], namely that for a heavy hole with angular momentum $J_z = \pm\frac{3}{2}$,

$\tilde{S}_z = \pm\frac{1}{2}$. For $\mathbf{B} = B\hat{x}$,

$$\mathbf{V}_{Zeeman} = \frac{\mu_B B}{2} \begin{array}{c} \begin{matrix} |z+\rangle & |z-\rangle & |t_z+\rangle & |t_z-\rangle \end{matrix} \\ \begin{bmatrix} 0 & g_{e,x} & 0 & 0 \\ g_{e,x} & 0 & 0 & 0 \\ 0 & 0 & 0 & -g_{h,x} \\ 0 & 0 & -g_{h,x} & 0 \end{bmatrix} \end{array}. \tag{2.7}$$

The ground (trion) states are now mixed by the field, and the new eigenstates are split by the Zeeman effect by an amount $g_{e,x}\mu_B B = \hbar\Delta_e$ ($g_{h,x}\mu_B B = \hbar\Delta_h$). Rediagonalizing the Hamiltonian gives the new ground eigenstates as

$$|x\pm\rangle = \frac{1}{\sqrt{2}}(|z-\rangle \pm |z+\rangle) \tag{2.8}$$

with corresponding eigenenergies $E_{x\pm} = \pm\hbar\frac{\Delta_e}{2}$ and the new trion eigenstates as

$$|t_x\pm\rangle \equiv |t\pm\rangle = \frac{1}{\sqrt{2}}(|t_z-\rangle \pm |t_z+\rangle) \tag{2.9}$$

with eigenenergies $E_{t\pm} = \hbar(\omega_0 \mp \frac{\Delta_h}{2})$. (Interface fluctuation dots had a nearly zero hole in-plane g factor, $g_{h\perp}$, so in those dots mixing of the trion states could be neglected [16].)

Computing the optically allowed transitions requires writing the Hamiltonian for optical interactions, $\mathbf{H}_{optical}$, and then asking which matrix elements $\langle a|\mathbf{H}_{optical}|b\rangle$ are nonzero for two non-identical states, $|a\rangle$ and $|b\rangle$.

$$\langle a|\mathbf{H}_{optical}|b\rangle = \langle a|\mathbf{H}_0|b\rangle + \langle a|\mathbf{V}_{optical}|b\rangle = E_a\delta_{a,b} + \langle a|\mathbf{V}_{optical}|b\rangle \tag{2.10}$$

In the dipole approximation, the interaction for an optical field can be written as

$$\mathbf{V}_{optical} = -\boldsymbol{\mu}\cdot\mathbf{E} = e\mathbf{r}\cdot\mathbf{E} \tag{2.11}$$

where e is a positive number giving the magnitude of an electron's charge. Since $\mathbf{E}$ does not operate upon the state vectors, it is sufficient to evaluate $\langle a|\mathbf{r}|b\rangle$ to determine the optically allowed transitions and their polarization selection rules.

In terms of irreducible spherical tensors

$$\mathbf{r} = -r_{-1}\boldsymbol{\epsilon}_{+1} - r_{+1}\boldsymbol{\epsilon}_{-1} + r_0\boldsymbol{\epsilon}_0 \tag{2.12}$$

where

$$\boldsymbol{\epsilon}_{\pm 1} = \mp\frac{(\hat{x} \pm i\hat{y})}{\sqrt{2}}, \quad \boldsymbol{\epsilon}_0 = \hat{z}. \tag{2.13}$$

Since the allowed optical transitions are dictated by angular momentum conservation, it is easier if we relabel the z basis states (the eigenstates in the absence of a field) with their angular momentum values:

$$|z-\rangle = |-\tfrac{1}{2}\rangle, \quad |z+\rangle = |\tfrac{1}{2}\rangle, \quad |t_z+\rangle = |\tfrac{3}{2}\rangle, \quad |t_z-\rangle = |-\tfrac{3}{2}\rangle. \tag{2.14}$$

Then

$$\begin{gathered} \langle \tfrac{3}{2}|\mathbf{r}|\tfrac{1}{2}\rangle = e\langle \tfrac{3}{2}|r_{+1}\boldsymbol{\epsilon}_{-1}|\tfrac{1}{2}\rangle \equiv \wp\boldsymbol{\epsilon}_{-1} \\ \langle \tfrac{3}{2}|\mathbf{r}|-\tfrac{1}{2}\rangle = 0 \\ \langle -\tfrac{3}{2}|\mathbf{r}|-\tfrac{1}{2}\rangle = e\langle \tfrac{3}{2}|r_{-1}\boldsymbol{\epsilon}_{+1}|\tfrac{1}{2}\rangle = \wp\boldsymbol{\epsilon}_{+1} \\ \langle -\tfrac{3}{2}|\mathbf{r}|\tfrac{1}{2}\rangle = 0, \end{gathered} \tag{2.15}$$

which confirms the polarizations of the optical transitions shown in Figure 2.6.

Combining Equations 2.8, 2.9, and 2.15 gives the selection rules for optical transitions in a magnetic field:

$$\begin{gathered} \langle t+|\mathbf{r}|x+\rangle = -\tfrac{\wp}{\sqrt{2}}i\hat{y} \\ \langle t-|\mathbf{r}|x-\rangle = -\tfrac{\wp}{\sqrt{2}}i\hat{y} \\ \langle t+|\mathbf{r}|x-\rangle = -\tfrac{\wp}{\sqrt{2}}\hat{x} \\ \langle t-|\mathbf{r}|x+\rangle = -\tfrac{\wp}{\sqrt{2}}\hat{x}. \end{gathered} \tag{2.16}$$

Due to the mixing of both ground and trion states, the optical selection rules are rather different from the B=0 case and lead to the four level system shown in Figure 2.8 which now involves transitions stimulated by linearly polarized light. The two ground states, which are the two levels of our spin-based qubit, can now be coupled via either trion state.

The Hamiltonian for this four level system in the presence of a Voigt magnetic field can be written

$$\mathbf{H}_{normal} = \begin{bmatrix} \frac{\hbar}{2}(-\omega_0 - \Delta_e) & V_{12} & V_{13} & V_{14} \\ V_{12}^* & \frac{\hbar}{2}(-\omega_0 + \Delta_e) & V_{23} & V_{24} \\ V_{13}^* & V_{23}^* & \frac{\hbar}{2}(\omega_0 - \Delta_h) & V_{34} \\ V_{14}^* & V_{24}^* & V_{34}^* & \frac{\hbar}{2}(\omega_0 + \Delta_h) \end{bmatrix}, \tag{2.17}$$

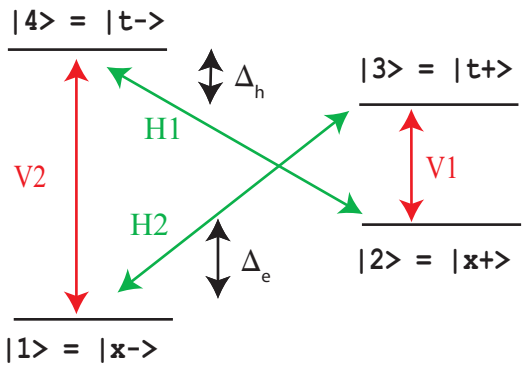

Figure 2.8: Allowed optical transitions in a charged dot with a magnetic field in the Voigt geometry. V1 and V2 are the $\hat{y}$ or vertically polarized transitions, and H1 and H2 are the $\hat{x}$ or horizontally polarized transitions. All four eigenstates are now defined along the x axis, and numerical labels are defined as a shorthand to refer to the four states.

where $V_{ij} = \langle i|\mathbf{V}_{optical}|j\rangle$ and the time dependence of the probability amplitudes is given by

$$i\hbar\dot{\mathbf{a}}(t) = \mathbf{H}\mathbf{a}(t). \tag{2.18}$$

We are interested in optical interactions, so we define a general electric field and substitute $\mathbf{V}_{optical} = -\boldsymbol{\mu}\cdot\mathbf{E}$ into Equation 2.17 as the interaction Hamiltonian. Since the transitions are linearly polarized, we define the electric field conveniently as

$$\mathbf{E}(t) = \frac{1}{2}(E_x(t)\hat{x} + E_y(t)\hat{y})e^{-i\omega t} + \frac{1}{2}(E_x^*(t)\hat{x} + E_y^*(t)\hat{y})e^{i\omega t}. \tag{2.19}$$

Most of our experiments use pulses that have broad enough bandwidth that they couple all four optical transitions. We evaluate the Hamiltonian and related equations under this assumption. If a narrower bandwidth laser is used, then the V terms representing uncoupled states should be set to zero. Then we can evaluate the Hamiltonian terms, for example H_{13}. From Equations 2.16, 2.17, and 2.19,

$$\begin{aligned} H_{13} =& -\langle x-|\boldsymbol{\mu}|t+\rangle\cdot\mathbf{E}(t) \\ =& \frac{\wp}{2\sqrt{2}}(E_x(t)e^{-i\omega t} + E_x^*(t)e^{i\omega t}) \\ =& \frac{\hbar}{2}(\Omega_x(t)e^{-i\omega t} + \Omega_x^*(t)e^{i\omega t}) \end{aligned} \tag{2.20}$$

defining the convenient notation

$$\Omega_x(t) \equiv \tfrac{\wp E_x(t)}{\hbar\sqrt{2}} \quad \Omega_y(t) \equiv \tfrac{i\wp E_y(t)}{\hbar\sqrt{2}}. \tag{2.21}$$

If we move to a rotating reference frame called the field interaction picture, where

$$\mathbf{c}(t) = \begin{bmatrix} e^{\frac{i\omega t}{2}} & 0 & 0 & 0 \\ 0 & e^{\frac{i\omega t}{2}} & 0 & 0 \\ 0 & 0 & e^{\frac{-i\omega t}{2}} & 0 \\ 0 & 0 & 0 & e^{\frac{-i\omega t}{2}} \end{bmatrix} \mathbf{a}(t) \tag{2.22}$$

and

$$\delta \equiv \omega_0 - \omega, \tag{2.23}$$

then the Hamiltonian becomes

$$\mathbf{H}_{FI} = \begin{bmatrix} -\frac{\hbar}{2}(\delta + \Delta_e) & V_{12} & V_{13}e^{-i\omega t} & V_{14}e^{-i\omega t} \\ V_{12}^* & \frac{\hbar}{2}(-\delta + \Delta_e) & V_{23}e^{-i\omega t} & V_{24}e^{-i\omega t} \\ V_{13}^* e^{i\omega t} & V_{23}^* e^{i\omega t} & \frac{\hbar}{2}(\delta - \Delta_h) & V_{34} \\ V_{14}^* e^{i\omega t} & V_{24}^* e^{i\omega t} & V_{34}^* & \frac{\hbar}{2}(\delta + \Delta_h) \end{bmatrix} \tag{2.24}$$

and

$$i\hbar\dot{\mathbf{c}}(t) = \mathbf{H}_{FI}\mathbf{c}(t). \tag{2.25}$$

In the field interaction picture,

$$H_{13} = \frac{\hbar}{2}(\Omega_x(t)e^{-2i\omega t} + \Omega_x^*(t)). \tag{2.26}$$

If $|\frac{\Omega_x(t)}{\omega_0+\omega}| \ll 1$ and $|\frac{\omega_0-\omega}{\omega_0+\omega}| \ll 1$, then we can neglect terms that oscillate at 2ω, as they will average out to zero over times short compared to other timescales in the problem. This is known as the rotating wave approximation (RWA). In the RWA,

$$H_{13} = \frac{\hbar\Omega_x^*}{2}. \tag{2.27}$$

Similar evaluations give

$$\mathbf{H}_{FI,RWA} = \frac{\hbar}{2}\begin{bmatrix} -\delta - \Delta_e & 0 & \Omega_x^*(t) & \Omega_y^*(t) \\ 0 & -\delta + \Delta_e & \Omega_y^*(t) & \Omega_x^*(t) \\ \Omega_x(t) & \Omega_y(t) & \delta - \Delta_h & 0 \\ \Omega_y(t) & \Omega_x(t) & 0 & \delta + \Delta_h \end{bmatrix}. \tag{2.28}$$

Therefore the equations of motion for the probability amplitudes are

$$\begin{aligned}
\dot{c}_1(t) &= \tfrac{i}{2}[(\delta+\Delta_e)c_1(t) - \Omega_x^*(t)c_3(t) - \Omega_y^*(t)c_4(t)] \\
\dot{c}_2(t) &= \tfrac{i}{2}[(\delta-\Delta_e)c_2(t) - \Omega_y^*(t)c_3(t) - \Omega_x^*(t)c_4(t)] \\
\dot{c}_3(t) &= \tfrac{i}{2}[-\Omega_x(t)c_1(t) - \Omega_y(t)c_2(t) + (-\delta+\Delta_h)c_3(t)] \\
\dot{c}_4(t) &= \tfrac{i}{2}[-\Omega_y(t)c_1(t) - \Omega_x(t)c_2(t) + (-\delta-\Delta_h)c_4(t)].
\end{aligned} \tag{2.29}$$

In order to properly include decay and dephasing processes, it is necessary to use the density matrix formalism, which is defined (in the field interaction picture) by

$$\rho_{ij}(t) = c_i(t)c_j^*(t). \tag{2.30}$$

The time evolution of the density matrix is given by

$$i\hbar\dot{\boldsymbol{\rho}} = [\mathbf{H}, \boldsymbol{\rho}] = \mathbf{H}\boldsymbol{\rho} - \boldsymbol{\rho}\mathbf{H} \tag{2.31}$$

Including decay, the field interaction density matrix equations for the four level system shown in Figure 2.8 are

$$\begin{aligned}
\dot{\rho}_{11} &= \tfrac{i}{2}\left(\rho_{13}\Omega_x + \rho_{14}\Omega_y - \rho_{31}\Omega_x^* - \rho_{41}\Omega_y^*\right) + \tfrac{\Gamma_t}{2}(\rho_{44}+\rho_{33}) + \Gamma_e(\rho_{22}-\rho_{11}) \\
\dot{\rho}_{22} &= \tfrac{i}{2}\left((\rho_{23}+\rho_{24})\,\Omega_y - \rho_{42}\Omega_x^* - \rho_{32}\Omega_y^*\right) + \tfrac{\Gamma_t}{2}(\rho_{44}+\rho_{33}) + \Gamma_e(\rho_{11}-\rho_{22}) \\
\dot{\rho}_{33} &= -\tfrac{i}{2}\left(\rho_{13}\Omega_x + \rho_{23}\Omega_y - \rho_{31}\Omega_x^* - \rho_{32}\Omega_y^*\right) - \Gamma_t\rho_{33}) + \Gamma_h(\rho_{44}-\rho_{33}) \\
\dot{\rho}_{44} &= -\tfrac{i}{2}\left((\rho_{14}+\rho_{24})\,\Omega_y - \rho_{42}\Omega_x^* - \rho_{41}\Omega_y^*\right) - \Gamma_t\rho_{44}) + \Gamma_h(\rho_{33}-\rho_{44}) \\
\dot{\rho}_{12} &= \tfrac{i}{2}\left(2\Delta_e\rho_{12} + (\rho_{13}+\rho_{14})\,\Omega_y - \rho_{32}\Omega_x^* - \rho_{42}\Omega_y^*\right) - \gamma_e\rho_{12} \\
\dot{\rho}_{13} &= \tfrac{i}{2}\left((2\delta+\Delta_e-\Delta_h)\,\rho_{13} + (\rho_{11}-\rho_{33})\,\Omega_x^* + (\rho_{12}-\rho_{43})\,\Omega_y^*\right) - \gamma_t\rho_{13} \\
\dot{\rho}_{14} &= \tfrac{i}{2}\left((2\delta+\Delta_e+\Delta_h)\,\rho_{14} + (\rho_{12}-\rho_{34})\,\Omega_x^* + (\rho_{11}-\rho_{44})\,\Omega_y^*\right) - \gamma_t\rho_{14} \\
\dot{\rho}_{23} &= \tfrac{i}{2}\left((2\delta-\Delta_e-\Delta_h)\,\rho_{23} + (\rho_{21}-\rho_{43})\,\Omega_x^* + (\rho_{22}-\rho_{33})\,\Omega_y^*\right) - \gamma_t\rho_{23} \\
\dot{\rho}_{24} &= \tfrac{i}{2}\left((2\delta-\Delta_e+\Delta_h)\,\rho_{24} + (\rho_{22}-\rho_{44})\,\Omega_x^* + (\rho_{21}-\rho_{34})\,\Omega_y^*\right) - \gamma_t\rho_{24} \\
\dot{\rho}_{34} &= \tfrac{i}{2}\left(2\Delta_h\rho_{34} - \rho_{14}\Omega_x - \rho_{24}\Omega_y + \rho_{32}\Omega_x^* + \rho_{31}\Omega_y^*\right) - \gamma_h\rho_{34}.
\end{aligned} \tag{2.32}$$

From definitions 2.30 and 2.31 it is clear that

$$\rho_{ji}(t) = \rho_{ij}^*(t). \tag{2.33}$$

Population decay is included through the trion decay rate (Γ_t), the electron spin flip rate (Γ_e), and the hole spin flip rate (Γ_h), while γ terms indicate decoherence rates.

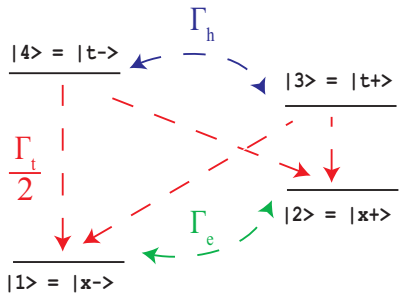

Figure 2.9: Definition of the decay rates among the four levels of interest in the dot. Γ_e (Γ_h) represents electron (hole) spin flip processes, and Γ_t represents recombination of an electron and hole.

The population decays are shown in Figure 2.9. In the absence of pure dephasing, $\gamma_t \approx \frac{\Gamma_t}{2}$, $\gamma_e = \Gamma_e$ and $\gamma_h = \Gamma_h$.

2.5 Dot Characterization

Because the growth of self-assembled dots is a stochastic process, each sample has a range of dot densities and dot transition energies. Before attempting any manipulations or spectroscopy toward the goal of quantum computing, a usable dot must be found and characterized. All measurements in this dissertation were taken with the sample in a continuous-flow helium cryostat which maintains the sample temperature at 5 K.

2.5.1 Photoluminescence

The first step of characterization is to take photoluminescence (PL) data from several different apertures. In PL we excite the system non-resonantly, significantly above the state of interest. The system then non-radiatively relaxes and the luminescence from a lower energy transition is detected (See Figure 2.10). PL measurements are made with a single non-mode-locked Coherent Mira Titanium-Sapphire laser that is tuned to 780 nm and pumped by a Coherent Verdi. The transmitted beam is collected and refocused into a spectrometer. The spectrum is collected on a liquid nitrogen cooled CCD at the spectrometer's image plane (see Figure 2.11).

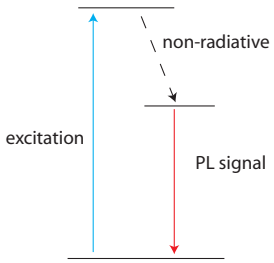

Figure 2.10: Energy transitions involved in photoluminescence characterization measurements. The dot is excited far above the transition of interest, the system relaxes through a non-radiative process, then photoluminescence is emitted from the lower energy transition.

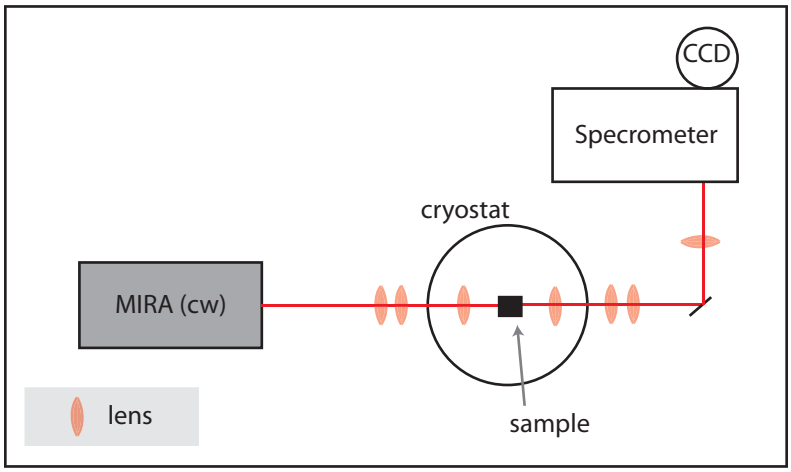

Figure 2.11: Experimental diagram for photoluminescence measurements. The MIRA Titanium:Sapphire laser is used in its non-modelocked, quasi-continuous wave mode. The MIRA is tuned to 780 nm and focused onto the aperture of interest on the sample, which is kept at 5 Kelvin in a liquid helium cryostat. The photoluminescence spectra are collected with a spectrometer and a liquid nitrogen cooled CCD array.

For a given scan, the sample bias voltage is held constant, and the spectrometer wavelength is scanned by a computer controlled motor. A map of voltage vs. energy is obtained by taking a series of these scans at incremental voltages. A desirable aperture will have either only one dot or a couple of dots that are well separated in transition energies. A dot must have a voltage range where the ground state to trion transition is observable, so that we know that the dot can be charged with a single electron. Often we identify dots and trion states by the characteristic separation

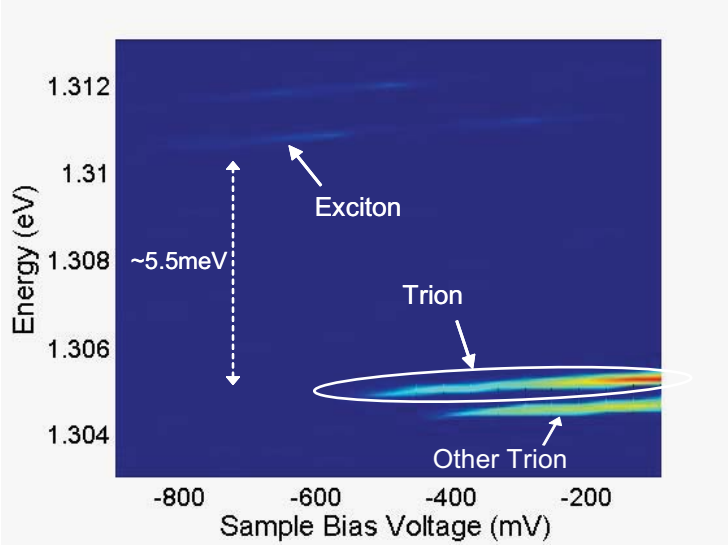

Figure 2.12: Subsection of a photoluminescence map through a single aperture. The trion of interest is labeled, as well as what is most likely the corresponding exciton, which is located 5.5 meV away.

between the exciton and trion, which is typically about 6 meV for our samples. Most of the expertise regarding identification of optical dot transitions from PL spectra was developed by Dan Gammon's group at the Naval Research Lab. An important parameter that can be measured from PL is the slope of the energy of the states with respect to voltage, which is due to the DC Stark effect [17]. A map showing the aperture of interest is shown in Figure 2.12. All data presented in this dissertation is from the circled trion.

2.5.2 CW Modulated Absorption

As described above, PL measurements are an indirect, off-resonant method of probing a state. In continuous wave (CW) absorption we scan the CW Coherent 899-21 Ti:Saph laser across the transition's energy, as estimated by the PL map. The sample's bias is modulated a small amount (.01 V) at around 1 kHz. Because of the DC Stark effect (observed in PL), modulating the bias voltage modulates the detuning of the laser from the state, therefore modulating the absorption strength. Bias modulation allows phase-sensitive detection with a lock-in. The transmitted light

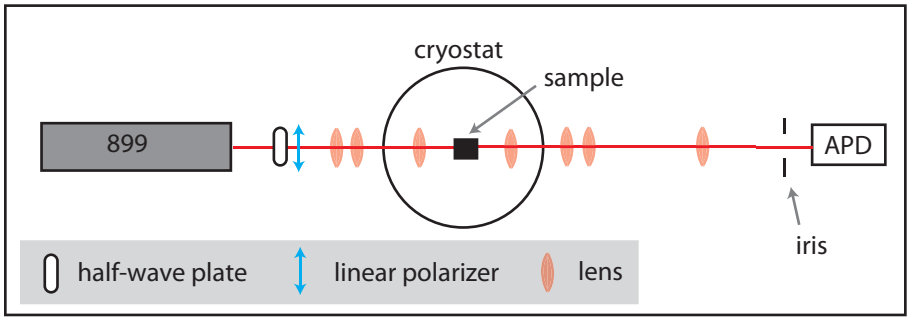

Figure 2.13: The experimental layout for modulated absorption measurements. The frequency-stabilized, continuous wave 899 Titanium:Sapphire laser is passed through a half-wave plate and linear polarizer to achieve any desired linear polarization, and then focused onto the aperture of interest. The transmitted light is collected by lenses and focused onto a silicon avalanche photodiode. Scattered light from adjacent apertures can be spatially blocked with an iris.

is focused onto a silicon avalanche photodetector, as shown in Figure 2.13, which is connected to the lock-in amplifier. By taking these scans at a range of DC bias values, it is possible to make a map of the energy and voltage range where the state absorbs (Figure 2.14).

With this voltage modulation method, if the modulation amplitude is much less than the transition linewidth, then the signal will be the derivative of the absorption line shape [18]. For the measurements in this work, the modulation amplitude is on the order of the transition linewidth. This means that the measured signal will have a distorted lineshape that is neither the actual lineshape nor exactly the derivative of the lineshape. At higher modulation amplitudes the phase of the absorption signal seems to have a bias dependence, meaning that that there is no lock-in phase such that all of the signal will be in a single channel. We chose our modulation amplitude to obtain the maximum signal amplitude without inducing this problematic phase artifact. Luckily, in all of the measurements discussed here, we are concerned with the magnitude of the absorption rather than the lineshape, so the distortion caused by the modulation is tolerable. With no magnetic field, all energy transitions within our four level system are degenerate, so only one absorption signal is observed (Figure 2.14).

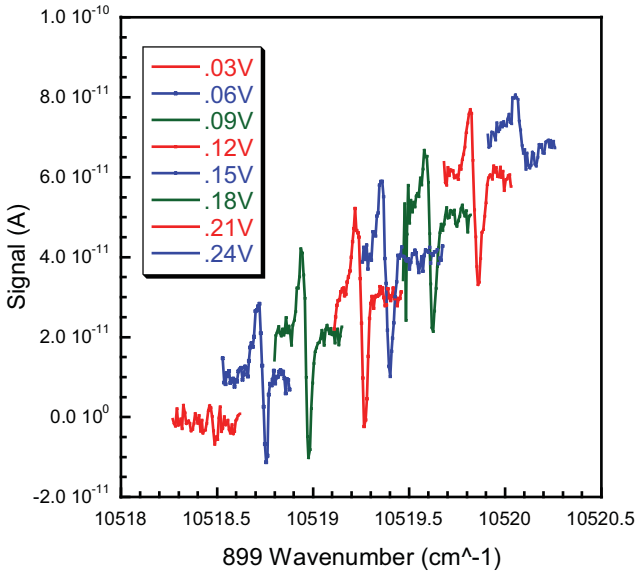

Figure 2.14: A series of cw bias modulated absorption scans taken at varying DC sample bias voltages, that show the voltage existence range of the state. (Data taken with Erik Kim.)

2.5.3 Absorption studies with a magnetic field

When a magnetic field is applied in the Voigt geometry and the laser polarization contains both H and V polarizations, we expect to see four separate transitions, as shown in Figure 2.8. Figure 2.15 shows the actual absorption data for our dot in a 0.66 Tesla field with 45 degree polarized light. At 0.06 V four derivative-like signals are present, but at 0.14 V, for example, there is only one broad feature. This behavior is caused by a process called optical pumping, which was first proposed by Alfred Kastler in 1950 in atomic systems [19, 20]. Xiaodong Xu first demonstrated optical pumping in the Voigt geometry in self-assembled dots, and demonstrated that it can be used for initialization [21]. In Chapter 3, we discuss initialization via optical pumping. Here we explain the effect and the measured absorption signals.

Figure 2.14 shows that there is a certain voltage range (0.06-0.22 V) over which the ground to trion transition absorbs. In the middle of this absorption voltage

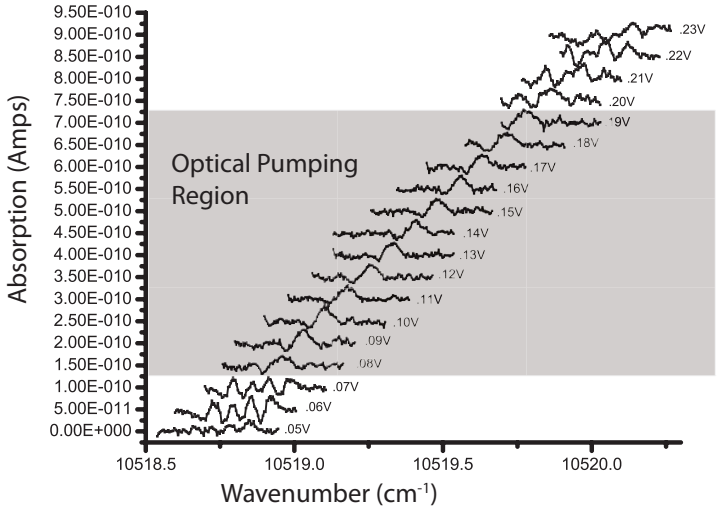

Figure 2.15: Modulated absorption of the trion studied in this thesis in a 0.66 Tesla magnetic field and for a range of bias voltages. Notice that all four transitions are observable on the edge of the bias range, while only a single broad peak is observed in the central, optical pumping, region.

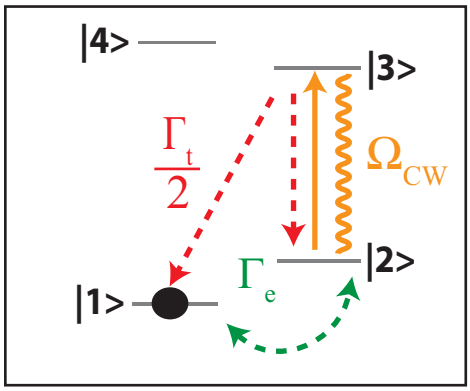

Figure 2.16: Illustration of the optical pumping process for a CW field tuned to the $|2\rangle$ to $|3\rangle$ transition.

range Γ_e is on the order of 10^3 s^{-1} [22]. This is much smaller than Γ_t, which is on the order of 10^9 s^{-1} [23]. Because $\Gamma_t \gg \Gamma_e$ optical pumping can occur. As an example of how optical pumping occurs in this system, consider the case shown in Figure 2.16 where a CW laser is driving the $|2\rangle$ to $|3\rangle$ transition. The CW laser optically excited population from $|2\rangle$ to $|3\rangle$ at a rate Ω_{CW}. Simultaneously, trion decay causes transitions at the rate $\frac{\Gamma_t}{2}$ to both ground states with equal probability. However, once the system decays to state $|1\rangle$ it can no longer be optically excited, so the dot is trapped in state $|1\rangle$ until a spin-flip occurs to transition back to state $|2\rangle$.

If $\Omega_{CW} \gg \Gamma_t$, optical pumping occurs within a few trion radiative lifetimes, so when $\Gamma_t \gg \Gamma_e$ the system spends most of the time in the non-optically coupled state ($|1\rangle$), and absorption is suppressed [21]. Note that if the laser frequency is being scanned, absorption is suppressed on each transition since each transition will optically pump within a few nanoseconds of the laser tuning into resonance. The data show a single broad feature in the optical pumping region because the middle two transitions, the $\hat{x}$ polarized transitions, are not resolved. This means that the laser is simultaneously driving both $\hat{x}$ transitions, so optical pumping cannot occur and a broad peak is observed. The outer, $\hat{y}$, transitions' absorption is suppressed as expected.

Near the edges of the absorption voltage existence range, the electron is far less stable in the dot. The rate of tunneling between the dot and the Fermi sea is higher, which leads to a higher spin-flip rate, $\Gamma_e \approx \Gamma_t$. This prevents population trapping in state $|1\rangle$, since the spin-flip process interchanges between states $|1\rangle$ and $|2\rangle$ at a rate equal to the trion decay. In such voltage ranges moderately strong absorption can be observed, so this is the simplest way to observe the four dot transitions. However, any manipulations for quantum computing need to be performed in the center of the existence range to avoid the increased tunneling rates at the edge of the the range, as spin flips destroy any information contained in the spin qubit. For this reason all data in later chapters is taken in the middle of the optical pumping region.

Figure 2.17 shows the four transitions more clearly at 1.32 Tesla in the non-optical pumping region, again using 45 degree polarized light. This supports our identification of the state as a trion, and our energy level diagram as shown in Figure 2.8. The splitting of these four peaks as a function of magnetic field strength can be used to measure the electron and hole in-plane g-factors, since the electron (hole) splitting is given by $g_{e\perp}\mu_B B_x$ ($g_{h\perp}\mu_B B_x$). Figure 2.18 shows a plot of the splittings. Measurement of the slopes results in an electron in-plane g-factor of 0.42 and a hole in-plane g-factor of 0.24.

In each scan of Figure 2.16 and 2.17, the DC bias voltage was held constant and the laser energy was scanned. Similar data could be obtained by keeping the laser energy fixed and scanning the DC bias voltage, due to the DC Stark effect. One

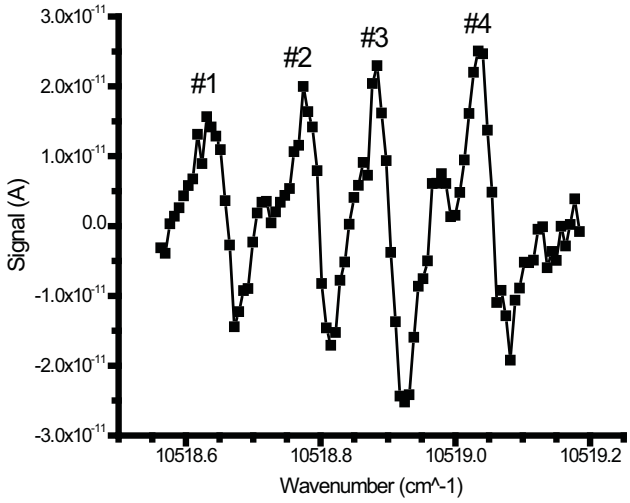

Figure 2.17: A CW modulated absorption scan clearly showing all four transitions, taken at 1.32 Tesla in the non-optical pumping region with 45 degree polarized light. (Data taken with Erik Kim.)

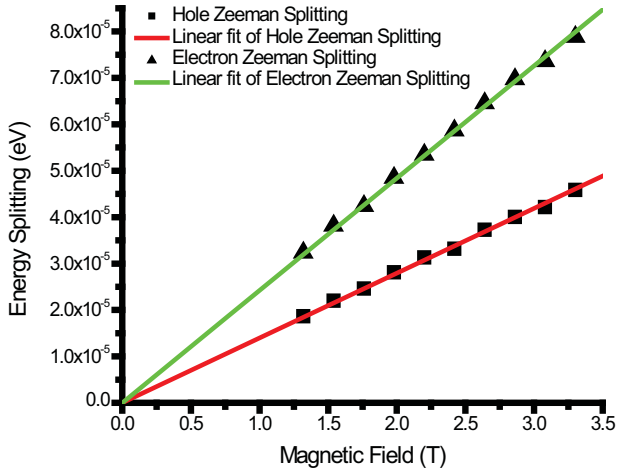

Figure 2.18: Zeeman splittings plotted as a function of current applied to the magnet. The magnetic field strength, B, in Teslas is given by $B = 0.11 * I$ where I is the current applied. The electron (hole) splitting is the difference between peaks 2 (3) and 4 in Figure 2.17. (Data taken with Erik Kim.)

must be careful when switching between these two methods, however, as the order of peaks is different in the two methods. For clarification, refer to Figure 2.19. The leftmost graph represents absorption existence ranges for two transitions plotted as laser energy vs. bias voltage with positively-sloped linear DC Stark effects assumed.

The other two graphs show the order in which the peaks appear when the voltage or the laser energy is scanned. Notice that in the voltage scan transition A appears on the left but in the energy scan transition B appears on the left.

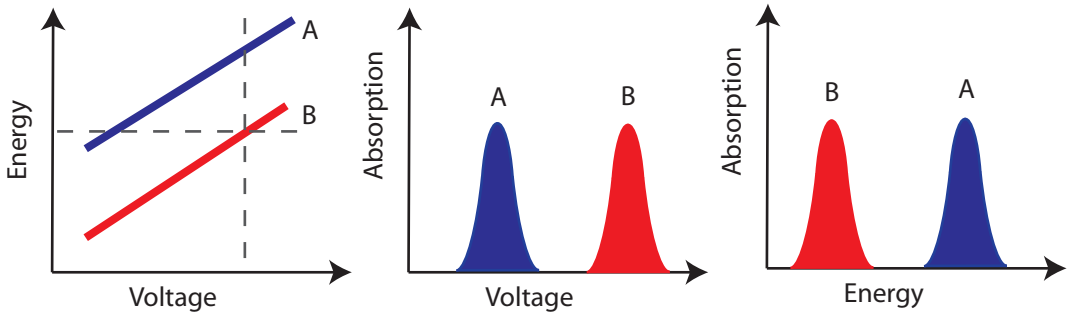

Figure 2.19: The leftmost graph represents the absorption existence ranges in voltage and energy of two transitions. The dotted lines represent a laser energy scan and a bias voltage scan. Notice that in the voltage scan transition A appears on the left but in the energy scan transition B appears on the left.

2.6 Chapter Summary

This chapter provided an introduction to the quantum dot samples and their optical properties. The sample structure was presented in detail, including an explanation of dot charging with a diode structure. Relevant energy levels of the dots were presented and related to energy bands in bulk semiconductors. The new energy eigenstates were calculated in the presence of a Voigt magnetic field, and the optically allowed transitions were calculated with and without the magnetic field. Equations of motion for a four level trion system were developed in both the probability amplitude and density matrix formalisms. These equations provide the basis for theoretical calculations that will be discussed in later chapters. Finally, initial dot characterization measurements were discussed, including PL and CW modulated absorption. Optical pumping was introduced as it relates to absorption studies. Measurements of the trion existence range, DC Stark effect, optical pumping region, and g-factor were presented. This chapter established the theoretical and experimental background necessary to discuss optical manipulations of the spin qubit. The next chapter discusses coherent

control of a single spin qubit.

BIBLIOGRAPHY

BIBLIOGRAPHY

[1] P. M. Petroff, A. Lorke, A. Imamoglu, "Epitaxially Self-Assembled Quantum Dots", *Physics Today* **54**, 46 (2001).

[2] T. H. Stievater, X. Li, D. G. Steel, D. Gammon, D. S. Katzer, D. Park, C. Piermarocchi, L. J. Sham, "Rabi oscillations of excitons in single quantum dots.", *Physical Review Letters* **87**, 133603 (2001).

[3] J. R. Guest, T. H. Stievater, X. Li, J. Cheng, D. G. Steel, D. Gammon, D. Katzer, D. Park, C. Ell, A. Thrnhardt, et al., "Measurement of optical absorption by a single quantum dot exciton", *Physical Review B* **65**, 1 (2002).

[4] M. E. Ware, A. Bracker, D. Gammon, D. Gershoni, "Polarization Spectroscopy of Charged Single Self-Assembled Quantum Dots", *Mat. Res. Soc. Symp. Proc.* **794** (2004).

[5] H. Drexler, D. Leonard, W. Hansen, J. Kotthaus, P. Petroff, "Spectroscopy of Quantum Levels in Charge-Tunable INGaAs Quantum Dots", *Phys. Rev. Lett.* **73** (1994).

[6] J. Dreiser, M. Atature, C. Galland, T. Muller, A. Badolato, A. Imamoglu, "Optical investigations of quantum-dot spin dynamics", *arXiv:0705.3557v1[cond-mat.mes-hall]* (2007).

[7] N. W. Ashcroft, N. D. Mermin, *Solid State Physics*, volume 10, Brooks Cole (1976).

[8] J. Singh, *Physics of Semiconductors and their Heterostructures*, McGraw-Hill Education, Hoboken, NJ, first edition, ISBN 0071128352 (1993).

[9] C. Kittel, *Introduction to Solid State Physics*, John Wiley and Sons, Inc., Hoboken, NJ, seventh edition, p.206-213 (1996).

[10] A. J. Williamson, A. Zunger, "InAs quantum dots: Predicted electronic structure of free-standing versus GaAs-embedded structures", *Physical Review B* **59**, 15819 (1999).

[11] O. Stier, M. Grundmann, D. Bimberg, "Electronic and optical properties of strained quantum dots modeled by 8-band kp theory", *Physical Review B* **59**, 5688 (1999).

[12] X. Xu, *Coherent optical spectroscopy of a single semiconductor quantum dot*, Ph.D. thesis, The University of Michigan, The Harrison M. Randall Laboratory of Physics, Ann Arbor MI 48109-1120 (2008).

[13] G. L. Bir, G. E. Pikus, *Symmetry and Strain-Induced Effect in Semiconductors* (1974).

[14] R. Winkler, "Spin Orbit Coupling Effects in Two-Dimensional Electron and Hole Systems", *New York* **23**, 211223 (2003).

[15] H. Van Kesteren, E. Cosman, W. Van Der Poel, C. Foxon, "Fine structure of excitons in type-II GaAs/AlAs quantum wells", *Physical Review B* **41**, 5283 (1990).

[16] J. G. Tischler, A. S. Bracker, D. Gammon, D. Park, "Fine Structure of Trions and Excitons in Single GaAs Quantum Dots", *Phys. Rev. B* **66**, 081310 (2002).

[17] R. J. Warburton, C. Schulhauser, D. Haft, C. Schäflein, K. Karrai, J. M. Garcia, W. Schoenfeld, P. M. Petroff, "Giant permanent dipole moments of excitons in semiconductor nanostructures", *Phys. Rev. B* **65**, 113303 (2002).

[18] B. Alen, F. Bickel, K. Karrai, R. J. Warburton, P. M. Petroff, "Stark-shift modulation absorption spectroscopy of single quantum dots", *Appl. Phys. Lett.* **83** (2003).

[19] A. Kastler, "Quelques suggestions concernant la production optique et la dtection optique dune ingalit de population des niveaux de quantification spatiale des atomes", *JPhysRad* **11**, 255 (1950).

[20] J. Brossel, A. Kastler, J. Winter, "Greation Optique Dune Inegalite De Population Entre Les Sous-Niveaux Zeeman De Letat Fondamental Des Atomes", *Journal de Physique et le Radium* **13**, 668 (1952).

[21] X. Xu, Y. Wu, B. Sun, Q. Huang, J. Cheng, D. G. Steel, A. S. Bracker, D. Gammon, C. Emary, L. J. Sham, "Fast Spin State Initialization in a Singly-Charged InAs-GaAs Quantum Dot by Optical Cooling", *Phys. Rev. Lett.* **99**, 097401 (2007).

[22] M. Kroutvar, Y. Ducommun, D. Heiss, M. Bichler, D. Schuh, G. Abstreiter, J. J. Finley, "Optically programmable electron spin memory using semiconductor quantum dots", *Nature* **432** (2004).

[23] E. D. Kim, K. Truex, A. Amo, X. Xu, D. G. Steel, A. S. Bracker, D. Gammon, L. J. Sham, "Picosecond optical spectroscopy of a single negatively charged self-assembled InAs quantum dot", *APL* **97**, 113110 (2010).

CHAPTER 3

Coherent Control of a Single Spin Qubit[1]

3.1 Introduction

Demonstration of a universal set of gates is one of the requirements for quantum computing, as presented in Chapter 1 [2]. Single qubit gates are the simplest, and thus a starting point for demonstrating the feasibility of our spin qubits. The most general single qubit gate, the arbitrary rotation, can be accomplished via rotation by an arbitrary angle about two orthogonal axes [3]. For our system, a single qubit rotation consists of a rotation of the electron spin vector. In terms of our four level energy diagram, it means coherently transferring an arbitrary probability of occupation from one ground state to the other.

To demonstrate or evaluate any manipulation, it is necessary to start in a well defined state. The first section of this chapter describes how we initialize the qubit before the coherent manipulation. The second section explains the readout method used to detect the state of the system after the manipulation. The third section establishes the basic theory of optical excitation of a two level system and explains why coherently controlling the spin in a useful manner for quantum computing is non-trivial. The final sections describe demonstrated methods of coherently controlling the electron spin: optically via Raman transitions, via precession about a magnetic field, and via optically induced geometric phases.

[1]The results presented in this chapter represents a joint effort with senior graduate student Erik Kim. The experimental data from Sections 3.5-3.7 were published in Physical Review Letters [1].

3.2 CW Initialization

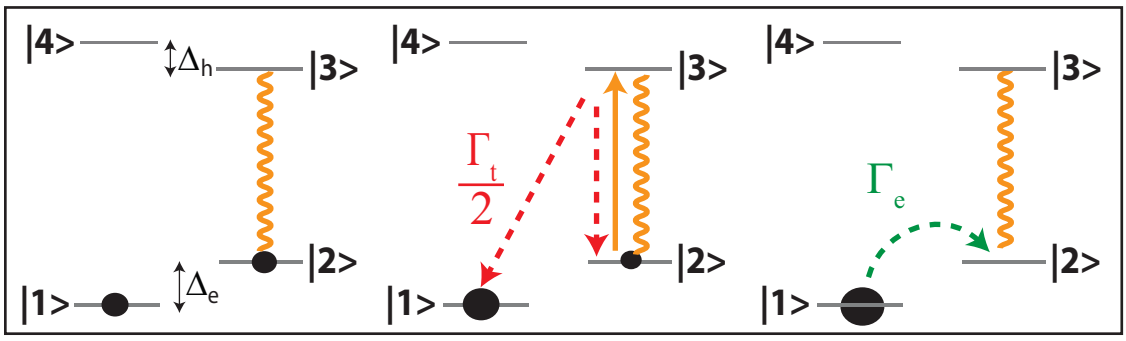

Figure 3.1: Illustration of the optical pumping process for a CW field tuned to the $|2\rangle$ to $|3\rangle$ transition.

When developing qubit rotations or other procedures, it is important for manipulations to be deterministic, so the system must be initialized. The spin state of a charged quantum dot is naturally a mixed state of $|\uparrow\rangle$ and $|\downarrow\rangle$, because even at 5 Kelvin and 6 Tesla the thermal energy, kT, is about 430 μeV which is greater than the electron Zeeman splitting, $\hbar\Delta_e$, of about 160 μeV. Therefore it is necessary to actively initialize the dot to start in a pure state. Initialization of the qubit is also one of DiVincenzo's requirements for quantum computing [2].

In 2007, Xiaodong Xu et al. demonstrated a fast initialization method using optical pumping [4]. Optical pumping was discussed in Chapter 2, but we revisit the topic here in the context of initialization. We initialize the spin by tuning a CW beam to be on resonance between levels $|2\rangle$ and $|3\rangle$ (as shown in Figure 3.1). The laser drives population from state $|2\rangle$ to state $|3\rangle$ at a rate of the CW Rabi frequency, Ω_{CW}, the excited state $|3\rangle$ decays radiatively at rate $\frac{\Gamma_t}{2}$ to states $|1\rangle$ and $|2\rangle$, and states $|1\rangle$ and $|2\rangle$ interchange population at the spin-flip rate Γ_e.

In InAs self-assembled dots at the proper bias voltage, $\Gamma_e << \Gamma_t$, so after a long enough time the system will be in state $|1\rangle$ with nearly unity probability. If $\Omega_{CW} >> \Gamma_t$ then the system will be initialized in a few radiative lifetimes, which corresponds to a few nanoseconds for our dots [4,5]. When this initialization method is combined with manipulation by a pulsed laser with a 13 ns repetition period, the dot is reinitialized between each set of pulses, forming a series of independent experiments.

We began all our rotations by initializing to state $|1\rangle$ via optical pumping.

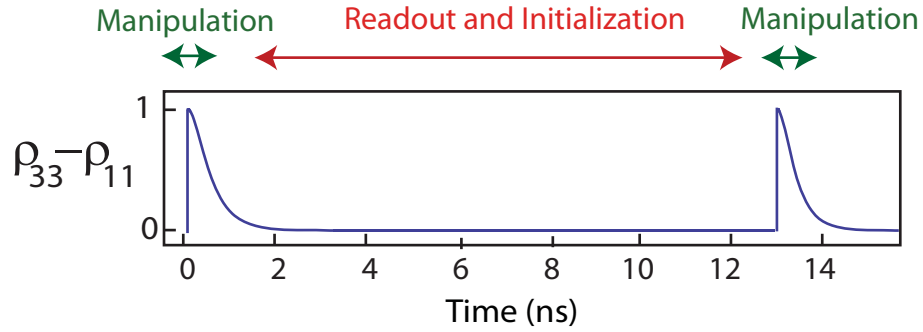

Figure 3.2: Diagram of the experimental dynamics of initialization, pulsed spin manipulation, and readout. The diagram is for the example of an H polarized pulse pulse with π pulse area which excites to state $|3\rangle$. Every 13 ns a pulse excites the dot to state $|3\rangle$, creating a readout signal. Between pulses, optical pumping reinitializes the dot to state $|1\rangle$.

3.3 CW Readout

Since we use the CW beam for initialization, it is convenient to leave it on and use it for readout. The measured signal is the absorption of the CW beam as detected by an avalanche photodiode (APD). As mentioned in Section 2.5.2, phase sensitive detection is used to improve signal to noise by using Stark shift modulation and a lock-in amplifier. The idea, shown in Figure 3.2, is that the CW beam initializes the system, a set of pulses arrive at the sample and manipulate the system, and finally a time averaged absorption signal is detected while optical pumping returns the system to its initialized state. The goal of this section is to relate the measured absorption signal to the state of the dot after the final pulse.

The APD is a square law detector that will detect the light intensity, L. The Maxwell-Bloch equations do not hold in general for a single quantum dot since the plane wave limit is inappropriate. The light intensity, L, at the APD can be properly calculated through the source-field formalism [6]. If $\mathbf{E}_-(t)(\mathbf{E}_+(t))$ are the negative (positive) frequency components of the electric field incident on the detector, then the detector sees an intensity, L, given by

$$L(t) =< \mathbf{E}_-(t)\mathbf{E}_+(t) > . \tag{3.1}$$

Any pulses are, at least ideally, blocked out by a polarizer or other method such that they are not detected by the APD; therefore $\mathbf{E}_+(t)$ is a sum of the CW laser field ($\mathbf{E}_{CW}$) and the optical field radiated by the dot ($\mathbf{E}_S$).

$$\mathbf{E}_+(t) = \mathbf{E}_{CW,+}(t) + \mathbf{E}_{s,+}(t). \tag{3.2}$$

Recall that the CW beam is on resonance with the V1 transition, defined in Figure 2.8, which couples states $|2\rangle$ and $|3\rangle$, such that

$$\mathbf{E}_{CW} = \hat{\mathbf{y}} E_{CW} \cos\omega_{32} t \tag{3.3}$$

where $\omega_{32} = \omega_0 - \frac{\Delta_e + \Delta_h}{2}$. The voltage modulation only modulates $\mathbf{E}_s$, so due to the phase sensitive detection only terms involving cross-products between $\mathbf{E}_s$ and $\mathbf{E}_{CW}$ will be detected by the lock-in.

The detector is in the far field, so the emitted field seen by the detector is approximately the field from an oscillating dipole. Thus, at the detector

$$L(t) =< \mathbf{E}_-(t)\mathbf{E}_+(t) >=< A\mu_{23} a^\dagger(0)\tilde{\sigma}_-(t')e^{i\omega_{32}\frac{R}{c}} + adj. + \text{terms not detected by lockin} > \tag{3.4}$$

where

$$\tilde{\sigma}_-(t) = \sigma_-(t)e^{i\omega_{32}t}, \tag{3.5}$$

A is a complex constant and σ_- is the Heisenberg lowering operator for the 32 transition. The retarded time,

$$t' = t - \frac{R}{c} \tag{3.6}$$

is determined by the distance between the dot and the detector, R, and the speed of light. The phase $\omega_{32}\frac{R}{c}$ represents an interference between the incident field and the field scattered by the dot in the forward direction.

Since the initial state of the field is produced by a narrow bandwidth laser, it resembles a coherent state, allowing the approximation

$$A\mu_{23} < a^\dagger(0)\tilde{\sigma}_{32}(t')e^{i\omega_{32}\frac{|R|}{c}} > \approx A\alpha\mu_{23}\rho_{32}(t')e^{i\omega_{32}\frac{|R|}{c}} \tag{3.7}$$

where $A\alpha$ is proportional to $|\mathbf{E}_{CW}|$.

The response time of the APD,τ_{APD}, is on the order of microseconds, so the signal will be an average over all faster timescales. The current from the APD will therefore be

$$I = \frac{|\mathbf{E}_{CW}|}{\tau_{APD}} \int_0^{\tau_{APD}} (K\mu_{23}\tilde{\rho_{32}}(t')e^{i\omega_{32}\frac{R}{c}} + adj.)\,\mathrm{d}t \tag{3.8}$$

where K is a complex proportionality constant and $\rho_{23}(t) = \tilde{\rho}_{23}(t)e^{i\omega_{32}t}$. Since the integration time (milliseconds) is so much longer than the propagation delay (nanoseconds), it is justifiable to neglect the propagation delay.

The coherence ρ_{32} can be found by solving the following density matrix equations for the four level system in the rotating wave approximation, assuming no pure dephasing.

$$\begin{aligned}
\tfrac{d\rho_{23}}{dt} &= -i\Omega_{23}(\rho_{33} - \rho_{22}) + i\omega_{32}\rho_{23} - \tfrac{\Gamma_t}{2}\rho_{23} \\
\tfrac{d\rho_{22}}{dt} &= -i(-\Omega_{32}\rho_{23} + \Omega_{23}\rho_{32}) + \tfrac{\Gamma_t}{2}(\rho_{33} + \rho_{44}) \\
\tfrac{d\rho_{33}}{dt} &= -i(\Omega_{32}\rho_{23} - \Omega_{23}\rho_{32}) - \Gamma_t\rho_{33} \\
\tfrac{d\rho_{44}}{dt} &= -\Gamma_t\rho_{44}
\end{aligned} \tag{3.9}$$

$$\Omega_{23} = \tfrac{-\mu_{23}E_{CW}}{\hbar} \tag{3.10}$$

These equations are simpler than Equation 2.32 because the narrow bandwidth CW beam only couples one transition. Also, we are neglecting Γ_e and Γ_h since they have a minimal effect during the 13 nanosecond pulse repetition period. For this calculation we are only considering evolution of the system after the final pulse, so $\rho(t = 0)$ is the density matrix immediately after the last pulse. The left column of Figure 3.3 shows the occupation probabilities of all four levels given four different initial conditions. The right column plots the imaginary part of ρ_{23}. Notice that there is a contribution to ρ_{23} even when the dot starts in state $|4\rangle$.

An analytical form of the absorption can be found by assuming a weak CW beam and using perturbation theory to solve Equation 3.9. It may be noted that initialization within the 13 ns pulse repetition period requires strong CW beams, so after inspection of the analytical perturbative solution the strong CW beam limit is treated

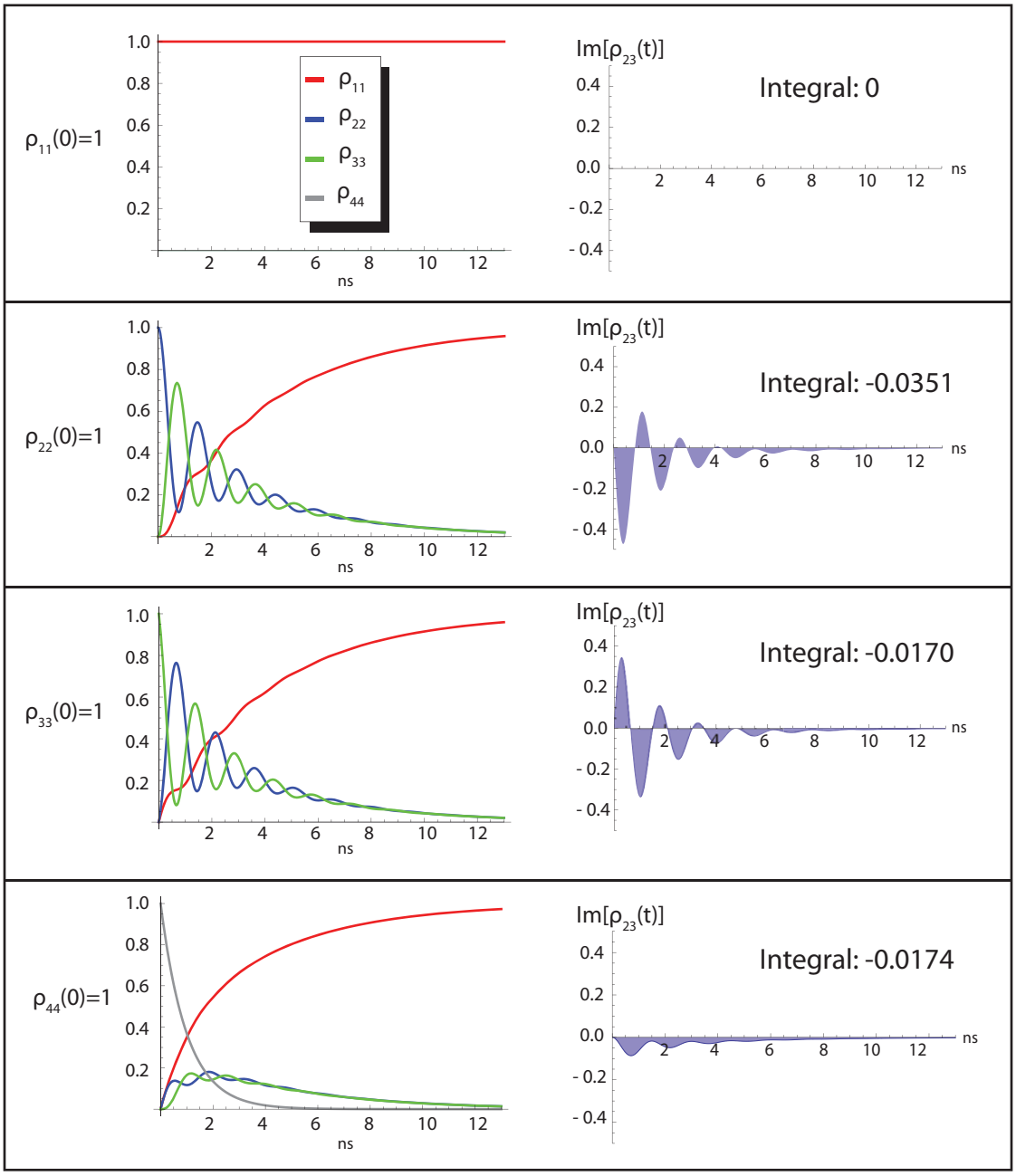

Figure 3.3: Numerical solutions to Equations 3.9 with experimentally relevant values $\Gamma_t = 10^9\ s^{-1}$, and $\Omega_{23} = 4.25 \cdot 10^9\ s^{-1}$. The left column shows the occupation probabilities of all four levels given four different initial conditions. The right column plots the imaginary part of ρ_{23} in the field interaction picture for the same initial conditions. Notice that there is a contribution to ρ_{23} even when the dot starts in state $|4\rangle$. The integral values represent an evaluation of $\frac{1}{T}\int_0^T \mathrm{Im}[\tilde{\rho}_{23}(t)]\,\mathrm{d}t$ and are proportional to the detected current.

numerically. First order perturbation theory gives

$$\rho_{23}(t) = \frac{i\Omega_{23}}{\Gamma_t} e^{i\omega_{32}t}[(3\rho_{33}(0) + \rho_{44}(0))e^{-\Gamma_t t} - (4\rho_{33}(0) + 2\rho_{44}(0) + 2\rho_{22}(0))e^{-\frac{\Gamma_t t}{2}} + (\rho_{33}(0) + \rho_{44}(0) + 2\rho_{22}(0))] + \rho_{23}(0)e^{i\omega_{32}t}e^{-\frac{\Gamma_t t}{2}}. \tag{3.11}$$

In this calculation, the effects of decay were included exactly, and only the optical field was treated perturbatively.

To calculate an expression for the APD current, this result is substituted into Equation 3.8. Neglecting terms that oscillate at ω_{32} or $(\omega_{32})^2$, since they would average to zero after the integration, gives

$$I = \frac{E_{CW}}{T} \mathrm{Im}[K e^{i\omega_{32}\frac{R}{c}} \mu_{32} \int_0^T \tilde{\rho}_{23}(t)\, \mathrm{d}t] \tag{3.12}$$

where $\rho_{23}(t) = \tilde{\rho}_{23}(t)e^{i\omega_{32}t}$. Integration is over T, the repetition period of our pulsed laser, because ideally the dot dynamics repeat every repetition period. The measurement is actually an average over τ_{APD}, which consists of many repetition periods. Evaluating the integral gives

$$\begin{aligned} I = \frac{(E_{CW})^2|\mu_{23}|^2}{\hbar\Gamma_t T} \mathrm{Im}[iKe^{i\omega_{32}\frac{R}{c}}][\rho_{33}(0)(&\frac{-3}{\Gamma_t}e^{-\Gamma_t T} + \frac{8}{\Gamma_t}e^{\frac{-\Gamma_t T}{2}} - \frac{5}{\Gamma_t} + T) \\ &+\rho_{44}(0)(\frac{-1}{\Gamma_t}e^{-\Gamma_t T} + \frac{4}{\Gamma_t}e^{\frac{-\Gamma_t T}{2}} - \frac{3}{\Gamma_t} + T) \\ &+\rho_{22}(0)(\frac{4}{\Gamma_t}e^{\frac{-\Gamma_t T}{2}} - \frac{4}{\Gamma_t} + 2T)] \\ -\frac{2E_{CW}}{\Gamma_t T} Im[Ke^{i\omega_{32}\frac{R}{c}}&\mu_{32}\rho_{23}(0)](e^{\frac{-\Gamma_t T}{2}} - 1). \end{aligned} \tag{3.13}$$

First order perturbation theory is a valid approximation if 1) $\Omega_{23} \ll \Gamma_t$ and 2) $T \ll \frac{\Gamma_t}{|\Omega_{23}|^2}$. The second condition ensures that no significant optical pumping occurs during the timescales of interest. $\Gamma_t = 10^9 s^{-1}$ for the dot used in these studies and T=13 ns for the pulsed Ti-Saph laser, which fulfills the second condition as long as the first condition is satisfied. Plugging in these values for Γ_t and T gives

$$I \approx \frac{2(E_{CW})^2|\mu_{23}|^2}{13\hbar}[4\rho_{33}(0)+5\rho_{44}(0)+11\rho_{22}(0)] - \frac{2E_{CW}}{\Gamma_t T} Im[Ke^{i\omega_{32}\frac{R}{c}}\mu_{32}\rho_{23}(0)] \tag{3.14}$$

This gives the relative contributions of the various density matrix terms, as present immediately after the pulses, to the time integrated readout signal. These relative

contributions are confirmed by a numerical solution of the density matrix equations (3.9) using the values of Γ_t and T from above and with $\Omega_{23} << \Gamma_t$. With field amplitudes that are more typical of our experiments, for example that allow initialization via optical pumping within a few nanoseconds, the different density matrix elements contribute in somewhat different ratios. Numerical simulations show that the measured signal in an experimentally typical regime is roughly proportional to

$$[\frac{1}{2}\rho_{33}(0) + \frac{1}{2}\rho_{44}(0) + \rho_{22}(0)] \equiv A_{CW} \tag{3.15}$$

There are some limitations to this readout method. Explicit in Equation 3.15 is the limitation that multiple density matrix values could give the same CW absorption signal. For example, $\rho_{33}(0) = \rho_{44}(0) = .5$ would give the same signal as $\rho_{22}(0) = \rho_{11}(0) = .5$. The ambiguity is reduced if time dynamics are monitored by using multiple pulses with variable delays. At first it appears that we cannot measure coherences with this method, but in fact we can. Details will be discussed in Chapter 4, but the idea is that a final pulse can convert a coherence into a population in order to detect it by CW absorption. This is very analogous to how coherences are read out with pulsed absorption measurements [7].

Another limitation is that if too much power from the pulses leaks through to the detector, then the noise can overwhelm the CW absorption signal. The simplest solutions to this limitation are to spatially block the pulses or to make the pulses cross polarized with the CW beam so they can be blocked by a polarizer. The polarization method also requires that the beams are well polarized after propagating through the sample and optics. Unfortunately, the apertures on our sample diffract the beams such that we cannot block the pulses spatially, so we primarily rely on polarization. In Appendix C we will discuss a possible additional solution for blocking the pulses, such that we can use any polarization of pulses with CW readout.

The final major limitation is that by leaving the CW beam on during the pulse manipulations the CW beam will affect the states of the system. Unless the CW beam is extremely strong, this effect will be small on the timescale of a fast gate, but it would still reduce the fidelity of an operation. The effect of the CW beam will be

discussed further in Section 3.7. The CW beam also reinitializes the system within a few nanoseconds, so this experimental method is not appropriate if it is necessary for the quantum system to hold information for longer times. In our case, we have already made our measurement and desire that the dot be reinitialized for the next measurement.

We decided to use CW readout, despite these limitations, for three reasons. First, the CW readout method was originally developed out of necessity for the spin rotation experiment described in Section 3.5, which uses detuned pulses. It would be extremely difficult to detect the weak absorption of the detuned pulses compared to detecting the absorption of an on resonant CW beam. Second, we want to use the CW beam for initialization, so this is a short term approach until the optical system is modified to allow gating of the CW beam. Third, the signal to noise acquired in a given amount of time is better compared to detecting the absorption of pulses [5]. This is partially because the pulsed method is sensitive to a power dependent background, requiring twice as many points to be acquired such that we can perform background subtraction [5].

3.4 Optical Excitation of a Two-level System

Now that we have established an initialization and experimental readout method, we return to our goal of rotating the electron spin. At first it seems that this is a fairly simple problem of transferring population between two quantum levels. Let us begin by considering the canonical problem of the interaction of an electromagnetic wave with a two-level quantum system, as this is the basis for later developments. For now we will leave the form of the interaction general so that it could represent an electric or magnetic interaction. Since our goal is the development of gates, it is most appropriate to focus on pulsed manipulations. We will define the perturbation as a square pulse, as this is easiest to solve analytically. Solutions for hyperbolic secant pulses are also analytically achievable and are addressed in detail in a text recently published by Paul Berman [6]. For this body of work the exact form of the solution

during the pulse is not critical, so the square pulse approximation is suitable to find the state of the quantum system after the pulse. Much of the following notation and development follows Chapter 2 of the text by Berman [6].

If the pulses have a pulsewidth of τ and frequency ω then the general field interaction can be defined as

$$\mathbf{V}(t) = \mathbf{V_0}\cos(\omega t + \phi) \sqcap (\frac{t}{\tau}) \tag{3.16}$$

$$\sqcap(\frac{t}{\tau}) = \begin{cases} 1 & \text{if } 0 \leq t < \tau \\ 0 & \text{if } t < 0 \text{ or } t \geq \tau. \end{cases} \tag{3.17}$$

The Hamiltonian can be written as the Hamiltonian in the absence of the field, $\mathbf{H_0}$, plus the interaction Hamiltonian, $\mathbf{V}$. The two levels have an energy difference $\hbar\omega_0$, and the zero energy level is chosen to be halfway between the two levels.

$$\mathbf{H} = \mathbf{H_0} + \mathbf{V} = \frac{\hbar\omega_0}{2}\begin{bmatrix} -1 & 0 \\ 0 & 1 \end{bmatrix} + \begin{bmatrix} 0 & \mathbf{V}(t) \\ \mathbf{V}(t) & 0 \end{bmatrix} \tag{3.18}$$

If $a_g(t)$ and $a_e(t)$ are the probability amplitudes for the ground and excited state respectively, then

$$\begin{aligned} i\hbar\dot{a}_g(t) &= -\tfrac{\hbar\omega_0}{2}a_g(t) + \mathbf{V}(t)a_e(t) \\ i\hbar\dot{a}_e(t) &= \tfrac{\hbar\omega_0}{2}a_e(t) + \mathbf{V}(t)a_g(t). \end{aligned} \tag{3.19}$$

The probability amplitudes in the field interaction representation are defined by the transformations

$$\begin{aligned} a_g(t) &= e^{i\omega t/2}c_g(t) \\ a_e(t) &= e^{-i\omega t/2}c_e(t), \end{aligned} \tag{3.20}$$

which when substituted into equation 3.19 give

$$\begin{aligned} i\hbar\dot{c}_g(t) &= -\tfrac{\hbar\delta}{2}c_g(t) + \mathbf{V}(t)e^{-i\omega t}c_e(t) \\ i\hbar\dot{c}_e(t) &= \tfrac{\hbar\delta}{2}c_e(t) + \mathbf{V}(t)e^{i\omega t}c_g(t) \end{aligned} \tag{3.21}$$

where $\delta = \omega_0 - \omega$. If we take the rotating wave approximation, which says that terms that oscillate at 2ω average to zero for relevant time scales, then for times $0 \leq t < \tau$ these equations simplify to

$$\begin{aligned} i\hbar\dot{c}_g(t) &= -\tfrac{\hbar\delta}{2}c_g(t) + \mathbf{V_0}e^{i\phi}c_e(t) \\ i\hbar\dot{c}_e(t) &= \tfrac{\hbar\delta}{2}c_e(t) + \mathbf{V_0}e^{-i\phi}c_g(t). \end{aligned} \tag{3.22}$$

If we define $\Omega_0 = -\frac{\mathbf{V_0}e^{i\phi}}{\hbar}$, then we can write

$$\begin{aligned}\dot{c}_g(t) &= i\tfrac{\delta}{2}c_g(t) + i\tfrac{\Omega_0}{2}c_e(t)\\ \dot{c}_e(t) &= -i\tfrac{\delta}{2}c_e(t) + i\tfrac{\Omega_0^*}{2}c_g(t).\end{aligned} \tag{3.23}$$

This coupled pair of differential equations can be solved since Ω_0 is independent of time. We find that for $0 \le t < \tau$

$$\begin{bmatrix} c_g(t) \\ c_e(t) \end{bmatrix} = \begin{bmatrix} \cos(\frac{\Omega t}{2}) + \frac{i\delta}{\Omega}\sin(\frac{\Omega t}{2}) & -\frac{i\Omega_0^*}{\Omega}\sin(\frac{\Omega t}{2}) \\ -\frac{i\Omega_0}{\Omega}\sin(\frac{\Omega t}{2}) & \cos(\frac{\Omega t}{2}) - \frac{i\delta}{\Omega}\sin(\frac{\Omega t}{2}) \end{bmatrix} \begin{bmatrix} c_g(0) \\ c_e(0) \end{bmatrix}. \tag{3.24}$$

.

$$\Omega = \sqrt{\delta^2 + |\Omega_0|^2} \tag{3.25}$$

From this we can find the state of the system immediately after the pulse by substituting τ for t in Equation 3.24. Equivalently, if $\mathbf{v}(t) = \begin{bmatrix} c_g(t) \\ c_e(t) \end{bmatrix}$ then

$$\mathbf{v}(t) = e^{\frac{-i\Omega t}{2}\mathbf{n}\cdot\boldsymbol{\sigma'}}\mathbf{v}(0) \tag{3.26}$$

where

$$\sigma_u = \begin{pmatrix} 0 & 1 \\ 1 & 0 \end{pmatrix} \quad \sigma_v = \begin{pmatrix} 0 & -i \\ i & 0 \end{pmatrix} \quad \sigma_w = \begin{pmatrix} 1 & 0 \\ 0 & -1 \end{pmatrix} \tag{3.27}$$

$$\mathbf{n} = \frac{\mathrm{Re}[\Omega_0]}{\Omega}\hat{\mathbf{u}} + \frac{\mathrm{Im}[\Omega_0]}{\Omega}\hat{\mathbf{v}} - \frac{\delta}{\Omega}\hat{\mathbf{w}}. \tag{3.28}$$

$U_R(\Phi) = e^{\frac{-i\Phi}{2}\hat{\mathbf{n}}\cdot\boldsymbol{\sigma'}}$ is a representation of the SU(2) group, which describes rotation of a two state system about the axis $\mathbf{n}$ by an angle Φ [6]. By writing the effect of the perturbation in the form of the SU(2) group, we have shown that such a perturbation can lead to a rotation of the state vector.

In this manner we could directly drive the spin between the $|x+\rangle$ and $|x-\rangle$ states with a magnetic pulse tuned to the energy difference $\hbar\Delta_e$ [8]. However, this direct transition is of a microwave frequency. Our model for electromagnetic interactions is only appropriate for Rabi frequencies, Ω, much less than the transition frequency. This limits the microwave pulsewidth to the order of nanoseconds. It is essential for quantum computation that gates operate much faster than the dephasing time, which is 80 ns for InAs dots, even when actively reducing nuclear fluctuations [2, 9].

Even with the microsecond dephasing times measured by Clark [10], it would not be possible to perform the 10^6 gate operations necessary to perform error correction [11]. Clearly microwave transitions will not suffice, so we focus on optical methods.

The allowed optical transitions were presented in Chapter 2. A simple optical approach would be to first excite the electron to, for example, $|T_x+\rangle$ with a pulse and then to drive it back down to $|x+\rangle$ with a second pulse. This method would be prone to errors, since for the time between the pulses the electron is in an excited state. The trion states decay quickly, and any decay would add error to the process. Thus, it is preferable to keep the electron in the ground state whenever possible. The following section derives a method for rotating the spin in which the electron is only in an excited state for the brief duration of each pulse.

3.5 Rotation about the optical axis via Raman transitions

To develop our ground state rotation we must first extend the theoretical development from Section 3.4 to optical excitation of a four level system. The general equations for this were developed in Chapter 2. We will again define the electric field as

$$\mathbf{E}(t) = \frac{1}{2}(E_x(t)\hat{x} + E_y(t)\hat{y})e^{-i\omega t} + \frac{1}{2}(E_x^*(t)\hat{x} + E_y^*(t)\hat{y})e^{i\omega t}. \tag{3.29}$$

We use the Hamiltonian from Equation 2.28, which was written in the field interaction representation and the rotating wave approximation. The optical interaction was calculated in the dipole approximation, $\mathbf{V} = -\boldsymbol{\mu}\cdot\mathbf{E}$. As a reminder, the equations of motion for the probability amplitudes are

$$\begin{aligned}
\dot{c}_1(t) &= \tfrac{i}{2}[(\delta+\Delta_e)c_1(t) - \Omega_x^*(t)c_3(t) - \Omega_y^*(t)c_4(t)] \\
\dot{c}_2(t) &= \tfrac{i}{2}[(\delta-\Delta_e)c_2(t) - \Omega_y^*(t)c_3(t) - \Omega_x^*(t)c_4(t)] \\
\dot{c}_3(t) &= \tfrac{i}{2}[-\Omega_x(t)c_1(t) - \Omega_y(t)c_2(t) + (-\delta+\Delta_h)c_3(t)] \\
\dot{c}_4(t) &= \tfrac{i}{2}[-\Omega_y(t)c_1(t) - \Omega_x(t)c_2(t) + (-\delta-\Delta_h)c_4(t)]
\end{aligned} \tag{3.30}$$

where

$$\Omega_x(t) \equiv \tfrac{\wp E_x(t)}{\hbar\sqrt{2}} \quad \Omega_y(t) \equiv \tfrac{i\wp E_y(t)}{\hbar\sqrt{2}}. \tag{3.31}$$

To simplify these equations, it is useful to make the substitutions

$$\begin{aligned}\tilde{c}_3(t) &= c_3(t)e^{-\frac{i}{2}(-\delta+\Delta_h)t} \\ \tilde{c}_4(t) &= c_4(t)e^{\frac{i}{2}(\delta+\Delta_h)t},\end{aligned} \tag{3.32}$$

which gives

$$\begin{aligned}\dot{\tilde{c}}_3(t) &= \tfrac{i}{2}e^{-\frac{i}{2}(-\delta+\Delta_h)t}[-\Omega_x(t)c_1(t) - \Omega_y(t)c_2(t)] \\ \dot{\tilde{c}}_4(t) &= \tfrac{i}{2}e^{\frac{i}{2}(\delta+\Delta_h)t}[-\Omega_y(t)c_1(t) - \Omega_x(t)c_2(t)].\end{aligned} \tag{3.33}$$

Integrating Equation 3.33 by parts gives

$$\begin{aligned}\tilde{c}_3(t) &= \tfrac{1}{-\delta+\Delta_h}[(\Omega_x c_1 + \Omega_y c_2)e^{-\frac{i}{2}(-\delta+\Delta_h)t} - \textstyle\int e^{-\frac{i}{2}(-\delta+\Delta_h)t}\frac{\mathrm{d}}{\mathrm{d}\,t}(\Omega_x c_1 + \Omega_y c_2)\mathrm{d}t] \\ \tilde{c}_4(t) &= \tfrac{-1}{\delta+\Delta_h}[(\Omega_y c_1 + \Omega_x c_2)e^{\frac{i}{2}(\delta+\Delta_h)t} + \textstyle\int e^{\frac{i}{2}(\delta+\Delta_h)t}\frac{\mathrm{d}}{\mathrm{d}\,t}(\Omega_y c_1 + \Omega_x c_2)\mathrm{d}t],\end{aligned} \tag{3.34}$$

where the time dependence of the Rabi frequencies and probability amplitudes has been dropped for compactness.

In the limit that all of the following are true

$$\begin{aligned}|\tfrac{\mathrm{d}}{\mathrm{d}\,t}(\tfrac{\Omega_x c_1}{\delta-\Delta_h})| &<< |\Omega_x c_1| \\ |\tfrac{\mathrm{d}}{\mathrm{d}\,t}(\tfrac{\Omega_y c_2}{\delta-\Delta_h})| &<< |\Omega_y c_2| \\ |\tfrac{\mathrm{d}}{\mathrm{d}\,t}(\tfrac{\Omega_x c_2}{\delta+\Delta_h})| &<< |\Omega_x c_2| \\ |\tfrac{\mathrm{d}}{\mathrm{d}\,t}(\tfrac{\Omega_y c_1}{\delta+\Delta_h})| &<< |\Omega_y c_1|,\end{aligned} \tag{3.35}$$

the integral portion of Equation 3.34 is small and can be neglected in the lowest order solution.

$$\begin{aligned}\tilde{c}_3(t) &\approx \tfrac{1}{-\delta+\Delta_h}(\Omega_x c_1 + \Omega_y c_2)e^{-\frac{i}{2}(-\delta+\Delta_h)t} \\ \tilde{c}_4(t) &\approx \tfrac{-1}{\delta+\Delta_h}(\Omega_y c_1 + \Omega_x c_2)e^{\frac{i}{2}(\delta+\Delta_h)t}\end{aligned} \tag{3.36}$$

Substituting these approximate solutions into Equation 3.30 gives

$$\begin{aligned}\dot{c}_1 &\approx \tfrac{i}{2}[(\delta+\Delta_e)c_1 + \tfrac{|\Omega_x|^2 c_1 + \Omega_x^*\Omega_y c_2}{\delta-\Delta_h} + \tfrac{|\Omega_y|^2 c_1 + \Omega_y^*\Omega_x c_2}{\delta+\Delta_h}] \\ \dot{c}_2 &\approx \tfrac{i}{2}[(\delta-\Delta_e)c_1 + \tfrac{|\Omega_y|^2 c_2 + \Omega_y^*\Omega_x c_1}{\delta-\Delta_h} + \tfrac{|\Omega_x|^2 c_2 + \Omega_x^*\Omega_y c_1}{\delta+\Delta_h}],\end{aligned} \tag{3.37}$$

which is equivalent to an effective two level Hamiltonian:

$$H_{eff} = \frac{-\hbar}{2}\begin{bmatrix}\delta+\Delta_e+\frac{|\Omega_x|^2}{\delta-\Delta_h}+\frac{|\Omega_y|^2}{\delta+\Delta_h} & \frac{\Omega_x^*\Omega_y}{\delta-\Delta_h}+\frac{\Omega_y^*\Omega_x}{\delta+\Delta_h} \\ \frac{\Omega_x\Omega_y^*}{\delta-\Delta_h}+\frac{\Omega_y\Omega_x^*}{\delta+\Delta_h} & \delta-\Delta_e+\frac{|\Omega_x|^2}{\delta+\Delta_h}+\frac{|\Omega_y|^2}{\delta-\Delta_h}\end{bmatrix}. \tag{3.38}$$

This procedure is known as adiabatically eliminating the trion states [6]. If the detuning is large enough, then further approximations can be made. If $\delta >> \Delta_h, \Delta_e$

then to first order in $\frac{\Delta_h}{\delta}$

$$H_{eff} \approx \frac{-\hbar}{2}\begin{bmatrix} \delta + \Delta_e + \frac{|\Omega_x|^2+|\Omega_y|^2}{\delta} + \frac{(-|\Omega_x|^2+|\Omega_y|^2)\Delta_h}{\delta^2} & \frac{\Omega_x^*\Omega_y+\Omega_y^*\Omega_x}{\delta} + \frac{(\Omega_y^*\Omega_x-\Omega_x^*\Omega_y)\Delta_h}{\delta^2} \\ \frac{\Omega_x^*\Omega_y+\Omega_y^*\Omega_x}{\delta} + \frac{(-\Omega_y^*\Omega_x+\Omega_x^*\Omega_y)\Delta_h}{\delta^2} & \delta - \Delta_e + \frac{|\Omega_x|^2+|\Omega_y|^2}{\delta} + \frac{(|\Omega_x|^2-|\Omega_y|^2)\Delta_h}{\delta^2} \end{bmatrix}. \tag{3.39}$$

Thus, if the pulses are detuned enough compared to the rate of change of the electric fields, the trion levels can be neglected. The interaction reduces to a two level system where the ground state energies have been shifted by a light shift. Now that we have cranked through the math, remember that we are trying to rotate the electron spin. As mentioned, the goal is to not excite occupation of the trion levels, so detuning from the trion transitions is somewhat intuitive. It is the off-diagonal terms of the two level effective Hamiltonian that allow our spin flip, since the levels of our two level system are the electron spin states. The physical process by which the spin flips is a coherent Raman interaction via a virtual intermediate state.

We want to maximize the off-diagonal terms in this effective Hamiltonian, since they are the terms creating the spin rotation. This means maximizing $|\Omega_x^*\Omega_y + \Omega_y^*\Omega_x|$. If we assume that the x and y components have equal power such that we can write $E_y = E_x e^{i\phi}$, then $|\Omega_x^*\Omega_y + \Omega_y^*\Omega_x| = 2|\Omega_x|^2 \sin\phi$. This shows that $\phi = \pm\frac{\pi}{2}$, circular polarization, leads to the maximum coupling between the spin states. Also $\phi = 0$, 45 degree polarization, makes the leading term zero and leaves a coupling that is weaker by the factor $\frac{\Delta_h}{\delta}$. We can understand this better by first realizing that this phase dependence is not present in a three level lambda system. Physically, the phase dependence is present because there are two possible two-photon pathways (V1-H2 and V2-H1). This phase dependence is a result of interference of the two pathways.

To see that this interaction takes the form of a rotation of the spin, we must make a few more approximations. First, we neglect terms proportional to $\frac{\Delta_h}{\delta}$. Second, we shift our zero energy by $\frac{\hbar\delta}{2}$ (which is equivalent to pulling out a phase factor common to all states) and finally we ignore the light shifts $\frac{|\Omega_x|^2+|\Omega_y|^2}{\delta}$. This leaves us with

$$H_{eff} \approx \frac{-\hbar}{2}\begin{bmatrix} \Delta_e & \tilde{V}(t) \\ \tilde{V}(t) & -\Delta_e \end{bmatrix} \tag{3.40}$$

where $\tilde{V}(t) = \frac{\Omega_x^* \Omega_y + \Omega_y^* \Omega_x}{\delta}$. Now we can make use of the Bloch vector picture. Discussions of this formalism can be found in most quantum optics books [6, 12]. In this formalism two vectors are defined, the Bloch vector $\mathbf{B}$ and the pseudofield vector $\mathbf{\Omega}_{pseudo}(t)$. For our H_{eff},

$$\mathbf{B}(t) = \begin{bmatrix} u \\ v \\ w \end{bmatrix} = \begin{bmatrix} \tilde{\rho}_{12} + \tilde{\rho}_{21} \\ i(\tilde{\rho}_{21} - \tilde{\rho}_{12}) \\ \rho_{22} - \rho_{11} \end{bmatrix} \tag{3.41}$$

$$\mathbf{\Omega}_{pseudo}(t) = \begin{bmatrix} -\tilde{V}(t) \\ 0 \\ \Delta_e \end{bmatrix} \tag{3.42}$$

Recall the experimental geometry presented in Figure 2.7. Given that a positive quantity $\rho_{22} - \rho_{11}$ corresponds to the spin aligned in the $+\hat{x}$ direction, the Bloch vector corresponds to the spin's direction in real space directions as follows:

$$\hat{w} \to \hat{x} \quad \hat{v} \to \hat{y} \quad \hat{u} \to -\hat{z} \tag{3.43}$$

The dynamics of the system can be visualized by the Bloch vector precessing about the pseudofield vector.

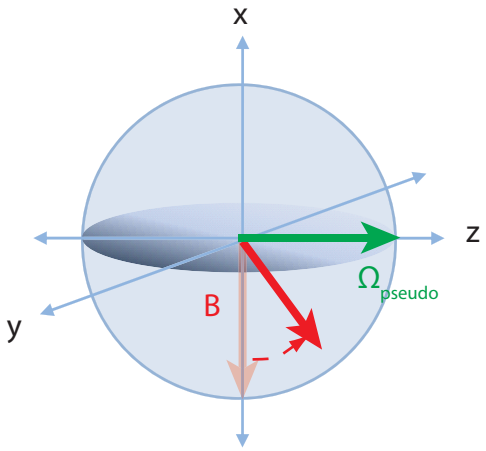

Figure 3.4: A Bloch sphere picture of the rotation described by Equation 3.40. The Bloch vector, $\mathbf{B}$, precesses about the pseudofield vector, $\mathbf{\Omega}_{pseudo}$. For the spin qubit system, the Bloch vector corresponds to the spin vector representation in real space.

The magnitude of $\tilde{V}$ is much greater than Δ_e for typical experimental parameters, so during the pulse the dominant effect is a rotation of the spin about the z axis, as shown in Figure 3.4. (We will discuss the effect of Δ_e in the absence of the pulse in the next section.) Neglecting the effect of the Zeeman splitting also leads to the following solution for the probability amplitudes immediately following a pulse:

$$\begin{aligned} c_1(t) &= \cos\tfrac{\theta}{2} c_1(-) + i \sin\tfrac{\theta}{2} c_2(-) \\ c_2(t) &= +i \sin\tfrac{\theta}{2} c_1(-) + \cos\tfrac{\theta}{2} c_2(-) \\ \theta &= \textstyle\int_{-\infty}^{\infty} \tilde{V}(t)\,\mathrm{d}t \end{aligned} \tag{3.44}$$

The terms such as $c_1(-)$ represent the probability amplitudes before the pulse arrives. θ is called the pulse area, and in this case determines the angle of the rotation about the z axis. Equation 3.44 is of the same form as Equation 3.24, which is that of a rotation.

Thus we have argued theoretically that a sufficiently detuned circularly polarized pulse should rotate the spin about the z axis by an amount determined by the pulse area. This two-photon optical process keeps the system in the ground states while being faster than a microwave interaction. The speed of the rotation is determined by the pulsewidth, which is in turn limited by the approximation conditions from Equation 3.35. Next we describe the experimental implementation of this rotation method.

3.5.1 Results: Spin Rabi Oscillations

The experimental measurement of Rabi oscillations between the two electron spin states involves two lasers, a CW laser for initialization and readout and a pulsed beam to perform rotations. The experimental layout is shown in Figure 3.5. The direction of the laser propagation and magnetic field are as defined in Figure 2.7. The pulses are produced by a Coherent Mira, which is a Kerr modelocked Ti:Saph laser. The pulses have a hyperbolic secant shape, a pulsewidth of about 2 ps for this measurement, a repetition period of 13 ns and are roughly transform limited. The pulses pass through a traveling wave acousto-optic modulator and the first order

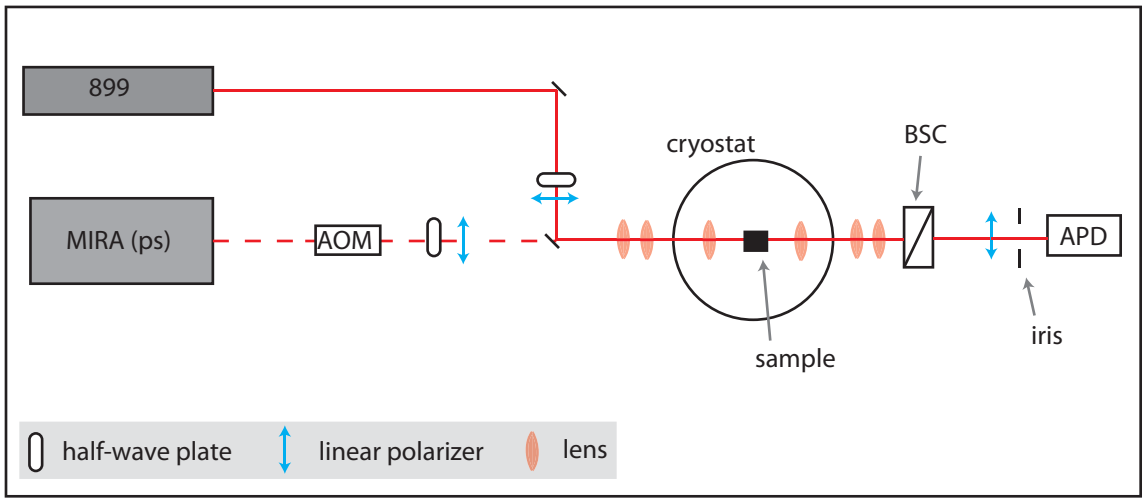

Figure 3.5: The experimental layout used for spin Rabi measurements. The 899 CW Ti:Saph laser is used for initialization and readout. The MIRA modelocked Ti:Saph laser produces picosecond pulses whose power is controlled by an acousto-opic modulator(AOM). The Babinet-Soleil compensator(BSC) and linear polarizer are adjusted such that they block the pulses.

diffracted beam continues to the sample, so that the pulse power at the sample can be electronically controlled by varying the driving amplitude of the modulator. The polarization is either set to be 45 degrees with a linear polarizer or circular with a polarizer and quarterwave plate. The polarization is set immediately before the pulses are combined with the CW beam on a beamsplitter.

The CW beam from the Coherent 899 is tuned to the transition V1 in Figure 2.8, frequency stabilized, and vertically polarized. The lowest energy transition was chosen to avoid any unexpected effects from nonradiative relaxation. As stated in Chapter 2, the 899 has a very narrow (<1MHz) bandwidth so only the V1 transition is coupled. For the on-resonance studies, the Mira is tuned such that the pulse bandwidth is centered on the V1 transition also, however its bandwidth is much greater than the ground state and trion state splitting, so all four transitions are coupled by the pulse. For the detuned measurements, the Mira is tuned 1 meV to the red of the V1 transition.

Both beams are collimated before being combined by a beamsplitter. The two collinear beams are then focused onto the aperture of interest. The transmitted beams pass through a Babinet Soleil compensator and then a linear polarizer. This

combination is adjusted for a given measurement to block the transmitted pulses. The compensator enables adjustment for birefringence in the sample and the cryostat windows that can lead to somewhat elliptically polarized transmitted beams. The remaining transmitted light is spatially filtered with an iris to reduce scattered light and focused onto a silicon avalanche photodiode.

This setup detects the modulated absorption of the CW beam. As described in Chapter 2, the sample is kept at 5 Kelvin and a bias is applied which has a DC and AC component. The DC component is chosen to place the V1 transition in the middle of the optical pumping region and the AC component is .02 V, which is on the order of the transition linewidth. The bias modulation is used as the reference input to a lock-in amplifier which processes the APD signal.

The experiment proceeds as described by Figure 3.2. The CW beam is used to initialize the system to state $|x-\rangle$ as explained in Section 3.2, and the absorption of the CW beam relates to the density matrix through Equation 3.15. From this expression we see that the when the system is in state $|1\rangle$ there is no CW absorption, but if the pulse causes some probability of being in any of the other three states, then CW absorption will be detected.

The data from four different Rabi oscillation experiments is plotted in the right half of Figure 3.6. For each experiment the time averaged CW absorption signal was measured for a range of bias voltages and pulse powers. The objective is to see the probability oscillate as a function of pulse area between the two ground states. This constitutes a spin Rabi oscillation and proves that we can rotate the spin. However, our readout method does not differentiate between the trion states and state $|x+\rangle$. We use polarization and detuning to isolate the two-photon spin Rabi process from the single photon excitation of the trion states.

We know that for 45 degree polarization the two photon process derived in the previous section is very weak, so we expect that signals at this polarization are coming from excitation of the trion levels. This data is shown in the upper half of Figure 3.6. When the pulses are on resonance we see two clear Rabi oscillations that disappear when we detune the pulse by 1 meV (approximately our pulse bandwidth). Thus, if

we use circular polarization and detune by 1 meV we know that any signal is from our coherent two photon spin rotation that does not populate the trion states. This is shown in the bottom right quadrant. The circularly polarized, on resonant data in the lower left quadrant has a combination of one- and two-photon processes.

The left half of Figure 3.6 plots the numerical solutions to the density matrix equations (Equation 2.32) using numerical parameters from the experiment. The calculated signal is Equation 3.15. A pulse power dependent redshift of the V1 transition was phenomenologically added to match an observed effect in the data. It is possible that the pulse is exciting carriers in the wetting layer which are affecting the dot's energy levels.

In summary, the lower right quadrant of Figure 3.6 demonstrates the coherent rotation of the electron spin about the optical (z) axis by an arbitrary angle that is controllable by the pulse power. This rotation is accomplished in 2 picoseconds.

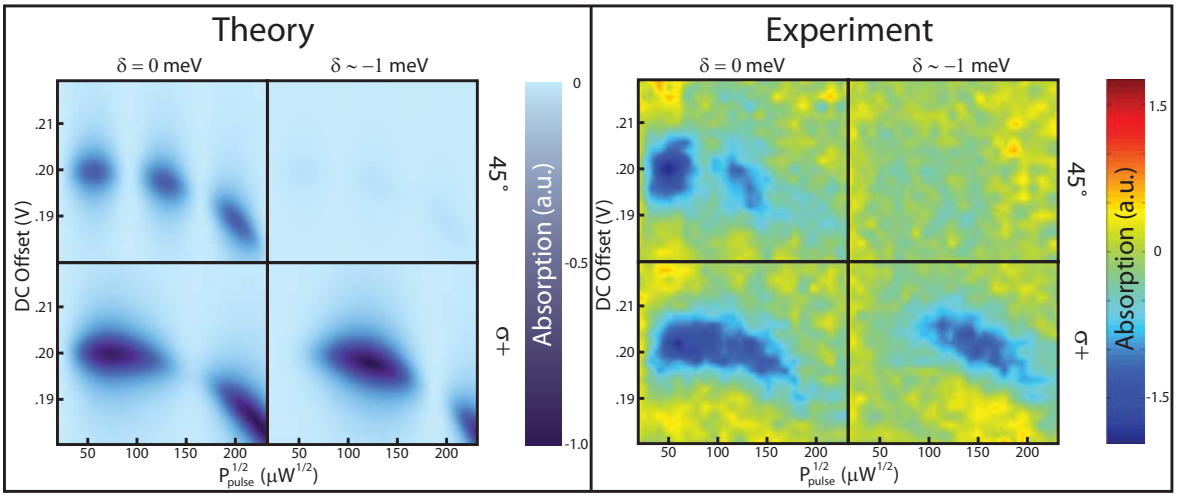

Figure 3.6: Numerical density matrix solutions and experimental data showing spin Rabi oscillations [1]. The plotted signal is the CW beam absorption for varying pulse power and bias voltage. $P_{pulse}^{1/2}$ is the square root of the average power of the pulsed beam and DC offset is the DC component of the sample bias. The two columns compare on-resonant pulses to pulses detuned by 1 meV. The rows contrast 45 and circular polarized pulses.

3.6 Precession

As previously discussed, for an arbitrary rotation we must have the ability to rotate the spin about two orthogonal axes. We have demonstrated a rotation about the z axis. In this section we discuss and measure the Larmour precession of the spin about the magnetic field, which given our axis definitions from Figure 2.7, provides a rotation about the x axis.

In the absence of optical excitation and with a magnetic field applied in the x direction, the probability amplitude equations from Equation 3.30 reduce to

$$\begin{aligned} \dot{c}_1(t) &= \tfrac{i}{2}\Delta_e c_1(t) \\ \dot{c}_2(t) &= -\tfrac{i}{2}\Delta_e c_2(t) \\ \dot{c}_3(t) &= \tfrac{i}{2}\Delta_h c_3(t) \\ \dot{c}_4(t) &= -\tfrac{i}{2}\Delta_h c_4(t) \end{aligned} \tag{3.45}$$

which have the simple solutions

$$\begin{aligned} c_1(t) &= e^{\frac{i\Delta_e t}{2}} c_1(0) \\ c_2(t) &= e^{\frac{-i\Delta_e t}{2}} c_2(0) \\ c_3(t) &= e^{\frac{i\Delta_h t}{2}} c_3(0) \\ c_4(t) &= e^{\frac{-i\Delta_h t}{2}} c_4(0). \end{aligned} \tag{3.46}$$

If there is no population in the trion states, then the two level electron spin system can be represented by equations of the form of Equation 3.26 or by the Bloch vector picture as before, but now

$$\mathbf{\Omega}_{pseudo}(t) = \begin{bmatrix} 0 \\ 0 \\ \Delta_e \end{bmatrix} \tag{3.47}$$

so the electron spin rotates about the x axis.

3.6.1 Results: Ramsey fringes

The experiment to measure this precession is very similar to the Rabi experiment from the previous section, except that there are two pulsed beampaths with a variable delay between them, as shown in Figure 3.7. The two pulses are co-circularly

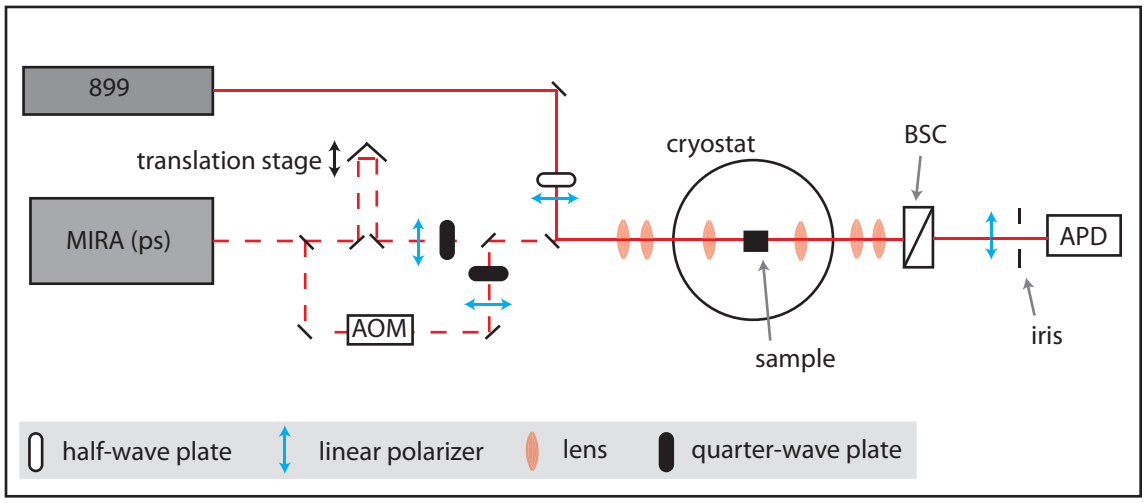

Figure 3.7: Experimental layout for two pulse Ramsey fringe measurements. A computer controlled translation stage scans the delay between the pulses. Otherwise the layout is the same as Figure 3.5.

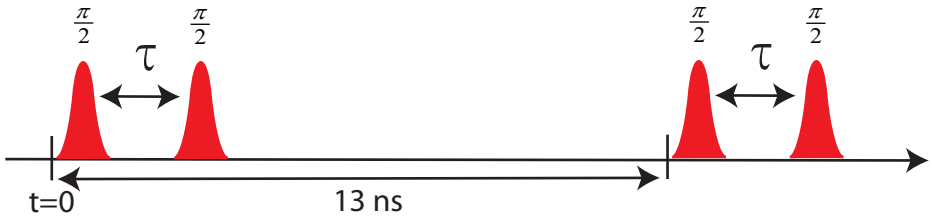

Figure 3.8: Pulse timing diagram for the Ramsey fringe experiments. The difference in pulse path length creates a pair of pulses separated by τ, which can be scanned up to 1 ns. The laser repetition rate is 13 ns.

polarized, detuned such that only the two photon spin rotation is observed, and have pulse areas of $\frac{\pi}{2}$. The timing of the experiment is shown in Figure 3.8.

It is convenient to write the probability amplitude solutions for the effect of the pulses and the effect of the precession in terms of transfer matrices.

$$\mathbf{T}_{pulse}(\theta = \tfrac{\pi}{2}) = \tfrac{\sqrt{2}}{2}\begin{bmatrix} 1 & i \\ i & 1 \end{bmatrix} \quad \mathbf{T}_B = \begin{bmatrix} e^{\frac{i\Delta_e\tau}{2}} & 0 \\ 0 & e^{\frac{-i\Delta_e\tau}{2}} \end{bmatrix} \tag{3.48}$$

The effect of the pulse pair can be found from

$$\mathbf{T}_{pulse}\mathbf{T}_B\mathbf{T}_{pulse} = i\begin{bmatrix} \sin(\frac{\Delta_e\tau}{2}) & \cos(\frac{\Delta_e\tau}{2}) \\ \sin(\frac{\Delta_e\tau}{2}) & -\sin(\frac{\Delta_e\tau}{2}) \end{bmatrix}. \tag{3.49}$$

The CW absorption for a system that starts initialized to state $|1\rangle$ will be proportional

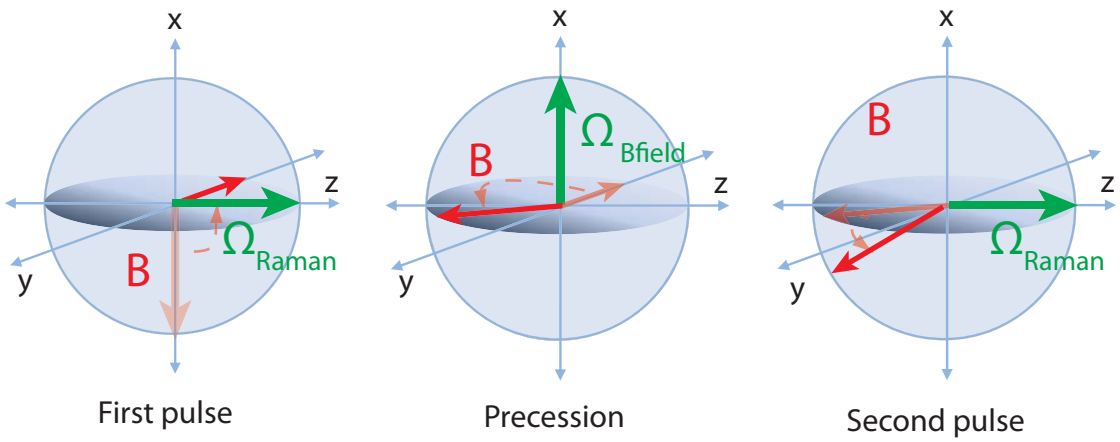

Figure 3.9: A Bloch sphere visualization of the spin dynamics during the two pulse, Ramsey fringe experiment. During the pulses the pseudovector is dominated by the optical field, and thus is approximately along the z (optical) axis, otherwise the pseudovector is along the x axis parallel to the magnetic field. The pulses have pulse area $\frac{\pi}{2}$, so they each rotate the Bloch vector 90 degrees about the pseudovector. Between the pulses the Bloch vector precesses about the pseudovector at a speed determined by the magnetic field strength.

to

$$\rho_{22} = \sin^2(\frac{\Delta_e \tau}{2}). \tag{3.50}$$

The CW beam is on transition V1 as before, so the system starts in state $|1\rangle$ (along the $-x$ axis as shown in Figure 3.9). The first pulse rotates the spin by 90 degrees about the z axis leaving it along the $-y$ axis. For the time τ between the pulses the spin will precess about the x axis until the second pulse rotates the spin again. Thus the delay between the pulses controls the angle of rotation about the x axis. This is a Ramsey fringe type experiment in that it measures the phase of the transition relative to the field for a known period of time.

Figure 3.10 shows the numerical simulation and experimental data for this two pulse measurement as a function of delay between the pulses and magnetic field strength. For a given magnetic field strength, the CW absorption oscillates as a function of delay. The oscillation frequency increases with magnetic field, as expected since $\Delta_e = g_{e,x}\mu_B B_x$. An electron g factor magnitude of 0.4 is extracted from this measurement. The observation of electron spin precession demonstrates that the Raman pulses manipulate the spin in a coherent manner.

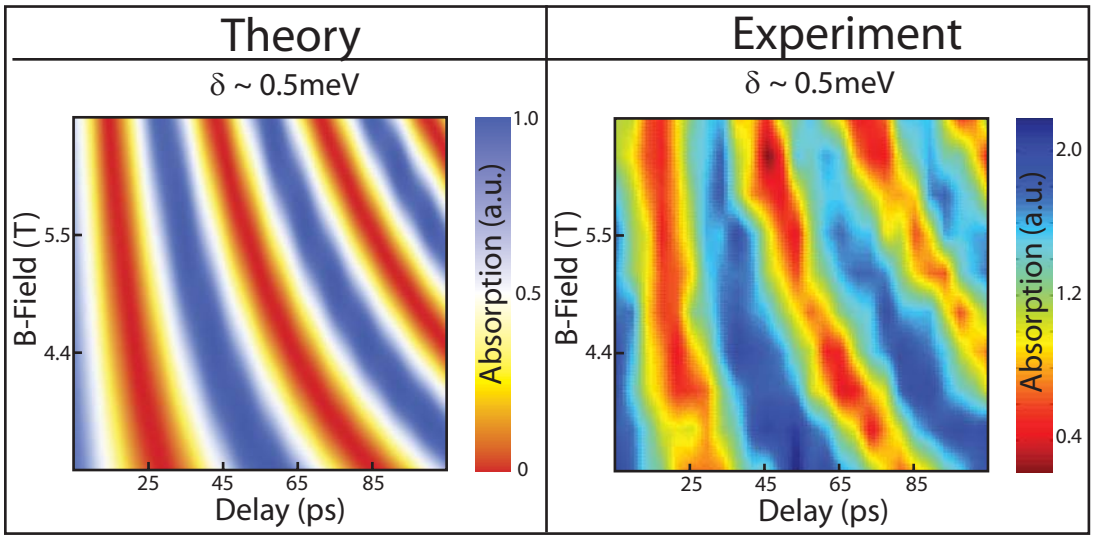

Figure 3.10: Numerical calculations (left) and data (right) for the CW absorption signal in a two pulse Ramsey fringe experiment for varying pulse delay and magnetic field [1]. The pulses are detuned 0.5 meV to the red of the trion transition.

These measurements demonstrate the combination of coherent rotations about two orthogonal axes: one produced by optical pulses, and the other by precession about the magnetic field. All rotations can be executed by any angle. While a rotation of any angle by the optical pulse requires only 2 picoseconds, a rotation of 2π by the magnetic field takes 33 picoseconds in a 6.6 Tesla magnetic field. This is still fast compared to the spin dephasing rate of microseconds. Therefore, we have demonstrated a method for arbitrary rotations of a single spin qubit. The next section discusses a different, purely optical method for optical rotation about the x axis.

3.7 CW Rabi oscillation and geometric phases

In this section we reexamine the derivation and experiment from the Section 3.6 with a focus on the effect of the CW beam between the two pulses. We treat the CW beam as perfectly on resonance with transition V1 such that

$$\begin{aligned} \mathbf{E}_{CW}(t) &= E_{CW}\hat{\mathbf{y}}\cos[(\omega_0 - \tfrac{\Delta_e+\Delta_h}{2})t] \\ \Omega_{CW} &\equiv \tfrac{i\wp E_{CW}(t)}{\hbar\sqrt{2}}. \end{aligned} \tag{3.51}$$

and Equation 3.30 becomes

$$\begin{aligned}
\dot{c}_1(t) &= \tfrac{i(3\Delta_e+\Delta_h)}{4} c_1(t) \\
\dot{c}_2(t) &= \tfrac{i}{4}[(-\Delta_e+\Delta_h)c_2(t) - 2\Omega^*_{CW} c_3(t)] \\
\dot{c}_3(t) &= \tfrac{i}{4}[-2\Omega_{CW} c_2(t) + (-\Delta_e+\Delta_h)c_3(t)] \\
\dot{c}_4(t) &= \tfrac{-i(\Delta_e+3\Delta_h)}{4} c_4(t).
\end{aligned} \tag{3.52}$$

which has the following solutions:

$$\begin{aligned}
c_1(t) &= e^{\frac{i(3\Delta_e+\Delta_h)t}{4}} c_1(0) \\
c_2(t) &= e^{\frac{i(-\Delta_e+\Delta_h)t}{4}} [\cos\tfrac{|\Omega_{CW}|t}{2} c_2(0) - \sin\tfrac{|\Omega_{CW}|t}{2} c_3(0)] \\
c_3(t) &= e^{\frac{i(-\Delta_e+\Delta_h)t}{4}} [\cos\tfrac{|\Omega_{CW}|t}{2} c_3(0) + \sin\tfrac{|\Omega_{CW}|t}{2} c_2(0)] \\
c_4(t) &= e^{\frac{-i(3\Delta_e+\Delta_h)t}{4}} c_4(0)
\end{aligned} \tag{3.53}$$

From these solutions we can extract an effective transfer matrix to describe the effect of simultaneous application of a CW laser and a magnetic field on our spin qubit.

$$\mathbf{T}_{\text{B+CW}} = \begin{bmatrix} e^{\frac{i(3\Delta_e+\Delta_h)t}{4}} & 0 \\ 0 & e^{\frac{i(-\Delta_e+\Delta_h)t}{4}} \cos\tfrac{|\Omega_{CW}|t}{2} \end{bmatrix} \tag{3.54}$$

The exponentials simply represent the precession about the magnetic field discussed in the previous section. If we consider specific values of t such that $t = \frac{2\pi n}{\Omega_{CW}} \equiv T$ then the contribution from the CW beam becomes a factor of $(-1)^n = e^{in\pi}$ between state $|1\rangle$ and $|2\rangle$. Thus the on-resonance CW beam can be used to create rotations of the spin that are multiples of π. This phase shift is considered a geometric phase because it comes from a cyclic transition [13]. In this case the CW beam causes a 2π Rabi oscillation. Such a cyclic evolution can acquire both dynamic and geometric phases. The dynamic phase is a generalization of the standard phase acquired by a wavefunction over time and is defined by

$$\gamma_d = -\frac{i}{\hbar}\int_0^T \frac{\langle\Psi_s(t)|H(t)|\Psi_s(t)\rangle}{\langle\Psi_s(t)|\Psi_s(t)\rangle}\mathrm{d}t \tag{3.55}$$

[13]. In this case, $|\Psi_s(t)\rangle$ is the electron spin vector and the Hamiltonian includes the effects of the magnetic field and the CW beam. If T takes only specific values as defined above and the system starts in one of the spin ground states, then this

integral evaluates to 0 indicating that any phase created is purely geometric. Because the Raman pulses do not lead to occupation of the trion states, experiments involving Raman pulses and complete CW Rabi oscillations can lead to purely geometric phases.

Let us consider the experiment from the previous section where two detuned, circularly polarized $\frac{\pi}{2}$ pulses are separated by a delay τ, but this time we account for the effect of both the magnetic field and the CW beam between the pulses. Since the system starts out initialized to the lowest energy state, the vector for the probability amplitudes of the spin ground states after the two pulse experiment described in the previous section will be

$$\mathbf{T}_{pulse}\mathbf{T}_{BandCW}\mathbf{T}_{pulse}\begin{bmatrix}1\\0\end{bmatrix} = \begin{bmatrix} e^{\frac{i(3\Delta_e+\Delta_h)t}{4}} - e^{\frac{i(-\Delta_e+\Delta_h)\tau}{4}} cos\frac{|\Omega_{CW}|\tau}{2} \\ ie^{\frac{i(3\Delta_e+\Delta_h)t}{4}} + ie^{\frac{i(-\Delta_e+\Delta_h)\tau}{4}} cos\frac{|\Omega_{CW}|\tau}{2}\end{bmatrix}. \tag{3.56}$$

We know that the absorption is proportional to

$$\rho_{22} + \frac{1}{2}(\rho_{33}+\rho_{44}) = \frac{1}{2}(1+\rho_{22}-\rho_{11}) = \frac{1}{2}(1+cos\frac{|\Omega_{CW}|\tau}{2}cos\Delta_e\tau) \tag{3.57}$$

so we expect the data from such a measurement to show oscillations with two frequency components: one from the Zeeman splitting of the ground states and one from Rabi oscillations of the CW beam. In the data shown in Figure 3.10 the CW beam was weak enough that the Rabi oscillations were so slow as to be unnoticeable on the timescale of the pulse delay.

3.7.1 Results: CW Rabi oscillations and π phase shifts

Figure 3.11 shows the same experiment as in Section 3.6.1 repeated with increasingly stronger CW beams and longer delay times so as to observe the effect of the CW beam. The faster oscillation represents the precession about the magnetic field and the slower envelope oscillation is due to the CW beam. Note that the envelope oscillation gets faster with higher CW beam powers, as expected from the theory. Also, the π phase shift mentioned above can be observed by comparing the precession signals at different powers. Near zero delay all powers precess in phase, for example at the first, green dotted line. After a given plot passes through a node of the envelope indicating

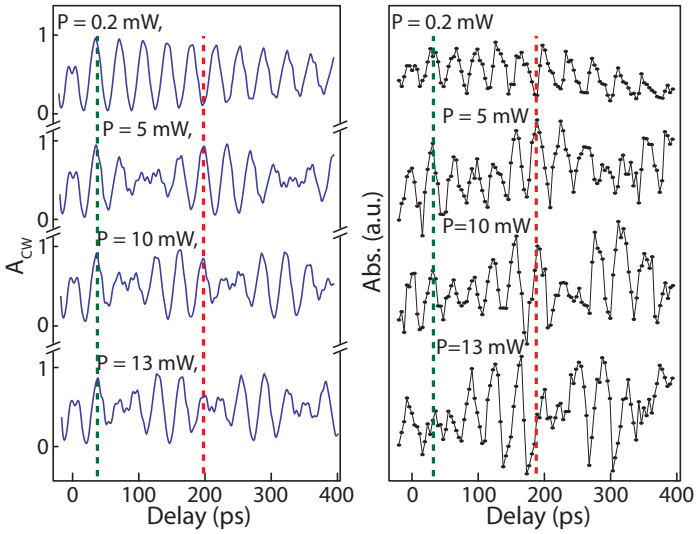

Figure 3.11: Numerical calculations (left) and data (right) showing the geometric phase and modulation envelope produced by the CW beam [1]. The fast oscillation is the spin precession. The four plots correspond to different powers, P, of the CW laser. The green dashed line demonstrates that all four plots are in phase near zero delay, while some plots are out of phase at the red line due to the acquired geometric phase. For the theoretical calculation $A_{CW} = \frac{1}{2}\rho_{33}(0) + \frac{1}{2}\rho_{44}(0) + \rho_{22}(0)$.

that $\tau > \frac{2\pi}{\Omega_{CW}}$, it is out of phase by π compared to a plot that has not passed through a node. For example, compare the 0.2 mW and 5 mW plots at the second, red dotted line. This data is evidence that the effects of the CW beam, including population transfer and geometric phases, can be quite significant and need to be considered in any such experiment with a CW beam driving a transition.

Economou and Reinecke propose using detuned hyperbolic secant pulses to create such a geometric phase [14]. They derive that, with a detuned pulse, a continuous range of phases can be produced such that the geometric phase can create rotation by any angle about the x axis [14]. In the limit that a CW beam can be considered a very long pulse, our experiment represents a first demonstration of the feasibility of this rotation method for spins in dots.

3.8 Chapter Summary

This chapter focused on manipulation of a single electron spin qubit. First, a technique of using a CW beam for initialization and readout in coherent control ex-

periments on the quantum dot electron spin was presented. Then three methods for coherently rotating the electron spin were derived and demonstrated. Circular, detuned optical pulses rotate the spin about the optical (z) axis in a few picoseconds. Magnetic field precession can cause the electric field to rotate about the field axis (x) in 33 picoseconds. Geometric phases provide a tool for optically rotating about the x axis. We demonstrated π rotations by this method using our CW beam, but pulses have been proposed to provide faster and more varied rotations [14]. A combination of these methods could achieve arbitrary rotation of the spin qubit about any axis in times much faster than the decoherence time. This work represents a major contribution toward fulfilling the DiVincenzo criteria [2].

BIBLIOGRAPHY

BIBLIOGRAPHY

[1] E. D. Kim, K. Truex, X. Xu, B. Sun, D. G. Steel, A. S. Bracker, D. Gammon, L. J. Sham, "Fast Spin Rotations by Optically Controlled Geometric Phases in a Charge-Tunable InAs Quantum Dot", *Phys. Rev. Lett.* **104**, 167401 (2010).

[2] D. P. DiVincenzo, "The Physical Implementation of Quantum Computation", *Fortschr. Phys.* **48** (2000).

[3] M. A. Nielsen, I. L. Chuang, *Quantum Computation and Quantum Information*, Cambridge University Press, Cambridge, United Kingdom, first edition (2000).

[4] X. Xu, Y. Wu, B. Sun, Q. Huang, J. Cheng, D. G. Steel, A. S. Bracker, D. Gammon, C. Emary, L. J. Sham, "Fast Spin State Initialization in a Singly-Charged InAs-GaAs Quantum Dot by Optical Cooling", *Phys. Rev. Lett.* **99**, 097401 (2007).

[5] E. D. Kim, K. Truex, A. Amo, X. Xu, D. G. Steel, A. S. Bracker, D. Gammon, L. J. Sham, "Picosecond optical spectroscopy of a single negatively charged self-assembled InAs quantum dot", *APL* **97**, 113110 (2010).

[6] P. R. Berman, V. S. Malinovsky, *Principles of Laser Spectroscopy and Quantum Optics*, Princeton University Press, Princeton, NJ, first edition (2011).

[7] Y. Wu, X. Li, L. M. Duan, D. G. Steel, D. Gammon, "Density matrix tomography through sequential coherent optical rotations of an exciton qubit in a single quantum dot.", *Physical Review Letters* **96**, 087402 (2006).

[8] F. H. L. Koppens, C. Buizert, K. J. Tielrooij, I. T. Vink, K. C. Nowack, T. Meunier, L. P. Kouwenhoven, L. M. K. Vandersypen, "Driven Coherent Oscillations of a Single Electron Spin in a Quantum Dot", *Nature* **442** (2006).

[9] X. Xu, W. Yao, B. Sun, D. G. Steel, A. S. Bracker, D. Gammon, L. J. Sham, "Optically controlled locking of the nuclear field via coherent dark-state spectroscopy", *Nature* **459**, 1105 (2009).

[10] S. M. Clark, K.-M. C. Fu, Q. Zhang, T. D. Ladd, C. Stanley, Y. Yamamoto, "Ultrafast optical spin echo for electron spins in semiconductors", *Physical Review Letters* **102**, 247601 (2009).

[11] K. K. Berggren, "Quantum computing with superconductors", *Proceedings of the IEEE* **92**, 1630 (2004).

[12] P. Meystre, M. Sargent, *Elements of Quantum Optics*, 1, Springer (2007).

[13] Y. Aharonov, J. Anandan, "Phase change during a cyclic quantum evolution", *Physical Review Letters* **58**, 1593 (1987).

[14] S. E. Economou, T. L. Reinecke, "Theory of fast optical spin rotation in a quantum dot based on geometric phases and trapped states", *Phys. Rev. Lett.* **99** (2007).

CHAPTER 4

Creating a Precursor State to Spin-Photon Entanglement: an Experimental Design[1]

4.1 Introduction

In order for a quantum computer to perform useful calculations, the computer must consist of a large network of qubits whose interactions are controllable. Liu, Yao, and Sham published a proposal for such a network in which quantum dot based qubits interact via a flying photon qubit [1]. An essential functionality of the proposed network is the ability to entangle the spin qubit and the state of the photon.

Consider a quantum dot embedded in a photonic cavity such that the cavity mode enhances spontaneous emission along the $|t+\rangle$ to $|x+\rangle$ transition but suppresses spontaneous emission along all other transitions. If this dot is prepared in the state $|\Psi^E\rangle = \frac{|x-\rangle+e^{i\phi_E}|t+\rangle}{\sqrt{2}}$, as illustrated in Figure 4.1, then the dot-cavity system is in the state

$$|\Psi^E_{system}\rangle = \frac{(|x-\rangle + e^{i\phi_E}|t+\rangle)|0\rangle_c}{\sqrt{2}}. \tag{4.1}$$

After radiative decay the system will be in a state

$$|\Psi^{decay}\rangle = \frac{(|x-\rangle|0\rangle_c + e^{i\phi_E}|x+\rangle|1\rangle_c)}{\sqrt{2}}, \tag{4.2}$$

where the states $|0\rangle_c$ and $|1\rangle_c$ represent the absence or presence of a photon in the cavity mode. If we measure whether a photon is present in the cavity, then we also

[1]This chapter was the result of encouragement by Luming Duan to pursue entanglement within the spin-exciton system.

know the spin of the electron. This procedure suggested by Yao, Liu, and Sham creates a deterministic entanglement between the emission of a photon and the electron spin [2]. Preparing a dot embedded in a photonic cavity in the state $|\Psi^E\rangle$ is thus a preliminary step to photon-spin entanglement.

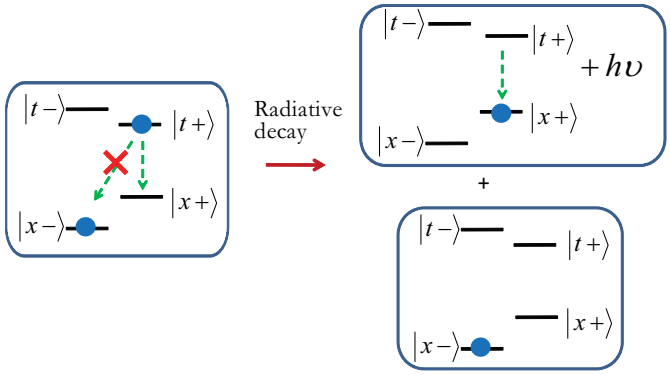

Figure 4.1: The photonic cavity modes can enhance one optical transition within the dot and suppress the others. Radiative decay leads to a superposition of two outcome states, $(|x-\rangle|0\rangle_c + e^{i\phi_E}|x+\rangle|1\rangle_c)/\sqrt{2}$ where the states $|0\rangle_c$ and $|1\rangle_c$ represent the presence or absence of a photon in the cavity mode.

This chapter presents a proposal to create the state $|\Psi^E\rangle$ in current samples, with structures as described in Chapter 2, in preparation for future studies with photonic cavity samples. As will be explained in Section 4.2, $|\Psi^E\rangle$ was created in an experiment presented in the previous chapter, but in a transient way that is unsuitable for the entanglement procedure described above. Section 4.3 proposes a detailed experimental procedure to create $|\Psi^E\rangle$ using pulsed coherent control and to measure the coherence of the created state. Section 4.4 discusses numerical simulations of the proposed experiment and its fidelity, including a comparison of two possible pulse sequences. The final section discusses the degree of entanglement present in $|\Psi^E\rangle$.

4.2 Preliminary Experiment

The entangled state $|\Psi^E\rangle$ was created in the experiment described in Section 3.7.1. As a reminder, the electron was initialized into the $|x-\rangle$ state via optical pumping by an on resonant CW beam which remained on throughout the experiment. The

electron spin was then manipulated by two circularly polarized picosecond pulses separated by a variable delay. Each pulse rotated the electron spin by 90 degrees about the optical axis since each had a pulse area of $\frac{\pi}{2}$. As described in Section 3.5, these pulses were energetically detuned so as to allow adiabatic elimination of the trion state and electron spin rotation through a two-photon Raman process [3, 4]. Between pulses the electron spin precessed about the magnetic field while simultaneously the CW beam drove Rabi oscillations between the $|x+\rangle$ and $|t+\rangle$ states. The measured signal was the absorption of the CW beam, which was tuned to the V1 transition and left on throughout the experiment. The readout signal was shown in Section 3.3 to be proportional to $[\frac{1}{2}\rho_{33}(0) + \frac{1}{2}\rho_{44}(0) + \rho_{22}(0)]$.

A subset of the experimental data and a corresponding numerical simulation are shown in Figure 4.2. The faster oscillation is the precession of the electron spin about the magnetic field, and the slower envelope represents the CW Rabi oscillation. After initialization, but before the pulses, the system is described by

$$\mathbf{c}(0) = \begin{bmatrix} c_1(0) \\ c_2(0) \\ c_3(0) \\ c_4(0) \end{bmatrix} = \begin{bmatrix} 1 \\ 0 \\ 0 \\ 0 \end{bmatrix}. \tag{4.3}$$

Equation 3.44 gives the probability amplitudes at t_1+, immediately after the first Raman pulse, as

$$\mathbf{c}(t_1) = \begin{bmatrix} \frac{\sqrt{2}}{2} \\ \frac{i\sqrt{2}}{2} \\ 0 \\ 0 \end{bmatrix}. \tag{4.4}$$

Equation 3.53 gives the effect of precession and the CW Rabi oscillations. If there is a delay of τ between pulses, the probability amplitudes immediately before the second

pulse are

$$\mathbf{c}(t_1+\tau) = \begin{bmatrix} \frac{\sqrt{2}}{2} e^{\frac{i(3\Delta_e+\Delta_h)\tau}{4}} \\ \frac{i\sqrt{2}}{2} e^{\frac{i(-\Delta_e+\Delta_h)\tau}{4}} \cos\frac{|\Omega_{CW}|\tau}{2} \\ \frac{i\sqrt{2}}{2} e^{\frac{i(-\Delta_e+\Delta_h)\tau}{4}} \sin\frac{|\Omega_{CW}|\tau}{2} \\ 0 \end{bmatrix}. \tag{4.5}$$

If $\tau = \frac{4n\pi}{|\Omega_{CW}|}$, where n is an integer, then

$$\mathbf{c}(t_1+\frac{4n\pi}{|\Omega_{CW}|}) = \begin{bmatrix} \frac{\sqrt{2}}{2} e^{\frac{i(3\Delta_e+\Delta_h)\tau}{4}} \\ \frac{i\sqrt{2}}{2} e^{\frac{i(-\Delta_e+\Delta_h)\tau}{4}} \\ 0 \\ 0 \end{bmatrix}, \tag{4.6}$$

and immediately before the second pulse the system is in an equal superposition of states $|x-\rangle$ and $|x+\rangle$. These conditions are represented by the data points where the envelope is a maxima, indicated in figure 4.2 by the blue arrows.

If instead, $\tau = \frac{4(n+\frac{1}{2})\pi}{|\Omega_{CW}|}$, then

$$\mathbf{c}(t_1+\frac{4(n+\frac{1}{2})\pi}{|\Omega_{CW}|}) = \begin{bmatrix} \frac{\sqrt{2}}{2} e^{\frac{i(3\Delta_e+\Delta_h)\tau}{4}} \\ 0 \\ \frac{i\sqrt{2}}{2} e^{\frac{i(-\Delta_e+\Delta_h)\tau}{4}} \\ 0 \end{bmatrix}, \tag{4.7}$$

which is a coherent superposition of states $|x-\rangle$, and $|t+\rangle$ and thus is our desired state. This state can be seen in the data as the minima of the envelope, which are indicated in Figure 4.2 by the red arrows.

While the state $|\Psi^E\rangle$ was created, no measurement was made of the entanglement. Furthermore, the dependence on the CW Rabi oscillation makes this method of preparation ill suited to quantitative measurements of $|\Psi^E\rangle$ or the deterministic entanglement procedure presented at the beginning of this chapter. The rate of the CW Rabi oscillation can be controlled by the power of the CW beam, but there are conflicting limitations on this rate. If the CW Rabi oscillation is too slow then radiative decay will degrade the fidelity of $|\Psi^E\rangle$. However, if the CW Rabi oscillation

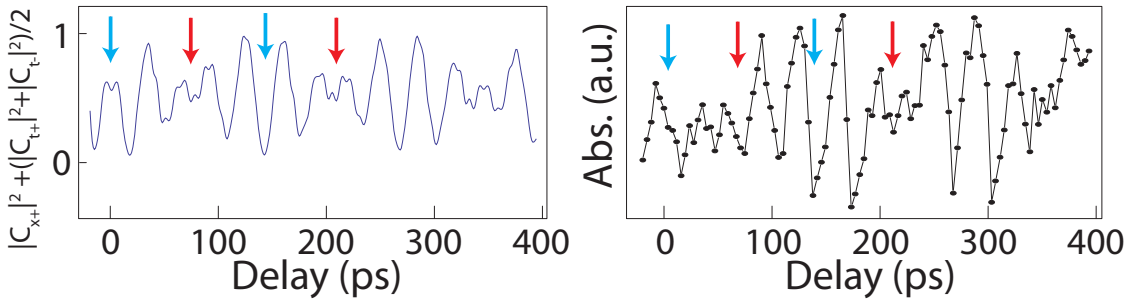

Figure 4.2: A subset of the geometric phase data from Section 3.7.1 for CW Power=13 mW. Numerical calculations (left) and data (right) for the CW absorption signal are plotted as a function of delay. The fast oscillation is the spin precession, and the envelope is due to Rabi oscillations driven by the CW beam. The blue arrows indicate times when the dot is in an equal coherent superposition of the two spin states, as described in Equation 4.6. The red arrows indicate times when the dot is in the superposition state $|\Psi^E\rangle$.

is fast then not only will the state $|\Psi^E\rangle$ be created quickly, but the CW Rabi oscillation will destroy $|\Psi^E\rangle$ quickly as well, since the CW beam remains on for the entire measurement. The next section suggests an alternate procedure to create $|\Psi^E\rangle$ that will allow for measurement and characterization of the state.

4.3 Procedure to create $|\Psi^E\rangle$

This section proposes an experimental procedure to create state $|\Psi^E\rangle$ through coherent manipulation with four optical pulses in such a manner that the state can persist, limited only by the timescales of decay and decoherence. The proposed experiment includes a measurement of the coherence of the created state, since coherence is essential for entanglement. The procedure for creating $|\Psi^E\rangle$ has three stages: (1) initialization to a pure spin ground state $|\Psi_{init}\rangle = |x-\rangle$, (2) spin rotation to $|\Psi_{spin}\rangle = \frac{-i}{\sqrt{2}}|x-\rangle - \frac{1}{\sqrt{2}}|x+\rangle$, and (3) selective excitation of the $||x+\rangle\rangle$ state such that the final state is $|\Psi^E\rangle = (|x-\rangle + e^{i\phi_E}|t+\rangle)/\sqrt{2}$. Notice that this procedure first rotates the spin qubit and then creates the exciton in two temporally separate manipulations.

4.3.1 Initialization

A CW beam on resonance with transition V1 initializes the system to state $|x-\rangle$

via optical pumping, as discussed in Section 3.2. The timing sequence of the proposed experiment is as shown in Figure 3.2. The CW beam initializes the system over several nanoseconds, then a series of pulses manipulates the system to create $|\Psi^E\rangle$. The measured signal is the absorption of the CW beam as reinitialization occurs, as calculated in Section 3.3.

4.3.2 Spin rotation

The spin rotation could be easily accomplished using a single off-resonant Raman pulse as presented in Section 3.5, however step (3) requires on resonance pulses. To avoid the need for a second pulsed laser or pulse shaping we propose a simple two pulse sequence to accomplish the effective rotation via a trion state. Starting in an initialized state $|\Psi_{init}\rangle = |x-\rangle$, we excite the system with a horizontally polarized (H) pulse with a bandwidth that covers all four optical transitions from Figure 2.8. Given that only state $|x-\rangle$is occupied, the polarization limits this optical interaction to the two level system of states $|x-\rangle$and $|t+\rangle$. Optical excitation of a two level system was treated in Section 3.4. The pulse area is π, leaving the system in $|t+\rangle$.

This horizontal pulse can then be followed by a 45 degree polarized pulse, which will couple from state $|t+\rangle$to both ground states equally. The pulse area can be chosen such that after the pulse there is zero probability of the electron being in $|t+\rangle$, leaving the electron in a coherent superposition of the ground states. To calculate the effect of this second pulse, Equation 2.29 can be simplified to a three level system by removing state $|t-\rangle$, since states $|t+\rangle$and $|t-\rangle$are not optically coupled. For a square pulse with 45 degree polarization, $\Omega_y = i\Omega_x$. With these simplifications, Equation 2.29 becomes

$$\begin{aligned} \dot{c}_1(t) &= -\tfrac{i}{2}\Omega_x c_3(t) \\ \dot{c}_2(t) &= -\tfrac{1}{2}\Omega_x c_3(t) \\ \dot{c}_3(t) &= -\tfrac{i}{2}\Omega_x c_1(t) + \tfrac{1}{2}\Omega_x c_2(t). \end{aligned} \tag{4.8}$$

The solutions to this set of equations, given the initial condition $c_3(0) = 1$ are

$$\begin{aligned} c_1(t) &= -\tfrac{i}{\sqrt{2}} \sin \tfrac{\Omega_x t}{\sqrt{2}} \\ c_2(t) &= -\tfrac{1}{\sqrt{2}} \sin \tfrac{\Omega_x t}{\sqrt{2}} \\ c_3(t) &= \cos \tfrac{\Omega_x t}{\sqrt{2}}, \end{aligned} \tag{4.9}$$

which means that the second pulse should have a power such that $\frac{\Omega_x \tau}{\sqrt{2}} = \pi$. Such a pulse will leave the dot in $|\Psi_{spin}\rangle = \frac{-i}{\sqrt{2}}|x-\rangle - \frac{1}{\sqrt{2}}|x+\rangle$. The proposed pulse sequence for creating and measuring $|\Psi^E\rangle$ is shown in Figure 4.3, with the first two frames completing the spin rotation.

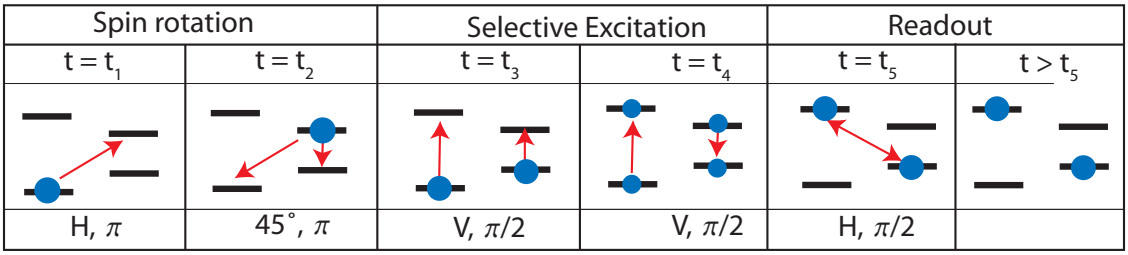

Figure 4.3: The proposed five pulse sequence for creating $|\Psi^E\rangle$ and measuring its coherence. Each panel represents a pulse with the top row indicating the purpose of the pulse, the next row labeling the time at which the pulse arrives at the dot, the red arrows indicating the transitions caused by the pulse, and the bottom row indicating its polarization and pulse area. All pulses are on-resonance.

4.3.3 Selective Excitation

We use the pulse shaping scheme proposed in Reference [5] for selective excitation from $|\Psi_{spin}\rangle = \frac{-i}{\sqrt{2}}|x-\rangle - \frac{1}{\sqrt{2}}|x+\rangle$ to $|\Psi^E\rangle = (|x-\rangle + e^{i\phi_E}|t+\rangle)/\sqrt{2}$ with two on-resonance pulses. The following is a detailed presentation of the theory.

4.3.3.1 Phase Dependence in a Two Level System

First consider a two level system with a ground state $|g\rangle$ and excited state $|e\rangle$ that is excited by two identical on-resonant pulses separated by a time δt. The incident electric field on the system is

$$\mathbf{E}(t) = \mathbf{E} \sqcap (\frac{t}{\tau}) \cos(\omega t + \phi_0) + \mathbf{E} \sqcap (\frac{t - \delta t}{\tau}) \cos(\omega(t - \delta t) + \phi_0) \tag{4.10}$$

where $\sqcap(\frac{t}{\tau})$ is again defined as

$$\sqcap(\frac{t}{\tau}) = \begin{cases} 1 & \text{if } 0 \leq t < \tau \\ 0 & \text{if } t < 0 \text{ or } t \geq \tau. \end{cases} \tag{4.11}$$

Thus the pulsewidth is τ, the relative phase between the pulse envelope and the optical carrier is ϕ_0, and the laser frequency is ω. $\mathbf{E}(t)$ and the two level system are illustrated in Figure 4.4.

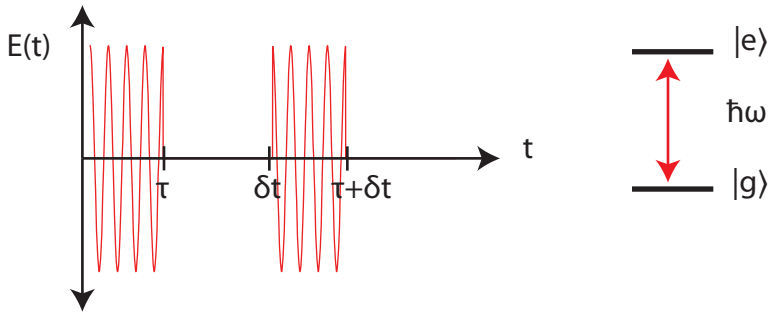

Figure 4.4: A graph of the electric field for the two square pulses defined in Equation 4.10 and a diagram of the two level system used in Section 4.3.3.1.

The field amplitude is constant for each time interval $0 \leq t < \tau$, $\tau \leq t < \delta t$, $\delta t \leq t < (\delta t + \tau)$, and $(\delta t + \tau) \leq t$. The equations of motion from Equation 3.23 for the probability amplitudes in the field interaction representation and the rotating wave approximation can be solved for each section of time and then combined. Since the pulses are on resonance, $\delta = 0$, and the probability amplitudes are constant except for the time intervals when the field is on. The probability amplitudes $c_g(t)$ and $c_e(t)$ for $t > (\tau + \delta t)$ are given by

$$\begin{bmatrix} c_g(t)e^{-i\omega t/2} \\ c_e(t)e^{i\omega t/2} \end{bmatrix} =$$

$$\begin{bmatrix} \cos\frac{\Omega\tau}{2} & -ie^{-i(\phi_0-\omega\delta t)}\sin\frac{\Omega\tau}{2} \\ -ie^{i(\phi_0-\omega\delta t)}\sin\frac{\Omega\tau}{2} & \cos\frac{\Omega\tau}{2} \end{bmatrix} \begin{bmatrix} \cos\frac{\Omega\tau}{2} & -ie^{-i\phi_0}\sin\frac{\Omega\tau}{2} \\ -ie^{i\phi_0}\sin\frac{\Omega\tau}{2} & \cos\frac{\Omega\tau}{2} \end{bmatrix} \begin{bmatrix} c_g(0) \\ c_e(0) \end{bmatrix}$$

$$= \begin{bmatrix} (\cos^2\frac{\Omega\tau}{2} - e^{i\omega\delta t}\sin^2\frac{\Omega\tau}{2})c_g(0) - (ie^{-i\phi_0} + ie^{-i(-\omega\delta t+\phi_0)})\cos\frac{\Omega\tau}{2}\sin\frac{\Omega\tau}{2}c_e(0) \\ (\cos^2\frac{\Omega\tau}{2} - e^{-i\omega\delta t}\sin^2\frac{\Omega\tau}{2})c_e(0) - (ie^{i\phi_0} + ie^{i(-\omega\delta t+\phi_0)})\cos\frac{\Omega\tau}{2}\sin\frac{\Omega\tau}{2}c_g(0) \end{bmatrix} \tag{4.12}$$

where $\Omega = -\frac{\mu E}{\hbar}$, and μ is the transition dipole moment. If we assume that the system starts in the ground state such that $c_e(0) = 0$, then the probabilities simplify to

$$\begin{aligned} |c_g(t)|^2 &= 1 - \sin^2(\Omega\tau)\cos^2\tfrac{\omega\delta t}{2} \\ |c_e(t)|^2 &= \sin^2(\Omega\tau)\cos^2\tfrac{\omega\delta t}{2}. \end{aligned} \tag{4.13}$$

Figure 4.5 plots $|c_e(t)|^2$ as a function of δt. Equation 4.13 shows that changes in the delay between two pulses (δt) on the order of the laser frequency affect whether the two pulses combine constructively or destructively. Figure 4.6 illustrates the effect of the two pulses with pulse areas ($\Omega\tau$) of $\frac{\pi}{2}$ on the Bloch vector for the two level system.

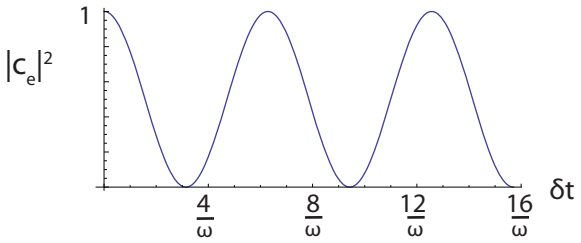

Figure 4.5: The probability of the system being in the excited state as a function of delay, δt, as given by Equation 4.13.

4.3.3.2 Phase Dependence in a Four Level System: Selective Excitation

This effect can be useful in an InAs dot's four level system. If we consider only vertically polarized pulses, then only transitions V1 and V2 will be excited (as illustrated in Figure 2.8). Because of the Zeeman splittings, the two transitions have different energies which will be labeled ω_{23} and ω_{14}. In the proposed experiment, two pulses that are tuned to halfway between the V1 and V2 transitions (with a frequency of $\frac{\omega_{23}+\omega_{14}}{2}$) are used for selective excitation. The bandwidth of these picosecond pulses is large compared to the typical Zeeman splittings, so the incident electric fields can be approximated as equal for transitions V1 and V2. Since $\frac{1}{\tau} >> \Delta_e, \Delta_h >> \Gamma_t$ in our system, where Γ_t is the radiative lifetime of the trion states, we can analytically approximate the pulses as on resonance with both transition V1 and V2.

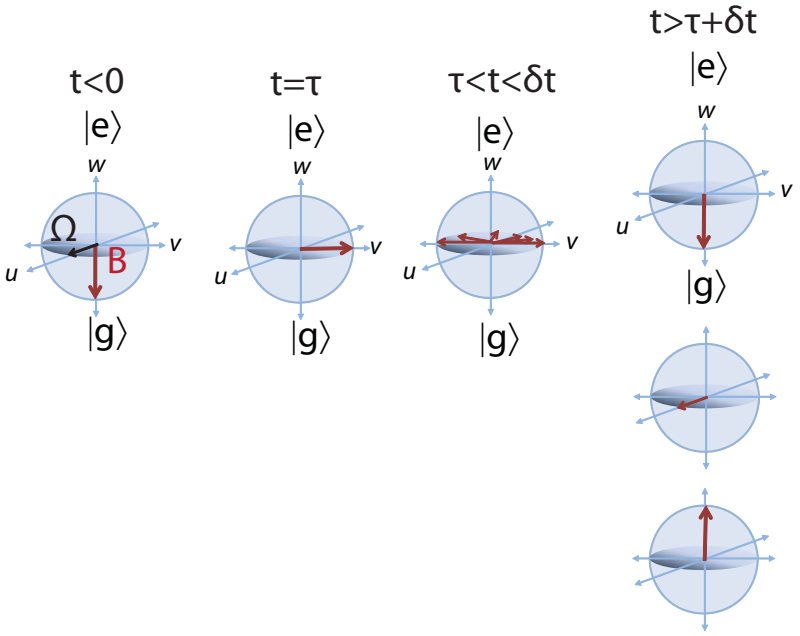

Figure 4.6: A Bloch sphere representation of the dynamics of the 2 level system driven by two pulses. See Section 3.5 for an introduction to Bloch spheres. From left to right, the first two spheres show the rotation of Bloch vector, **B**, by the first pulse about the pseudofield vector, Ω. The third sphere shows precession of the Bloch vector at the rate ω about the w axis. The three vertical spheres on the right are three possible final Bloch vector orientations after the second pulse rotates the Bloch vector about the u axis again. The final state of the Bloch vector depends on how long the Bloch vector precesses between the pulses.

Ignoring decay terms, this creates two completely uncoupled systems, so we can write down the probabilities of occupation for all four states after the two pulses by using equation 4.13 above. Recall that the first two pulses of our procedure in Figure 4.3 created an equal superposition of the two ground states, so a simple adjustment of a factor of two is necessary to account for the initial population of $\frac{1}{2}$ in each ground state instead of the value of 1 used to derive equation 4.13.

$$\begin{aligned}
|c_{\uparrow}(t)|^2 &= \tfrac{1}{2}(1-\sin^2\Omega\tau\cos^2\tfrac{\omega_{23}\delta t}{2}) \\
|c_{\uparrow\downarrow\Uparrow}(t)|^2 &= \tfrac{1}{2}(\sin^2\Omega\tau\cos^2\tfrac{\omega_{23}\delta t}{2}) \\
|c_{\downarrow}(t)|^2 &= \tfrac{1}{2}(1-\sin^2\Omega\tau\cos^2\tfrac{\omega_{14}\delta t}{2}) \\
|c_{\downarrow\uparrow\Downarrow}(t)|^2 &= \tfrac{1}{2}(\sin^2\Omega\tau\cos^2\tfrac{\omega_{14}\delta t}{2})
\end{aligned} \tag{4.14}$$

These equations show that as the delay, δt, is varied the probability oscillates between states $|x-\rangle$ and $|t-\rangle$ at a different rate than between states $|x+\rangle$ and $|t+\rangle$.

When $\delta t = \frac{\pi}{(\omega_{14}-\omega_{23})} = \frac{\pi}{(\Delta_e+\Delta_h)}$ the V1 and V2 transitions are exactly out of phase and the third and fourth pulses will add constructively (destructively) along V1 (V2) respectively, leaving the system in $|\Psi^E\rangle$. Notice that stability of the delay between the third and fourth pulses must be on the order of the optical frequency to observe this effect. Figure 4.7 illustrates how the relative phase between $|c_{\uparrow\downarrow\Uparrow}(t)|^2$ and $|c_{\downarrow\uparrow\Downarrow}(t)|^2$ evolves as a function of delay. The difference between the frequencies is exaggerated to make the effect easier to visualize. For the dot studied in this work in a 5.5 Tesla magnetic field, the two transitions are exactly out of phase at $\delta t = 10$ ps.

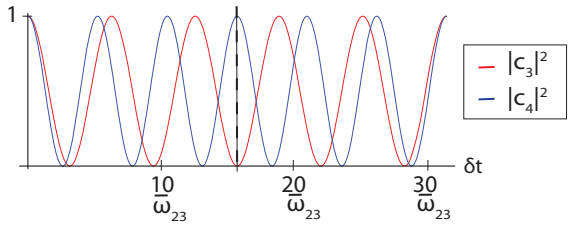

Figure 4.7: Simulation of the evolution of the relative phase between states 3 and 4 as a function of delay for $\Omega\tau = \frac{\pi}{2}$. The dotted line shows the point where $\delta t = \frac{\pi}{(\omega_{14}-\omega_{23})}$ and the two transitions are exactly out of phase. Here $\omega_{14} = 1.2\omega_{23}$ in order to exaggerate the effect and make the graph easier to read. Experimental values for the dot under study in a 5.5 Tesla magnetic field are $\omega_{14} = 1.00016\omega_{23}$.

Figure 4.8 illustrates the selective excitation effect of pulses 3 and 4 in the proposed experiment. Pulses 3 and 4 have pulse areas of $\frac{\pi}{2}$ and are vertically polarized, such that only the $|x-\rangle$ to $|t-\rangle$ and $|x+\rangle$ to $|t+\rangle$ transitions are optically driven. This enables the four level system to be treated as two decoupled two level systems, each illustrated by a Bloch sphere. After the first two pulses of the experiment, the dot is in an equal superposition of the ground states $|x-\rangle$ and $|x+\rangle$. Pulse 3 rotates both Bloch vectors by 90 degrees about the pseudofield vector, creating an equal, coherent superposition of all four states. During the time between pulses 3 and 4, the Bloch vectors precess in the equatorial plane. This precession corresponds to the accumulation of phases of the form $e^{i\omega\delta t}$. Since the two transitions have different frequencies, the two Bloch vectors precess at different rates. As calculated above, if the pulses are separated by $\delta t = \frac{\pi}{(\omega_{14}-\omega_{23})}$, then the V1 and V2 transitions are exactly out of phase. In the Bloch sphere picture that corresponds to the time when one

Bloch vector has lagged behind the other so much that the two vectors are pointing in opposite directions. If the fourth pulse arrives at exactly this time, then it will rotate one vector up to the trion state and the other vector down to the ground state, leaving the dot in state $|\Psi^E\rangle$.

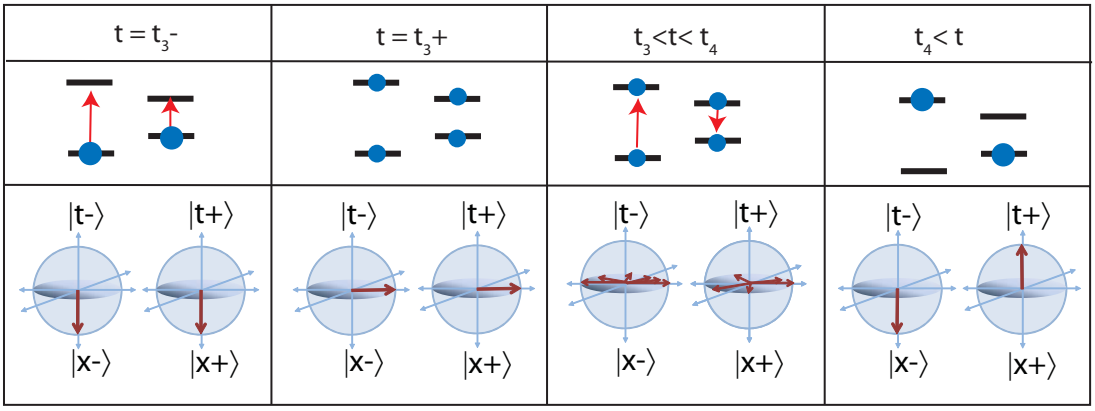

Figure 4.8: Visual representations of the effects of two vertically polarized $\frac{\pi}{2}$ pulse area pulses. The upper panels show the occupation of the four dot levels and the lower panels give Bloch sphere representations of the two optically coupled, two-level systems.

4.3.4 Measuring the coherence of $|\Psi^E\rangle$

Measuring the coherence of $|\Psi^E\rangle = (|x-\rangle + e^{i\phi_E}|t+\rangle)/\sqrt{2}$ is essential, since an incoherent state would not be useful in an entanglement procedure. The experimentally measured signal is the absorption of the CW beam, as described in Section 3.3. The coherence of $|\Psi^E\rangle$ can be measured after a fifth on-resonance horizontally polarized $\pi/2$ pulse rotates the coherence ρ_{13} into a population for readout by the cw laser.

If the state vector immediately after the fourth pulse is $c(t_4+)$, then Equation 3.46 gives the state vector immediately before the fifth pulse as

$$\begin{aligned} c_1(t_5-) &= e^{\frac{i\Delta_e(t_5-t_4)}{2}} c_1(t_4+) \\ c_2(t_5-) &= e^{\frac{-i\Delta_e(t_5-t_4)}{2}} c_2(t_4+) \\ c_3(t_5-) &= e^{\frac{i\Delta_h(t_5-t_4)}{2}} c_3(t_4+) \\ c_4(t_5-) &= e^{\frac{-i\Delta_h(t_5-t_4)}{2}} c_4(t_4+). \end{aligned} \tag{4.15}$$

Next, Equation 2.29 can be solved to find an expression for the state vector immedi-

ately after the fifth pulse, $c(t_5+)$. As before, the pulse can be approximated as square. Since $\tau << \frac{1}{\Delta_e}$ and $\tau << \frac{1}{\Delta_h}$, the effects of precession may be neglected during the pulse so that Equation 2.29 simplifies to

$$\begin{aligned}
\dot{c}_1(t) &= -\tfrac{i}{2}\Omega_x^* c_3(t) \\
\dot{c}_2(t) &= -\tfrac{i}{2}\Omega_x^* c_4(t) \\
\dot{c}_3(t) &= -\tfrac{i}{2}\Omega_x c_1(t) \\
\dot{c}_4(t) &= -\tfrac{i}{2}\Omega_x c_2(t).
\end{aligned} \tag{4.16}$$

This gives

$$\begin{aligned}
c_1(t_5+) &= \cos(\tfrac{|\Omega_x|\tau}{2})c_1(t_5-) - \tfrac{i\Omega_x^*}{|\Omega_x|}\sin(\tfrac{|\Omega_x|\tau}{2})c_3(t_5-) = \tfrac{\sqrt{2}}{2}[c_1(t_5-) - ic_3(t_5-)] \\
c_2(t_5+) &= \cos(\tfrac{|\Omega_x|\tau}{2})c_2(t_5-) - \tfrac{i\Omega_x^*}{|\Omega_x|}\sin(\tfrac{|\Omega_x|\tau}{2})c_4(t_5-) = \tfrac{\sqrt{2}}{2}[c_2(t_5-) - ic_4(t_5-)] \\
c_3(t_5+) &= \cos(\tfrac{|\Omega_x|\tau}{2})c_3(t_5-) - \tfrac{i\Omega_x}{|\Omega_x|}\sin(\tfrac{|\Omega_x|\tau}{2})c_1(t_5-) = \tfrac{\sqrt{2}}{2}[c_3(t_5-) - ic_1(t_5-)] \\
c_4(t_5+) &= \cos(\tfrac{|\Omega_x|\tau}{2})c_4(t_5-) - \tfrac{i\Omega_x}{|\Omega_x|}\sin(\tfrac{|\Omega_x|\tau}{2})c_2(t_5-) = \tfrac{\sqrt{2}}{2}[c_4(t_5-) - ic_2(t_5-)]
\end{aligned} \tag{4.17}$$

for Ω_x real and $\Omega_x\tau = \frac{\pi}{2}$. Substituting Equation 4.15 into Equation 4.17 gives the state vector immediately after the fifth pulse in terms of the state vector immediately after the fourth pulse. If $c_2(t_5-) = c_4(t_5-) = 0$, then Equation 4.17 can be rewritten in the form of a rotation matrix as

$$\begin{bmatrix} c_1(t_5+) \\ c_3(t_5+) \end{bmatrix} = \begin{bmatrix} \cos[\frac{\theta}{2}] & -ie^{-i\phi}\sin[\frac{\theta}{2}] \\ -ie^{i\phi}\sin[\frac{\theta}{2}] & \cos[\frac{\theta}{2}] \end{bmatrix} \begin{bmatrix} c_1(t_5-) \\ c_3(t_5-), \end{bmatrix} \tag{4.18}$$

where $\theta = |\Omega_x|\tau$ and $\Omega_x = |\Omega_x|e^{i\phi}$.

To find the measured signal, recall that the CW absorption signal was found to be proportional to $\frac{1}{2}\rho_{33} + \frac{1}{2}\rho_{44} + \rho_{22}$, where the density matrix elements are evaluated after the final pulse. In this case,

$$\begin{aligned}
\tfrac{1}{2}\rho_{33}(t_5-) + \tfrac{1}{2}\rho_{44}(t_5-) + \rho_{22}(t_5-) = \tfrac{1}{4}(\rho_{11}(t_4+) + \rho_{33}(t_4+) + 3(\rho_{22}(t_4+) + \rho_{44}(t_4+)) \\
+2\mathrm{Im}[(\rho_{42}(t_4+) + \rho_{13}(t_4+))e^{\frac{i}{2}(t_5-t_4)(\Delta_e-\Delta_h)}]).
\end{aligned} \tag{4.19}$$

The probability amplitudes and density matrix elements used here were defined in Chapter 2 in the field interaction picture. To properly write the time dependence of the absorption signal, we must convert back to density matrix elements in the

normal picture, $\tilde{\rho}$, by way of Equation 2.22. Ideally, immediately after the fourth pulse $c(t_4+) = |\Psi^E\rangle = c_1|x-\rangle + c_2|t+\rangle$, and thus the CW absorption signal simplifies to

$$\frac{1}{2}\rho_{33}(t_5-)+\frac{1}{2}\rho_{44}(t_5-)+\rho_{22}(t_5-) = \frac{1}{4}(\rho_{11}(t_4+)+\rho_{33}(t_4+)+2\mathrm{Im}[\tilde{\rho}_{13}(t_4+)e^{\frac{i}{2}\omega_{13}(t_5-t_4)}]). \tag{4.20}$$

Thus if the delay between pulses 4 and 5 is varied and is stable on the scale of ω_{13}, the CW absorption shows an oscillation with an amplitude that corresponds to the coherence of $|\Psi^E\rangle$ after pulse 4. Equation 4.20 is plotted for sample values in Figure 4.9.

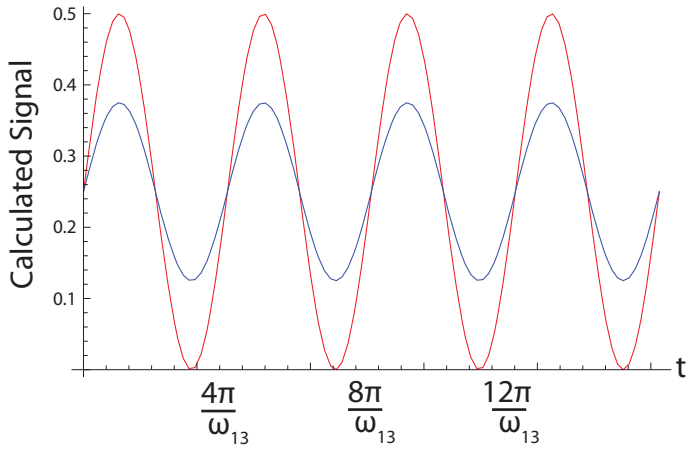

Figure 4.9: A plot of Equation 4.20 for $\rho_{11}(t_4+) = \rho_{33}(t_4+) = .5$. The red plot is with $\rho_{13} = .5$, and the blue plot is with $\rho_{13} = .25$(blue). Notice that the amplitude of the oscillation is a measure of the coherence.

4.4 Numerical Simulations Reveal Advantages of Two Pulse Selective Excitation

Numerical solutions to the density matrix equations, Equation 2.32, allow a test of how well realistic experimental parameters can reproduce the theory from the preceding sections. Sources of deviation from the theory include the limited pulse bandwidth, which does not actually couple all four transitions equally, slight overlap of the pulses in time, trion state decay, and decoherence. It should be noted that if the

pulse bandwidth is overly narrow then detuning effects can lead to major qualitative deviations from the desired manipulations. In the simulation of the full four pulse sequence,

$$\begin{aligned}\Omega_x(t) &= \tfrac{i\mu}{\hbar}[E_1\mathrm{sech}(\tfrac{t-t_1}{\tau}) + E_2\mathrm{sech}(\tfrac{t-t_2}{\tau})] \\ \Omega_y(t) &= \tfrac{-\mu}{\hbar}[E_2\mathrm{sech}(\tfrac{t-t_2}{\tau}) + E_3\mathrm{sech}(\tfrac{t-t_3}{\tau}) + E_3\mathrm{sech}(\tfrac{t-t_4}{\tau})e^{-i\omega t_4}]\end{aligned} \tag{4.21}$$

with τ=1.1 ps, t_1=0 ps, t_2=5 ps , t_3=10 ps, and t_4=20.5013 ps. The density matrix was initialized such that $\rho_{11}(0) = 1$. The field amplitudes and the value for t_4 were determined such that they gave the result most similar to $|\Psi^E\rangle$. Values of $\Gamma_t = 1.17 * 10^9 s^{-1}$ and $\gamma_e = \gamma_h = 10^9 s^{-1}$ were used [6, 7].

A gate is often characterized by its fidelity, F, defined as

$$F = \overline{|\langle\psi|U_P^\dagger U_I|\psi\rangle|}, \tag{4.22}$$

where U_I is the ideal unitary gate operator, U_P is the operation of the physical gate, and the overbar indicates an average over all possible initial states [8]. This can be modified to

$$\mathrm{F}(\rho_I, \rho_P) = \mathrm{Tr}\sqrt{\rho_I \rho_P} \tag{4.23}$$

to take decay and decoherence into account [9]. Here the fidelity F(ρ_{theory},ρ_{sim}) is calculated to compare the ideal,theoretical result of the proposed experiment to the simulated result.

The theoretical calculation uses a formalism of 4x4 transfer matrices in the probability amplitude picture, where each matrix represents either the instantaneous action of a pulse or the evolution of the phase of the states between pulses. This is similar to the development in the previous sections. When decay and decoherence are neglected, the transfer matrix calculation and the numerical simulation agree with a fidelity of 0.999. Including decay and decoherence in the simulation only degrades the fidelity to 0.987, which is a small difference because the total time required for the entire four pulse sequence is only 25 ps. Including the effect of a 200μW CW beam only lowers the fidelity to 0.985.

An alternative approach to the experiment would be to replace pulses 3 and 4 with a single pulse that has a narrow enough bandwidth that it only excites a single

transition. This pulse would be centered at ω_{23}. This method must balance having narrow enough bandwidth with the effects of decay and decoherence that become problematic for longer pulses. Due to this trade-off, the highest fidelity possible for this single pulse in the presence of decay and decoherence is 0.989 for a pulse with τ=6 ps. If the length of the operation is arbitrarily defined as the time interval between the 4% power point on the leading edge of the first pulse and the 4% power point on the falling edge of the final pulse, then this single pulse operation is 29 ps long. Comparatively, a calculation of only the selective excitation pulses, 3 and 4, yields a fidelity of 0.995 and an operation time of only 14 ps. Thus the two pulse selective excitation method gives more ideal results in a shorter operation time. The two pulse method is particularly useful in our lab as the MIRA laser cannot directly produce pulses with bandwidths narrow enough to use the single pulse method, and we do not have the power to spare to do simple spectral filtering. An electro-optic modulator can produce a 200 ps pulse from a CW beam, but decay would cause such a long pulse to have a fidelity of 0.879 at best.

4.5 Partial Entanglement of $|\Psi^E\rangle$

Given that state $|\Psi^E\rangle$ leads, upon radiative decay in a cavity, to entanglement between the electron spin and the presence of a photon in the cavity mode, it is natural to wonder whether $|\Psi^E\rangle$ itself is an entangled state. This is a complicated question to answer. If the trion is written as a product of a spin and an exciton, then $|\Psi^E\rangle$ can be written in an analogous form to $|\Psi^{decay}\rangle$ since the exciton radiatively recombines to form the photon. $|\Psi^{decay}\rangle$ is known to be a maximally entangled state. However, in a dot the electrons are sufficiently close together that their fermionic properties do not allow the above mentioned factorization of the many particle trion state.

To more clearly define whether $|\Psi^E\rangle$ is entangled, Appendix A calculates its entropy of entanglement. Entropy of entanglement, S, is a common measure of the entanglement of a state that exists in a composite Hilbert space [10]. It is defined

such that a separable product state has S=0 and a maximally entangled state has $S = \log_2 d$ where d is the Hilbert space dimension of the smaller subsystem. The calculation in Appendix A finds that S=.92 for $|\Psi^E\rangle$. This measurement used the spin of one electron as one subsystem, so the dimension of the smallest Hilbert space is 2 for the two spin states. The maximum possible entropy is therefore 1. Thus, the entropy of entanglement calculation tells us that there is a partial entanglement between the measured spin of an electron in $|\Psi^E\rangle$ and the many particle conditional state that remains after the measurement. This represents a partial entanglement of internal variables of the single dot. .The entanglement is not maximal because when a spin down electron is measured there are two possible conditional states that the system could be left in. By contrast, the state $|\Psi^{decay}\rangle$ created after $|\Psi^E\rangle$ radiatively decays is maximally entangled.

4.6 Chapter Summary

This chapter presented a proposed experiment to create $|\Psi^E\rangle = \frac{1}{\sqrt{2}}(|x-\rangle + e^{i\phi_E}|t+\rangle)$ with a sequence of four pulses, such that the state is stable over time except for the effects of decay. A proposed fifth pulse can measure the coherence of the created state, as both confirmation of the state's coherence and as a demonstration of the possibility of performing measurements. Numerical simulations show that this proposed experiment can have high fidelities for parameters that are experimentally relevant.

The state $|\Psi^E\rangle$ posesses a partially entanglement of internal variables. Additionally, as explained in the introduction, if the coherent state $|\Psi^E_{system}\rangle$ were created in a dot in an appropriate optical cavity, it would decay to the state $|\Psi^{decay}\rangle = (|x-\rangle|0\rangle_c + e^{i\phi_E}|x+\rangle|1\rangle_c)/\sqrt{2}$ which possesses maximal entanglement between the electron spin and the occupation of the cavity mode. Achieving entanglement between a spin and a photon is an important step toward scaling quantum computers to a useful size. The next chapter will discuss ongoing efforts toward the goal of spin-photon entanglement.

BIBLIOGRAPHY

BIBLIOGRAPHY

[1] R.-B. Liu, W. Yao, L. J. Sham, "Quantum computing by optical control of electron spins", *Advances in Physics* **59**, 69 (2010).

[2] W. Yao, L. Ren-Bau, L. J. Sham, "Theory of Control of the Spin-Photon Interface for Quantum Networks", *Phys. Rev. Lett.* **95** (2005).

[3] D. Press, T. D. Ladd, B. Zhang, Y. Yamamoto, "Complete quantum control of a single quantum dot spin using ultrafast optical pulses", **456**, 218 (2008).

[4] E. D. Kim, K. Truex, X. Xu, B. Sun, D. G. Steel, A. S. Bracker, D. Gammon, L. J. Sham, "Fast Spin Rotations by Optically Controlled Geometric Phases in a Charge-Tunable InAs Quantum Dot", *Phys. Rev. Lett.* **104**, 167401 (2010).

[5] C. Piermarocchi, P. Chen, Y. S. Dale, L. J. Sham, "Theory of fast quantum control of exciton dynamics in semiconductor quantum dots", *Phys. Rev. B* **65**, 075307 (2002).

[6] E. D. Kim, K. Truex, A. Amo, X. Xu, D. G. Steel, A. S. Bracker, D. Gammon, L. J. Sham, "Picosecond optical spectroscopy of a single negatively charged self-assembled InAs quantum dot", *APL* **97**, 113110 (2010).

[7] I. A. Merkulov, A. L. Efros, M. Rosen, "Electron spin relaxation by nuclei in semiconductor quantum dots", *Phys. Rev. B* **65**, 205309 (2002).

[8] J. F. Poyatos, J. I. Cirac, P. Zoller, "Complete Characterization of a Quantum Process: The Two-Bit Quantum Gate", *Phys. Rev. Lett.* **78**, 390 (1997).

[9] X. Li, Y. Wu, D. Steel, D. Gammon, T. H. Stievater, D. S. Katzer, D. Park, C. Piermarocchi, L. J. Sham, "An All-Optical Quantum Gate in a Semiconductor Quantum Dot", *Science* **301**, 809 (2003).

[10] C. H. Bennett, H. J. Bernstein, S. Popescu, B. Schumacher, "Concentrating Partial Entanglement by Local Operations", *Physical Review A* **53**, 20 (1995).

CHAPTER 5

Summary and Future Directions

5.1 Summary

This research is one part of a larger effort to implement quantum computing, motivated by the potential to solve important problems such as factoring, searching, and simulating quantum systems faster than is possible with classical computers. Optically driven self-assembled quantum dots are leading candidates for quantum computers because of their potential for high speed gate operations and relatively compact design. The spin of an electron in a self-assembled dot has shown much promise as a qubit. Our group has previously demonstrated fast optical initialization via optical pumping, and a relatively long spin decoherence time which can be lengthened by nuclear spin narrowing. This thesis addressed two additional requirements for a physical quantum computer based on spins in self-assembled quantum dots: a universal set of gates and a scalable system of qubits. Both were addressed primarily through coherent control of the spin state in a magnetic field with optical pulses.

The sample structure and material properties are critical to optical coherent control of spin qubits in single dots. The micron aluminum apertures on the surface of our sample allow optical studies of a single quantum dot, which is optimal for quantum computing studies since the decoherence time for an ensemble is generally shorter than that of a single dot. The Schottky diode structure of our sample enables charging the dot with a single electron whose spin serves as the quantum bit. The confinement of the quantum dot leads to discrete energy levels and suppressed many-body effects,

which, in combination with the long decoherence time of the electron spin, creates a promising candidate for scalable quantum computing architectures. Spin-orbit coupling of the dot in a magnetic field applied in the Voigt geometry provides a mixing term that allows optical transitions between the two electron spin states, enabling optical control of the spin qubit. Photoluminescence and modulated absorption were used as initial characterization techniques to identify the dot transition energies, the voltage range over which the dot is singly charged, the dot's Stark shift, and the g factors. These parameters characterize the four optical transitions as a function of sample bias and applied magnetic field strength.

The most general form of a single qubit gate is an arbitrary rotation. This work addressed the requirement for single qubit gates through demonstrations of coherent rotations of the electron spin. The general experimental technique used for all coherent control measurements in this thesis consisted of initializing the spin qubit using an on resonant optical pumping CW beam. This CW beam remained on the dot throughout the pulsed manipulations, and the absorption of this beam provided the readout signal.

Using these initialization and readout methods, it was demonstrated that a detuned optical pulse causes rapid rotations about the optical axis via a near resonant stimulated Raman process involving the trion. Coherent rotations of arbitrary angle were demonstrated using picosecond pulses. Several control experiments using different polarizations and detunings clearly distinguished this two photon Raman process from qualitatively similar data due to resonant single photon excitation processes. Complete 2π rotations were achieved during the picosecond pulse. Precession of the spin qubit about the magnetic field between two such stimulated Raman pulses provides rotation about an orthogonal axis. Arbitrary rotation angles were achieved by varying the time between the Raman rotation pulses, and the speed of the rotation depends on the magnetic field strength, with a 2π rotation requiring 33 picoseconds in a 6.6 Tesla magnetic field.

Geometric phases were detected in quantum dots for the first time, due to cyclic Rabi oscillations driven by the continuous-wave readout laser that coupled one spin

state to an optically excited state. These geometric phases provide another method of spin rotation and can be used in a gate. A limitation of this method is that the CW laser power determines the time required for the rotation, and a high CW power of 13 mW is necessary to achieve a 2π rotation in 250 ps. Any combination of these methods that provides spin rotation about two orthogonal axes can be combined with a phase gate to accomplish any unitary single qubit gate.

Implementations of quantum computing must be scalable, since a large network of qubits will be necessary in order to perform useful calculations. It has been proposed that entanglement between non-adjacent qubits could occur via a photon, provided the photon can be entangled with the spin qubit. This thesis presented a detailed experimental procedure for creating an entanglement within a quantum dot spin-exciton system, as a preliminary step to spin-photon entanglement. The proposed procedure uses a five pulse sequence to create a precursor state and measure its coherence. Creating this precursor state in a quantum dot embedded in an appropriate cavity and allowing radiative decay deterministically creates entanglement between the spin qubit and the presence of a photon in the cavity. Numerical simulations of the proposed design using experimentally relevant values predict that the precursor state can be achieved with high fidelity.

5.2 Future Directions

This section proposes several potential future experiments that are extensions of results presented in this thesis.

5.2.1 Gating the Initialization Beam

As observed in Section 3.7.1, the CW beam can have a significant effect on the spin qubit between pulses. While these effects can be useful, often they are not part of the desired operation, so it would be beneficial to design a method for gating off the initialization laser during the pulse manipulations. Initialization requires a few nanoseconds [1], and the pulse repetition rate is 13 nanoseconds, so an appropriate

switching time would be approximately one nanosecond. This speed requirement suggests the use of a lithium niobate electro-optic modulator that we have purchased with a bandwidth well above a GHz. The modulator is quite challenging to use, largely because of a photorefractive effect inherent in lithium niobate, but it does have the ability to produce a long pulse with a peak power of up to 200 μW, which is sufficient for initialization and readout. It will be necessary to synchronize the modulator with the modelocked titanium:sapphire laser producing the picosecond manipulation pulses.

5.2.2 Rotations due to Geometric Phases Imparted by Optical Pulses

Section 3.7.1 demonstrated the generation of a π geometric phase shift by an on resonant continuous wave (CW) laser. While detuning the CW laser would allow the creation of arbitrary geometric phases that take the form of rotations about the x (magnetic field) axis [2], the use of a CW laser means the rotation would be continuously occurring. Additionally, high laser powers are necessary to obtain fast rotations, as can be observed from Figure 3.11. Thus, an experimental demonstration of the proposal by Economou and Reinecke [3] to use the geometric phases imparted by detuned optical pulses to create spin rotations should provide a superior method for rotation about the x axis.

To summarize the proposal, a vertically polarized pulse would be tuned such that $\omega_{pulse} = \frac{(\omega_{14}+\omega_{23})}{2}$. In this configuration the detuning is negative from one transition and positive from the other, which leads to geometric phases imparted that are of opposite signs. The effect of these geometric phases is a rotation about the x axis by an angle determined by the ratio of the pulse bandwidth to the splitting $\omega_{14} + \omega_{23}$. Thus for a given magnetic field, the desired rotation angle determines the bandwidth, and then the pulse power can be selected such that no trion population is created. The bandwidth will determine how fast the rotation occurs. A detailed experimental procedure for attempting such an implementation is described in reference [4], but it will require some form of pulse shaping to readily control the pulse bandwidth. A

successful implementation of rotations about the x axis with detuned optical pulses, when combined with the fast optical rotations from Section 3.5, would enable purely optical fast rotations without the need for a high magnetic field.

5.2.3 Implementation of the Experimental Design from Chapter 4

A well defined future experiment would be implementing the proposal from Chapter 4 to create the precursor state $|\Psi^E\rangle$. A significant challenge to performing this experiment will be achieving the required stability of delay between the last three pulses in the proposed experiment. As mentioned in Section 4.3, it is essential that the delay between pulses 3 and 4 is stable to less than an optical cycle in order to obtain selective excitation in the four level system. For perspective, calculations show that if this delay varies by half of an optical cycle then the detected signal will be 40% of its expected value. This reduction in the readout signal indicates population present in states 2 and 4, where there would ideally be none. Given the light wavelength, variation in the path difference must be significantly less than a micron. Additionally, the coherence measurement above requires scanning the delay between the fourth and fifth pulse with a resolution small enough to observe oscillations at the optical frequency. Appendix B presents an interferometer that has been designed by Leon Webster to address these requirements.

Another challenge will be obtaining sufficient signal to noise. In the experiments in Chapter 3, the pulses were blocked from the photodetector with a polarizer. However, the proposed experiment in Chapter 4 requires pulses that are copolarized with the detected CW laser, so they cannot be blocked using polarization. The pulses cannot be separated from the CW beam spatially due to diffraction from the small apertures in the aluminum sample mask. It is best to block the pulses as much as possible because they contribute optical shot noise to the measurement. One possible solution is to use the modes of a Fabry-Pérot etalon to spectrally filter most of the power from the broadband pulses while passing the narrowband CW beam. Appendix C discusses a Fabry-Pérot etalon that I designed and ordered for this purpose.

5.2.4 Quantum dots in cavities

Once the creation of the precursor state, $|\Psi^E\rangle$ has been demonstrated in our current quantum dot samples, a new sample where the dots are embedded in a cavity will be needed to carry out the proposed demonstration of spin-photon entanglement [5]. Only a weak coupling between the dot and cavity is necessary, such that the Purcell effect will enhance spontaneous emission for optical dot transitions which are on resonance with the cavity and suppress spontaneous emission along those transitions that are off-resonance. The study of optical microcavities and their coupling with quantum dots has become an active research area. Several different types of cavities are being explored, including photonic crystal cavities in two and three dimensions [6] and micropillar cavities [7]. The wavelength dependent suppression and enhancement of spontaneous emission has been demonstrated with photonic crystals [8] and high Q microresonators [9].

Our group has studied one sample made by the Naval Research Lab that had a quantum dot layer between Bragg gratings made from layers of GaAs-Te and AlAs-Te. This cavity had a resonance at 970 nm and a broad cavity mode of about 5 nm. Study of this sample was inhibited by unusual voltage modulation data and the observation of sudden changes in the wavelength of the dot resonances. We hypothesize that the voltage controlled charging is complicated by the presence of the Bragg grating layers, perhaps by the trapping of charges in these layers.

Dots embedded within cavities could enable full implementation of the spin-photon entanglement protocol proposed by Yao, Liu, and Sham [5]. Additionally, cavities can enhance the overall light-dot interaction and increase collected signals. However, careful design of the type of cavity will be necessary to obtain a sample suitable for experiments involving voltage modulation and tailored to the desired experiment.

Completing any of these future experiments would augment the progress demonstrated in this thesis toward quantum computation using quantum dot based spin qubits.

BIBLIOGRAPHY

BIBLIOGRAPHY

[1] X. Xu, Y. Wu, B. Sun, Q. Huang, J. Cheng, D. G. Steel, A. S. Bracker, D. Gammon, C. Emary, L. J. Sham, "Fast Spin State Initialization in a Singly-Charged InAs-GaAs Quantum Dot by Optical Cooling", *Phys. Rev. Lett.* **99**, 097401 (2007).

[2] E. D. Kim, K. Truex, X. Xu, B. Sun, D. G. Steel, A. S. Bracker, D. Gammon, L. J. Sham, "Fast Spin Rotations by Optically Controlled Geometric Phases in a Charge-Tunable InAs Quantum Dot", *Phys. Rev. Lett.* **104**, 167401 (2010).

[3] S. E. Economou, T. L. Reinecke, "Theory of fast optical spin rotation in a quantum dot based on geometric phases and trapped states", *Phys. Rev. Lett.* **99** (2007).

[4] E. D. Kim, *The Coherent Optical Spectroscopy and Control of an Electron Spin in a Self-Assembled Quantum Dot for Quantum Computing*, PhD in applied physics, University of Michigan (2009).

[5] W. Yao, L. Ren-Bau, L. J. Sham, "Theory of Control of the Spin-Photon Interface for Quantum Networks", *Phys. Rev. Lett.* **95** (2005).

[6] S. Noda, M. Fujita, T. Asano, "Spontaneous-emission control by photonic crystals and nanocavities", *Nature Photonics* **1**, 449 (2007).

[7] J. P. Reithmaier, G. Sek, A. Lffler, C. Hofmann, S. Kuhn, S. Reitzenstein, L. V. Keldysh, V. D. Kulakovskii, T. L. Reinecke, A. Forchel, "Strong coupling in a single quantum dot-semiconductor microcavity system.", *Nature* **432**, 197 (2004).

[8] P. Lodahl, A. Floris Van Driel, I. S. Nikolaev, A. Irman, K. Overgaag, D. Vanmaekelbergh, W. L. Vos, "Controlling the dynamics of spontaneous emission from quantum dots by photonic crystals.", *Nature* **430**, 654 (2004).

[9] M. Bayer, T. L. Reinecke, F. Weidner, A. Larionov, A. McDonald, A. Forchel, "Inhibition and Enhancement of the Spontaneous Emission of Quantum Dots in Structured Microresonators", *Phys. Rev. Lett.* **86**, 3168 (2001).

APPENDICES

APPENDIX A

Quantifying Entanglement[1]

This appendix defines how to calculate the entropy of entanglement, calculates the entropy of entanglement of the EPR state as a simple example, and finally calculates the entropy of entanglement of $|\Psi^E\rangle$ from Chapter 4. The entropy of entanglement of a composite system is based on definitions from quantum measurement theory, so the discussion starts with those definitions. The introductory discussion is a combination of the presentations in the textbooks by Schumacher and Westmoreland [1] and Nielson and Chuang [2].

A.1 Projective Measurements

Consider a state $|\Psi\rangle$ that exists in the composite system AB, composed of subsystems A and B. If a projective measurement is made on subsystem A in the basis $\{|a\rangle\}$ which results in a measured eigenvalue a, then the conditional state of subsytem B given this measurement outcome is

$$|\psi_a^B\rangle = \frac{\langle a|\Psi\rangle}{\sqrt{p(a)}}, \tag{A.1}$$

where

$$p(a) = \langle\Psi|a\rangle\langle a|\Psi\rangle \tag{A.2}$$

is the probability of measuring eigenvalue a.

[1]Lu Sham provided many instructive discussions that guided these calculations.

A.2 Entropy of Entanglement

If state $|\Psi\rangle$ exists in the composite system AB, then its entropy of entanglement, S, (between systems A and B) can be found from

$$S(\rho_B) = -\mathrm{Tr}(\rho_B \log_2 \rho_B), \tag{A.3}$$

where ρ_A is a reduced density matrix defined as

$$\rho_B = \mathrm{Tr}_A |\Psi\rangle\langle\Psi|. \tag{A.4}$$

Tr_A is the partial trace over system A. If system A can be described by the basis $\{|a\rangle\}$ and ρ_{AB} is the density matrix for the state of the composite system, then

$$\rho_B = \sum_a \langle a|\rho_{AB}|a\rangle = \sum_a p(a)|\psi_a^B\rangle\langle\psi_a^B|, \tag{A.5}$$

where the sum is over all eigenvalues of system A.

A.3 EPR Example - Method 1

As an example of how to apply the definitions above, consider the EPR state of two electrons where the wavevector (k_1 or k_2) and spin (up or down) are correlated. Since electrons are fermions, the total wavefunction must be antisymmetric under exchange. Therefore,

$$|\Psi_1\rangle = \frac{1}{\sqrt{2}}(|k_1,+\rangle_1|k_2,-\rangle_2 - |k_2,-\rangle_1|k_1,+\rangle_2). \tag{A.6}$$

For a more complicated system, the Slater determinant can be used to find the anti-symmetric wavefunction [3].

The basis $\{|k_1\rangle, |k_2\rangle\}$ describes one sub-system, so one possible reduced density matrix is

$$\rho_{spin} = {}_1\langle k_1|\psi_1\rangle\langle\psi_1|k_1\rangle_1 + {}_1\langle k_2|\psi_1\rangle\langle\psi_1|k_2\rangle_1 = \frac{1}{2}(|+\rangle\langle+| + |-\rangle\langle-|). \tag{A.7}$$

A measurement was made on the wavevector space, resulting in a mixture of conditional spin states. The entropy of entanglement is $S(\rho_{spin}) = -2(\frac{1}{2}\log_2\frac{1}{2}) = 1$ as expected, as this is known to be a maximally entangled state.

A.4 EPR Example - Method 2

This system can be alternately defined by fermion annihilation and creation operators acting on a null state, where $c^\dagger_{k_1,+}|0\rangle$ represents a single electron with wavevector k_1 and spin up. With these definitions,

$$|\Psi_1\rangle = c^\dagger_{k_1,+}c^\dagger_{k_2,-}|0\rangle. \tag{A.8}$$

Measurement can be redefined in terms of a measurement operator M_a which acts only on subsystem A and measures the eigenvalue a with probability

$$p(a) = \langle\Psi|M^\dagger_a M_a|\Psi\rangle. \tag{A.9}$$

The system after measurement is given by

$$|\psi^B_a\rangle = \frac{M_m|\Psi\rangle}{\sqrt{p(a)}}. \tag{A.10}$$

A completeness relation requires that

$$\sum_a p(a) = 1. \tag{A.11}$$

A comparison of the two formalisms for measurement suggests that annihilation operators are appropriate measurement operators. For $|\Psi_1\rangle$, the completeness relation requires normalization of the operators such that

$$\begin{aligned} M_{k_1,+} &= \tfrac{1}{\sqrt{2}}c_{k_1,+} \\ M_{k_2,-} &= \tfrac{1}{\sqrt{2}}c_{k_2,-}. \end{aligned} \tag{A.12}$$

The reduced density matrix is still given by

$$\rho_B = \sum_a p(a)|\psi^B_a\rangle\langle\psi^B_a|. \tag{A.13}$$

For $|\Psi_1\rangle$, p(k_1,+)= p(k_2,-)=$\frac{1}{2}$, so

$$\begin{aligned} \rho_B &= \tfrac{1}{2}|\psi^B_{k_1,+}\rangle\langle\psi^B_{k_1,+}| + \tfrac{1}{2}|\psi^B_{k_2,-}\rangle\langle\psi^B_{k_2,-}| \\ &= \tfrac{1}{2}c_{k_1,+}|\Psi_1\rangle\langle\Psi_1|c^\dagger_{k_1,+} + \tfrac{1}{2}c_{k_2,-}|\Psi_1\rangle\langle\Psi_1|c^\dagger_{k_2,-} \\ &= \tfrac{1}{2}c^\dagger_{k_2,-}|0\rangle\langle 0|c_{k_2,-} + \tfrac{1}{2}c^\dagger_{k_1,+}|0\rangle\langle 0|c_{k_1,+}, \end{aligned} \tag{A.14}$$

which is equivalent to Equation A.7 and also yields an entropy of entanglement of 1.

A.5 Quantifying the Entanglement of $|\Psi^E\rangle$

The goal of this section is to calculate the entropy of entanglement of the state $|\Psi^E\rangle$, created in Chapter 4, using the tools introduced above. The four levels in Figure 2.8 can be defined in terms of a picture of three electrons distributed between the conduction and valence band as

$$|1\rangle = c_-^\dagger v_+^\dagger v_-^\dagger|0\rangle \quad |2\rangle = c_+^\dagger v_+^\dagger v_-^\dagger|0\rangle \quad |3\rangle = c_-^\dagger c_+^\dagger v_+^\dagger|0\rangle \quad |4\rangle = c_-^\dagger c_+^\dagger v_-^\dagger|0\rangle \tag{A.15}$$

where $c^\dagger$ creates an electron in the conduction band and $v^\dagger$ creates an electron in the valence band. With these definitions,

$$|\Psi^E\rangle \equiv \frac{1}{\sqrt{2}}(|1\rangle + e^{i\phi_E}|3\rangle) = \frac{1}{\sqrt{2}}(c_-^\dagger v_+^\dagger v_-^\dagger|0\rangle + e^{i\phi_E} c_-^\dagger c_+^\dagger v_+^\dagger|0\rangle). \tag{A.16}$$

A possible set of unnormalized measurement operators is $\{c_-, c_+\}$.

$$\langle\Psi^E|c_+^\dagger c_+|\Psi^E\rangle + \langle\Psi^E|c_-^\dagger c_-|\Psi^E\rangle = \frac{1}{2} + 1 = \frac{3}{2} \tag{A.17}$$

so the normalized measurement operators are

$$M_+ = \sqrt{\tfrac{2}{3}} c_+ \quad M_- = \sqrt{\tfrac{2}{3}} c_-. \tag{A.18}$$

Following the same procedure as in the preceding section, the reduced density matrix produced by these measurement operators can be calculated.

$$\begin{aligned} |\psi_+\rangle &= \tfrac{M_+|\Psi^E\rangle}{\sqrt{p(+)}} = \sqrt{2} c_+|\Psi^E\rangle = e^{i\phi_E} c_-^\dagger v_+^\dagger|0\rangle \\ |\psi_-\rangle &= \tfrac{M_-|\Psi^E\rangle}{\sqrt{p(-)}} = c_-|\Psi^E\rangle = \tfrac{1}{\sqrt{2}}(v_+^\dagger v_-^\dagger|0\rangle + e^{i\phi_E} c_+^\dagger v_+^\dagger|0\rangle) \end{aligned} \tag{A.19}$$

$$\begin{aligned} \rho_{red} &= p(+)|\psi_+\rangle\langle\psi_+| + p(-)|\psi_-\rangle\langle\psi_-| \\ &= \tfrac{1}{3} c_-^\dagger v_+^\dagger|0\rangle\langle 0|v_+ c_- + \tfrac{1}{3}(v_+^\dagger v_-^\dagger + c_+^\dagger v_+^\dagger)|0\rangle\langle 0|(v_- v_+ + v_+ c_+) \end{aligned} \tag{A.20}$$

Now the entropy of entanglement for $|\Psi^E\rangle$ can be found.

$$S(\rho_{red}) = -\mathrm{Tr}(\rho_{red}\log_2\rho_{red}) = -\frac{2}{3}\log_2\frac{2}{3} - \frac{1}{3}\log_2\frac{1}{3} \approx .92 \tag{A.21}$$

This illustrates that measuring the spin of an electron in a dot that is in state $|\Psi^E\rangle$ results in a conditional state with an entropy of entanglement that is nonzero, but less than the maximal value of one.

A.6 Entropy of Entanglement of $|\Psi_{decay}\rangle$

The previous section calculated that the state $|\Psi^E\rangle$ was not maximally entangled. By contrast, the state $|\Psi_{decay}\rangle = (|x-\rangle|0\rangle_c + e^{i\phi_E}|x+\rangle|1\rangle_c)/\sqrt{2}$ left after the state $|\Psi^E\rangle$ decays is analogous to the EPR state and has a maximal entropy of 1, as calculated here. In the creation operator notation,

$$|\Psi_{decay}\rangle = \frac{1}{\sqrt{2}}(c_-^\dagger|0\rangle + e^{i\phi_E}c_+^\dagger a_k^\dagger|0\rangle). \tag{A.22}$$

Following the same procedure as in the previous two calculations,

$$M_\pm = c_\pm \tag{A.23}$$

$$p(+) = p(-) = \frac{1}{2} \tag{A.24}$$

$$|\psi_+\rangle = e^{i\phi_E}a_k^\dagger|0\rangle \quad |\psi_-\rangle = |0\rangle \tag{A.25}$$

$$\rho_{red} = \frac{1}{2}a_k^\dagger|0\rangle\langle 0|a_k + \frac{1}{2}|0\rangle\langle 0|, \tag{A.26}$$

and therefore

$$S(\rho_{red}) = -\frac{1}{2}\log_2\frac{1}{2} + -\frac{1}{2}\log_2\frac{1}{2} = 1 \tag{A.27}$$

proving that $|\Psi_{decay}\rangle$ is maximally entangled.

BIBLIOGRAPHY

BIBLIOGRAPHY

[1] B. Schumacher, M. Westmoreland, *Quantum Processes Systems, and Information*, Cambridge University Press, Cambridge, United Kingdom, first edition (2010).

[2] M. A. Nielsen, I. L. Chuang, *Quantum Computation and Quantum Information*, Cambridge University Press, Cambridge, United Kingdom, first edition (2000).

[3] J. C. Slater, "The Theory of Complex Spectra", *Phys. Rev.* **34**, 1293 (1929).

APPENDIX B

An interferometer for phase stability

In the experimental proposal from Chapter 4, it is essential that the delay between pulses 3 and 4 is stable to less than an optical cycle. Additionally,the proposal requires scanning the delay between the fourth and fifth pulse with a resolution small enough to observe oscillations at the optical frequency. These two requirements can be met by a beam path that contains two interferometers, as shown in Figure B.1. One pulse is split into pulses 3-5 for the full experiment. Changes in the path difference between the fourth and fifth pulses are passively detected by a photodetector monitoring interference fringes from a green HeNe. This path difference can be scanned during the measurement with the piezoelectric mirror A. The path difference between pulse 3 and pulses 4 and 5 is actively locked with a feedback circuit that controls piezoelectric mirror B and monitors the fringes of a red HeNe. A high pass filter prevents either HeNe beam from reaching the sample.

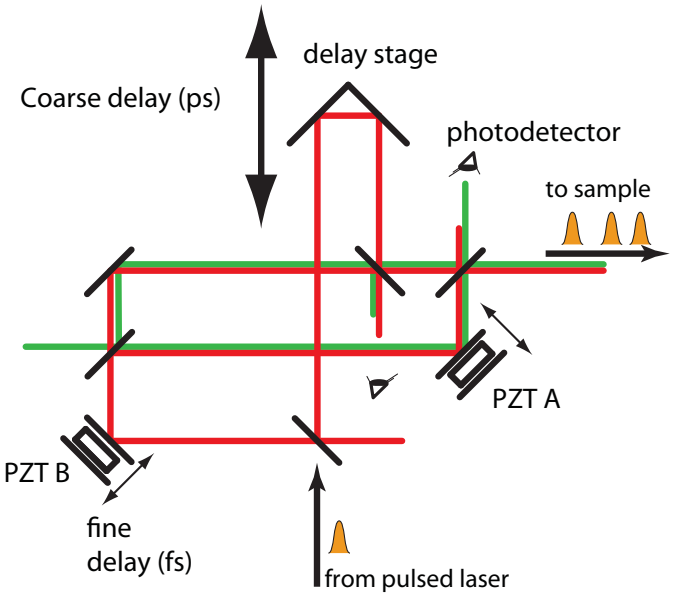

Figure B.1: A double interferometer designed by Leon Webster that splits one pulse into three pulses, for use as pulses 3-5 in the experiment proposed in Chapter 4.

APPENDIX C

Filtering pulses with a Fabry-Perot etalon

The signal to noise ratio could be improved when implementing the experiment proposed in Chapter 4 by spectrally filtering most of the power from the pulses with a Fabry-Perot etalon before the detector while passing the narrowband CW readout beam. An etalon mode can be angle tuned into resonance with the CW beam by maximizing the transmission of the CW beam through the etalon. I designed a custom Fabry Perot for this purpose, which was built by TecOptics. It was important that the etalon be narrow enough that a pulse traveling through the etalon will overlap in time with many reflected pulses such that they form frequency modes. This requires that the round trip time in the cavity must be much less than the pulsewidth [1]. The etalon is air spaced with the spacers made from Corning ULE, an extremely thermally stable material, so the etalon modes should not shift noticeably with normal daily ambient temperature changes. Piezoelectric tunable etalons are available, but require active electronic stabilization using strain gauges, so a fixed width etalon that can be angle tuned was simpler and more cost effective. The etalon can be angle tuned by more than its free spectral range, so it can be used at any wavelength from about 900 nm to 1μm, limited only by the bandwidth of the reflective coatings on the etalon.

The primary design criteria was to maximize $\frac{T_{CW}}{\sqrt{T_{pulse}}}$, where T_{CW} (T_{pulse}) is the fraction of CW (pulse) power transmitted by the etalon. T_{CW} was provided by the manufacturer. T_{pulse} was numerically estimated for a given pulse from this expression

for the transmitted electric field of the pulse:

$$E_{pulseout}(\omega) = E_{pulsein}(\omega) \sum_{m=1}^{M} R^{m-1}(1-R)e^{-\frac{2il\omega(m-1)}{c}}, \tag{C.1}$$

where R is the etalon's reflectivity and l its width [1]. This formula adds the transmitted fields produced by 1 through M reflections, where M is given by the pulsewidth divided by the single pass time across the etalon. The ratio of integrals

$$T_{pulse} = \frac{\int_{\omega_1}^{\omega_2} |E_{pulseout}(\omega)|^2 \, \mathrm{d}\omega}{\int_{\omega_1}^{\omega_2} |E_{pulsein}(\omega)|^2 \, \mathrm{d}\omega} \tag{C.2}$$

gives T_{pulse}.

The purchased etalon has a finesse of about 100 and is 42 μm in width for a free spectral range of 3500 GHz. Including the effects of angle tuning, it is estimated that $T_{CW} \approx .76$ and $T_{pulse} \approx .08$ for an improvement in signal to noise of 2.7, which is over a 7 times reduction in averaging time. There may be some degradation in the performance of the etalon due to distortion in the wavefront by the aluminum apertures on the sample, but the etalon should work well with the apertureless samples being used by some group members.

BIBLIOGRAPHY

BIBLIOGRAPHY

[1] A. Kastler, "Transmission of light pulse through a Fabry-Perot interferometer", *Nouvelle Revue d'Optique* **5**, 133 (1974).